Accepted for publication in the Astrophysical Journal

A Uniform Analysis of the Ly-α Forest at $z = 0 - 5$: V. The extragalactic ionizing background at low redshift

Jennifer Scott, Jill Bechtold, Miwa Morita

Steward Observatory, University of Arizona, Tucson, AZ 85721, USA
e-mail: [jscott,jbechtold,mmorita]@as.arizona.edu

Adam Dobrzycki

Harvard-Smithsonian Center for Astrophysics, 60 Garden Street, Cambridge, MA 02138, USA
e-mail: adobrzycki@cfa.harvard.edu

Varsha P. Kulkarni

University of South Carolina, Department of Physics and Astronomy, Columbia, SC 29208, USA
e-mail: varsha@mail.psc.sc.edu

ABSTRACT

In Paper III of our series "A Uniform Analysis of the Ly-α forest at $z = 0-5$", we presented a set of 270 quasar spectra from the archives of the Faint Object Spectrograph (FOS) on the Hubble Space Telescope (HST). A total of 151 of these spectra, yielding 906 lines, are suitable for using the proximity effect signature to measure $J(\nu_0)$, the mean intensity of the hydrogen-ionizing background radiation field, at low redshift. Using a maximum likelihood technique and the best estimates possible for each QSO's Lyman limit flux and systemic redshift, we find $J(\nu_0) = 7.6^{+9.4}_{-3.0} \times 10^{-23}$ ergs s^{-1} cm^{-2} Hz^{-1} sr^{-1} at $0.03 < z < 1.67$. This is in good agreement with the mean intensity expected from models of the background which incorporate only the known quasar population. When the sample is divided into two subsamples, consisting of lines with $z < 1$ and $z > 1$, the values of $J(\nu_0)$ found are $6.5^{+38.}_{-1.6} \times 10^{-23}$ ergs s^{-1} cm^{-2} Hz^{-1} sr^{-1}, and $1.0^{+3.8}_{-0.2} \times 10^{-22}$ ergs s^{-1} cm^{-2} Hz^{-1} sr^{-1}, respectively, indicating that the mean intensity of the background is evolving over the redshift range of this data set. Relaxing the assumption that the spectral shapes of the sample spectra and the background are identical, the best fit HI photoionization rates are found to be 6.7×10^{-13} s^{-1} for all redshifts, and 1.9×10^{-13} s^{-1} and 1.3×10^{-12} s^{-1} for $z < 1$ and $z > 1$, respectively. The inclusion of blazars, associated absorbers, or damped Ly-α absorbers, or the consideration of a Λ CDM cosmology rather than one in which $\Omega_\Lambda = 0$ has no significant effect on the results. The result obtained using radio loud objects is not significantly different from that found using radio quiet objects. Allowing for a variable equivalent width threshold gives a consistently larger value of $J(\nu_0)$ than the constant threshold treatment, though this is found to be sensitive to the inclusion of a small number of weak lines near the QSO emission redshifts. This work confirms that the evolution of the number density of Ly-α lines is driven by a decrease in the ionizing background from $z \sim 2$ to $z \sim 0$ as well as by the formation of structure in the intergalactic medium.

Subject headings: diffuse radiation— intergalactic medium—quasars: absorption lines

1. Introduction

The spectra of quasars show a “forest” of absorption lines blueward of the Ly-α emission line (Lynds 1971, Sargent et al. 1980, Weymann, Carswell, & Smith 1981). Observational and theoretical work in recent years has shown that most of this absorption can be attributed to neutral hydrogen in galaxies and large-scale structure along the line of sight (Cen et al. 1994, Lanzetta et al. 1995,1996, Zhang et al. 1995, Hernquist et al. 1996, Miralda-Escudé et al. 1996, Bi & Davidsen 1997, Chen et al. 1998, Theuns et al. 1998, Ortiz-Gil et al. 1999, Impey, Petry, & Flint 1999, Davé et al. 1999, Bryan et al. 1999). In aggregate, QSO spectra show an increasing line density with increasing redshift such that $dN/dz \propto (1. + z)^\gamma$ (Sargent et al. 1980, Weymann, Carswell, & Smith 1981, Young et al. 1982, Murdoch et al. 1986, Lu, Wolfe, & Turnshek, 1991, Bechtold 1994, Kim et al. 1997). But the line density within an individual quasar spectrum decreases with proximity to the Ly-α emission line (Weymann, Carswell, & Smith 1981, Murdoch et al. 1986). This is generally thought to be due to enhanced ionization of neutral hydrogen in the vicinity of the quasar due to ionizing photons from the quasar itself. This “proximity effect” can be used to measure the mean intensity of the UV background, denoted $J(\nu_0)$ (Carswell et al. 1987, Bajtlik, Duncan, & Ostriker 1988, hereafter BDO).

$J(\nu_0)$ has been measured at $z > 1.7$ by a variety of authors (BDO, Lu, Wolfe, & Turnshek 1991, Giallongo et al. 1993,1996, Bechtold 1994, Williger et al. 1994, Cristiani et al. 1995, Fernández-Soto et al. 1995, Lu et al. 1996, Savaglio et al. 1997, Cooke et al.

1997, Scott et al. 2000b). The results, summarized in Paper II of this series (Scott et al. 2000b), are in general agreement with the predictions of models of the UV background which integrate the contribution from known population of quasars and include reprocessing effects in an inhomogeneous intergalactic medium (Haardt & Madau 1996, hereafter HM96, Fardal et al. 1998). In Paper II, the mean intensity of the ionizing background was found to be $7.0^{+3.4}_{-4.4} \times 10^{-22}$ ergs s^{-1} cm^{-2} Hz^{-1} sr^{-1} at $z \sim 3$. The decline of the quasar space density from $z \sim 2$ to the present is expected to drive a corresponding decline in the intensity of the UV background. Kulkarni & Fall (1993, hereafter KF93) measured $J(\nu_0) \sim 6 \times 10^{-24}$ ergs s^{-1} cm^{-2} Hz^{-1} sr^{-1} at $z \sim 0.5$ from a subset of the now complete HST Quasar Absorption Line Key Project sample presented by Bahcall et al. (1993).

Much of this previous work has relied upon the technique for measuring $J(\nu_0)$ outlined by BDO. This technique requires the entire sample of absorption lines to be binned according to the ratio of the quasar flux at the physical position of the absorber to the background flux. This is done for several initial guesses of the background intensity; and the value that gives the lowest χ^2 between the binned data and the ionization model is chosen as the best fit $J(\nu_0)$. However, this is not the optimal technique to use at low redshift where absorption line densities are low. KF93 developed a maximum likelihood technique to address this issue and used it in their measurement of $J(\nu_0)$ at $z \sim 0.5$. However, their measurement was based upon a sample of only 13 QSOs and less than 100 lines, and has correspondingly large error bars. In addition, the value these authors find is lower than the predictions of the models of Haardt & Madau (1996), though consistent within the uncertainties, as shown in Figure 13 of Paper II and in Figure 11 of this paper. Given the importance of the value of the HI ionization rate to the hydrodynamical evolution of the low redshift universe, performing this measurement with a much larger line sample is worthwhile.

The low redshift hydrodynamic simulations of Theuns et al. (1998) and Davé et al. (1999) indicate that the evolution of the ionizing background is the primary driver behind the change of character of the Ly-α forest from high redshift to low redshift, specifically, the break in the number distribution of Ly-α lines at $z = 1.7$ (Morris et al. 1991, Bahcall et al. 1991, Weymann et al. 1998). The growth of structure pulling gas from low density regions into high density regions also contributes to this and other attributes of the evolution of the Ly-α forest.

Shull et al. (1999) estimate the local ionizing background including contributions to the background from starburst galaxies as well as Seyferts and QSOs. Their models include a treatment of the opacity of the low redshift Ly-α forest using information drawn from recent observational work (Weymann et al. 1998, Penton et al. 2000b). They find that starbursts and AGN could contribute approximately equally to the ionizing background at low redshift, each $\sim 1.0 \times 10^{-23}$ ergs s^{-1} cm^{-2} Hz^{-1} sr^{-1}.

The full HST/FOS archival data set is presented in Paper III and can also be found at

`http://lithops.as.arizona.edu/~jill/QuasarSpectra` or

`http://hea-www.harvard.edu/QEDT/QuasarSpectra`,

so we describe the data used in this paper only briefly in §2. In §3 and §4, we discuss our treatment of two parameters of each sample object which are integral to the proximity effect analysis, systemic redshifts and Lyman limit fluxes. We outline the proximity effect analysis in §5 and we present our results in §7. We discuss the recovery of $J(\nu_0)$ from simulated Ly-α forest spectra in §6.1. A comparison of the results from radio loud and radio quiet QSOs is given in §7.1. The maximum likelihood solutions for $J(\nu_0)$ found when allowing for an equivalent width threshold that varies across each sample spectrum are discussed in §6.3. Solutions for the HI ionization rate are given in §6.2. The effect of a non-zero Ω_Λ on our calculations is discussed in §7.2, and the effect of the ionizing background on the Ly-α forest line density is discussed in §7.3. We provide comparisons with previous observational work on the low redshift UV background in §7.4 and with models of this background in §7.5. A discussion of possible systematic effects on this analysis is given in §7.6. We conclude with a summary of the results in §8.

2. Data Sample

The reduction of the FOS data is described in Paper III. Table 1 lists the objects used in the proximity effect analysis along with the object's redshift and classification in the NASA Extragalactic Database.

For the reasons outlined in Scott et al. (2000b) we have removed from the full FOS sample of Paper III the spectra of quasars known to be lensed, as well as those that show damped Ly-α absorption, associated absorption, or broad intrinsic absorption. For our primary proximity effect sample, we also remove objects classified as blazars (BL Lacs and optically violent variables) on the grounds that their continua are highly variable. However, we also perform the proximity effect analysis with associated absorbers, damped Ly-α absorbers, and blazars included in order to determine if they affect the results obtained.

As discussed in Paper III, objects observed only in the period before the COSTAR upgrade to the HST optics and with the A-1 FOS aperture are particularly subject to irregular line spread functions. We have omitted those data from this analysis as well. The distributions in redshift of the QSOs and absorption lines used in this paper are shown in

Figure 1.

3. Systemic Redshifts

QSO redshifts based on the Ly-α emission line have been shown to be blueshifted from the systemic redshift based on narrow emission lines by up to $\sim$ 200 km s^{-1}. Generally, the forbidden OIII doublet at 4959, 5007 Å is taken to be the most reliable indicator of the QSO systemic redshift; though other lines such as Mg II $\lambda\lambda$2796,2803 and Balmer lines have been shown to trace the systemic redshift as well, with some spread. (Zheng & Sulentic 1990, Tytler & Fan 1992, Laor et al. 1994,1995, Corbin & Boroson 1996) However, the results of Nishihara et al. (1997), M^{c}Intosh et al. (1999), and Scott et al. (2000b) indicate that in fact Hβ may not reflect the systemic redshift of high redshift QSOs.

3.1. Observations

Spectra of the emission lines Hβ, [OIII]λ5007, or Mg II were obtained for several objects in our total proximity effect sample. The observations were carried out on the nights of 19 December 1995, 14 January 1996, 20 and 21 April 1996, 12 and 13 December 1996, and 2 February 1997. These observations are summarized in Table 2.

The 19 December 1995 and 13 December 1996 observations were made using the 1.5 meter Tillinghast telescope at the Fred Lawrence Whipple Observatory using the FAST spectrograph (Fabricant et al. 1998) and a thinned Loral 512x2688 CCD chip (gain = 1.06, read noise = 7.9 e^{-}) binned by a factor of 4 in the cross-dispersion direction. Observations were made using a 300 lines mm^{-1} grating blazed at 4750 Å and a 3$''$ slit. These spectra cover a wavelength range of 3660–7540 Å. This is listed as set-up (1) in Table 2.

The January, April, and December 10 and 12, 1996 observations were made using the Steward Observatory Bok 90 inch telescope using the Boller and Chivens Spectrograph with a 600 l mm^{-1} grating blazed at 6681 Å in the first order, a 1.5$''$ slit, and a 1200 x 800 CCD array with a gain of 2.2 e^{-} ADU^{-1} and a read noise of 7.7 e^{-}, binned 1x1. For the January 1996 observations, the data were obtained with one of two grating tilts, one resulting in wavelength coverages of 3600–5825 Å and 6870–9140 Å. For the April 1996 data, the wavelength ranges were 4140–6370 Å and 5280–7550 Å. Two grating tilts were also used for the December 1996 data, giving wavelength coverages of 4500–6700 Å and 5610–7860 Å.

The spectrum of one object, 0827+2421, was obtained on 15 February 1997 at the Multiple Mirror Telescope with the Blue Channel Spectrograph, a 2 $''$ slit, the 3K x 1K CCD array, and the 800 l mm^{-1} grating blazed at 4050 Å with spectral coverage of 4365–6665 Å.

The spectra are shown in Figure 2 and the lines used for redshift measurements are labeled.

3.2. Measurements

Taking a simple cursor measurement of each line centroid, we find a mean [OIII]-Balmer line Δv of -30 $\pm$ 1010 km s^{-1} for 31 objects and a mean [OIII]-Mg II Δv of 58 $\pm$ 576 km s^{-1} for 31 objects. The mean blueshift of the Ly-α emission line with respect to [OIII] is 289 $\pm$ 727 km s^{-1} based on 51 measurements. The redshifts measured for each object in our sample are shown in Table 1; and the results are shown in Figure 3. Gaussian fits to the lines give similar results.

We therefore treat both Balmer lines and Mg II in addition to [OIII] as good systemic redshift indicators for these low redshift objects. In the case of a QSO for which we have only a Ly-α emission line measurement of the redshift, we add 300 km s^{-1} to this value to estimate its systemic redshift.

4. Lyman Limit Fluxes

Our method for estimating Lyman limit fluxes for each QSO is the same as that described in Paper II. For objects with spectral coverage between the Ly-α and CIV emission lines, we extrapolate the flux from 1450 Å in the quasar's rest frame to 912 Å using $f_\nu \sim \nu^{-\alpha}$ and a spectral index α measured from the spectral region between the Ly-α and C IV emission lines. Figure 4 shows the FOS spectra for which these fits were made along with the power law fits themselves. In some cases, α is poorly constrained from these fits, especially if there was little spectral coverage redward of Ly-α emission in the data. If another measurement of the spectral index was available in the literature for these objects, we used it; otherwise, we used our measurement.

Table 3 lists the Lyman limit flux for each object in this proximity effect sample and either a) the flux at 1450 Å, or some other appropriate wavelength free of emission features, measured from the FOS data, or b) a directly measured Lyman limit flux and the reference. If available from the extracted archive data, red spectra and the fits to them are presented for objects which were observed only with pre-COSTAR FOS and A-1 aperture, though these data were not subsequently used for any Ly-α forest studies. See Table 4 of Paper III.

In Figure 5, we show QSO Lyman limit luminosities versus emission redshift for this HST/FOS sample combined with the high redshift objects presented in Papers I and II. Only at the lowest redshifts is there any trend of luminosity with redshift.

5. Analysis

The distribution of Ly-α lines in redshift and equivalent width is given by:

$$\frac{\partial^2 \mathcal{N}}{\partial z \partial W} = \frac{A_0}{W^*}(1+z)^{\gamma} \exp\left(-\frac{W}{W_*}\right). \tag{1}$$

The distribution in redshift and HI column density, N, is:

$$\frac{\partial^2 \mathcal{N}}{\partial z \partial N} = A N^{-\beta}(1+z)^{\gamma}. \tag{2}$$

The parameter γ is the redshift distribution parameter. The quantities W^* in Equ. 1 and β in Equ. 2 are the line rest equivalenth width and column density distribution parameters, respectively. The quantities A_0 and A are normalizations.

The BDO method for measuring $J(\nu_0)$ consists of binning all lines in the sample in the parameter $\omega(z)$, the ratio of QSO to background Lyman limit flux density at the physical location of the absorber: $F^Q(\nu_0)/(4\pi J(\nu_0))$ for various values of $J(\nu_0)$. The value of $J(\nu_0)$ that results in the lowest χ^2 between the binned data and the ionization model,

$$\frac{d\mathcal{N}}{dz} = \mathcal{A}_0(1+z)^{\gamma}[1+\omega(z)]^{-(\beta-1)}, \tag{3}$$

is considered to be the optimal value. This ionization model follows from the assumption that the column densities of lines are modified by the presence of the QSO according to

$$N \propto N_0(1+\omega(z))^{-1}, \tag{4}$$

where N_0 is the column density a given line would have in the absence of the QSO. The 1σ errors are found from $\Delta\chi^2 = 8.18$ for 7 degrees of freedom (Press et al. 1992).

The value of $\omega(z)$ for each line in a given sample depends not only upon the value of $J(\nu_0)$ assumed, but also on the cosmological model, as

$$F^Q(\nu_0) = \frac{L(\nu_0)}{4\pi r_L^2(z)} \tag{5}$$

and

$$L(\nu_0) = 4\pi d_L^2(z)\frac{f(\nu_0)}{(1+z_{em})}, \tag{6}$$

where $r_L(z)$ is the luminosity distance of an individual absorber from the QSO and $d_L(z)$ luminosity distance to the QSO from the observer. The luminosity distance between two objects at different redshifts can be calculated analytically for cosmological models in which $\Omega_\Lambda = 0$. We return to this point in Section 7.2 below.

If the proximity effect is indeed caused by enhanced ionization of the IGM in the vicinity of QSOs, one may expect to observe a larger deficit of lines relative to the Ly-α forest near high luminosity QSOs than near low luminosity QSOs. In Figure 6(a), we plot the fractional deficit of lines with respect to the number predicted by Equ. 1 versus distance from the QSO for this HST/FOS sample combined with the high redshift objects observed with the Multiple Mirror Telescope (MMT) presented in Papers I and II. We divide our QSO sample into high and low luminosity objects at the median Lyman limit luminosity of the combined MMT and HST/FOS sample, $\log(L_{912\,\text{Å}}) \sim 31$. High luminosity objects show a marginally more pronounced proximity effect than low luminosity objects: 4.9σ for QSOs with $\log(L_{912\,\text{Å}}) > 31$ versus 3.2σ for QSOs with $\log(L_{912\,\text{Å}}) < 31$. In panel (b), we plot the line deficit within 2 h_{75}^{-1} Mpc as a function of $\log(L_{912\,\text{Å}})$. The lack of a significant difference in the line deficit between high and low luminosity QSOs may indicate the presence of clustering, if absorption features cluster more strongly around more luminous QSOs with deeper potential wells. We will address the issue of clustering further below.

The BDO method of measuring the background can result in poor statistics at low redshift due to the low line density in the low redshift Ly-α forest. We will quote results from this method, but we will generally the maximum likelihood method for measuring $J(\nu_0)$ as presented by KF93, which consists of constructing a likelihood function of the form

$$L = \prod_a f(N_a, z_a) \prod_q \exp[-\int_{z^q_{\rm min}}^{z^q_{\rm max}} dz \int_{N^q_{\rm min}}^{\infty} f(N,z)dN], \tag{7}$$

where

$$f(N,z) = AN^{-\beta}(1+z)^{\gamma}[1+\omega(z)]^{-(\beta-1)}, \tag{8}$$

and the indicies a and q denote sample absorption lines and quasars, respectively. Using the values of γ and A_0 from a separate maximum likelihood analysis on the Ly-α forest excluding regions of the spectra affected by the proximity effect (Dobrzycki et al. 2001, Paper IV), and a value of β from studies with high resolution data, eg. $\beta = 1.46$ from Hu et al. (1995), the search for the best-fit value of $J(\nu_0)$ consists of finding the value that maximizes this function, fixing the other parameters.

If the line density is low throughout a single Ly-α forest spectrum, it becomes difficult to distinguish any proximity effect, even in a large sample of spectra. The absence of a proximity effect in this model formally translates into the limit $J(\nu_0) \to \infty$ because in this scenario, the QSO has no additional effect on its surroundings and therefore generates no relative line underdensity. The errors quoted in the values of $\log[J(\nu_0)]$ are found from the fact that in solving for $\log[J(\nu_0)]$ alone, the logarithm of the likelihood function, $-2\ln(L/L_{\max})$, is distributed as χ^2 with one degree of freedom. In the case of an ill-defined solution, the likelihood function is very broad and the formal error approaches infinity. If a proximity effect is weak but not absent in the data, a maximum likelihood solution is sometimes possible, but with no well-defined 1σ upper limit on $\log[J(\nu_0)]$. In other words, if an upper limit of infinity is quoted, the data cannot rule out the nonexistence of a proximity effect to within 1σ confidence.

Using a constant equivalent width threshold results in the loss of a large amount of spectral information. In the case of a large equivalent width threshold, of course, many weak lines are discarded; and in the case of a small threshold, regions of spectra where the signal-to-noise ratio (S/N) does not permit the detection of lines all the way down to the specified threshold are lost and only the highest S/N spectral regions are used. The technique of measuring the statistics γ and W^* has been expanded to allow for a threshold that varies with S/N across each QSO spectrum (Bahcall et al. 1993,1996, Weymann et al. 1998, Scott et al. 2000a). We will use this variable threshold information to measure $J(\nu_0)$ as well.

6. Results

The results of this analysis are given in Table 4.

Before we begin the discussion of the results, some words about the normalization values listed in Table 4 are in order. In the BDO method for measuring $J(\nu_0)$, lines are binned in $\omega(z)$ and compared to the ionization model given by Equ. 3, for an assumed value of β. In this case, the normalization listed in Table 4 is the parameter in Equ. 1, found from the number of lines in the sample and the maximum likelihood value of γ:

$$\mathcal{A}_0 = A_0 \exp\left(-\frac{W_{\rm lim}}{W_*}\right) = \mathcal{N}\left(\sum_q \int_{z^q_{\rm min}}^{z^q_{\rm max}} dz\,(1+z)^\gamma\right)^{-1}, \qquad (9)$$

where $\mathcal{N}$ is the total number of lines observed with rest equivalent width greater than $W_{\rm lim}$, the limiting equivalent width of the line sample. For the maximum likelihood solutions for $J(\nu_0)$, we convert line equivalent widths to column densities using the Ly-α curve of growth and an assumed value of b, the characteristic Doppler parameter of the lines. As we will demonstrate, different values of β and b have only a small effect on the value of $J(\nu_0)$ found.

The normalization is given by

$$A = \mathcal{N} \left(\sum_q \int_{z^q_{\rm min}}^{z^q_{\rm max}} dz \int_{N^q_{\rm min}(z)}^{\infty} dN \, N^{-\beta} (1+z)^{\gamma} \right)^{-1} , \tag{10}$$

where $N^q_{\rm min}(z)$ is the limiting column density across each QSO spectrum corresponding to a limiting equivalent width. This quantity can be held constant, as in the BDO method, or it can be allowed to vary across each QSO spectrum. In both of these formulations for the normalization, a proximity region around the QSO is neglected and that proximity region is either defined by a velocity cut, eg. $z_{\rm em}$ - 3000 km s^{-1}, or by a cut in $\omega(z)$, eg. $\omega(z) = 0.2$.

We also use the standard BDO method to find $\log[J(\nu_0)] = -22.04^{+0.43}_{-1.11}$ and $-22.06^{+0.05}_{-0.62}$ for equivalent width thresholds of 0.32 and 0.24 Å respectively. Figures 7(a) and (d) illustrate the χ^2 of the binned data compared to the BDO ionization model as a function of assumed $J(\nu_0)$ for these two thresholds. The BDO ionization model is expressed in terms of the number of lines per coevolving coordinate:

$$\frac{dN}{dX_\gamma} = \mathcal{A}_0 (1+\omega)^{-(\beta-1)}, \tag{11}$$

where $X_\gamma = \int (1+z)^\gamma dz$. This χ^2 curve is very broad, which is reflected in the large error bars and indicates the difficulty in isolating the optimal mean intensity of a weak background using this technique. Figures 8(a) and (d) show the binned data and the ionization model for the values of $J(\nu_0)$ listed above, those that give the lowest χ^2 between the binned data and the model, ie. the minima of the curves in Figures 7(a) and (d).

We executed the maximum likelihood search for $J(\nu_0)$, using two different fixed equivalent width thresholds, 0.24 Å and 0.32 Å as well as for the case of a variable threshold across all the spectra. The uncertainty in γ does not translate directly into a large uncertainty in $J(\nu_0)$. Changing the value of γ alters the maximum likelihood normalization, A, according to Equ. 10. From the sample of lines with rest equivalent widths greater than 0.32 Å we find $\log[J(\nu_0)] = -22.11^{+0.51}_{-0.40}$ for $\gamma = 0.82 \pm 0.29$. Varying γ by $\pm 1\sigma$ gives $\log[J(\nu_0)] = -22.21$ and -22.00 with similar uncertainties.

The data used here are not of sufficient resolution to fit Voigt profiles to the absorption features and derive HI column densities and Dopper parameters. We therefore choose to fix the values of β and b to those found from work on high resolution data, rather than allow them to freely vary in our analysis. For the 0.32 Å fixed equivalent width threshold, we tested several pairs of values of (β, b) where b is in km s^{-1}: (1.46,35) and (1.46,25) where the value of β is taken from Hu et al. (1995); as well as (1.45,25) and (1.70,30) found from low redshift Ly-α forest spectra taken with the Goddard High Resolution Spectrograph (GHRS) on HST by Penton et al. (2000a,b). In addition, Davé & Tripp (2001) have found some evidence for β increasing to 2.04 at $z < 0.3$ from high resolution echelle data from the Space Telescope Imaging Spectrograph aboard the HST. We test this value as well. The likelihood functions for the maximum likelihood solutions listed in rows 2-6, 8-12, 14, and 18 of Table 4 are shown in Figure 9. The binned data and ionization models are plotted in Figure 10. The values of $J(\nu_0)$ derived for these various pairs of values of β and b are not significantly different from one another, though the results in Table 4 indicate that varying β has a larger impact on the inferred $J(\nu_0)$ than does varying b. The solution for $\beta = 2.04$ differs from the $\beta = 1.46$ solution by $\sim 1\sigma$. In the analysis that follows, we adopt the values 1.46 and 35 km s^{-1}.

The models of Haardt & Madau (1996) predict that the UV background arising from QSOs drops by over an order of magnitude from $z = 2.5$ to $z = 0$. We therefore divide the sample into low and high redshift subsamples at $z = 1$ and use both the BDO method and the maximum likelihood method for finding $J(\nu_0)$. These results, also listed in Table 4, confirm some evolution in $J(\nu_0)$, though not at a high level of significance. For the BDO solutions, we find $\log[J(\nu_0)]$ at $z < 1$ is equal to $-22.87^{+1.19}_{-0.82}$ and $\log[J(\nu_0)]$ at $z > 1$ is equal to $-22.02^{+0.005}_{-1.33}$. The restrictive 1σ upper limit for $\log[J(\nu_0)]$ at $z > 1$ arises from the steeply rising χ^2 as a function of $\log[J(\nu_0)]$ shown in Figure 7. This, in turn arises from the single line in the highest $\log(\omega)$ bin moving to the next bin for larger values of $J(\nu_0)$, resulting in a drastic change in the χ^2 with respect to the photoionization model. We do not consider this to be a reliable indicator of the uncertainty in $J(\nu_0)$ at $z > 1$. The maximum likelihood technique gives more robust estimates of the uncertainties. From this analysis, we find $\log[J(\nu_0)]$ at $z < 1$ is found to be $-22.18^{+0.90}_{-0.61}$, while at $z > 1$ it is $-21.98^{+0.76}_{-0.54}$. These results are shown in Figures 11(a) and 16.

Including associated absorbers, damped Ly-α absorbers, or blazars in the proximity effect analysis appears to have little effect on the results. One might expect associated absorbers to reduce the magnitude of the observed proximity effect and hence cause $J(\nu_0)$ to be overestimated. The value found including the 45 associated absorbers in our sample is indeed larger, $\log[J(\nu_0)] = -21.74^{+0.55}_{-0.39}$, versus $\log[J(\nu_0)] = -22.11^{+0.51}_{-0.40}$, but not significantly so. Likewise, if the intervening dust extinction in damped Ly-α absorbers is significant, including these objects in our analysis could cause us to overestimate the magnitude of the proximity effect and hence underestimate $J(\nu_0)$. However, the inclusion of these 7 objects only negligibly reduces the value of $J(\nu_0)$ derived. QSO variability on timescales less than $\sim 10^5$ years would be expected to smooth out the proximity effect distribution (BDO). However, the inclusion of 6 blazars in the sample, all at $z < 1$, resulted in no discernible change in $J(\nu_0)$. The sample used in the analysis of HI ionization rates discussed below includes all of these objects.

For each solution, we calculate the χ^2 with respect to the ionization model expressed by Equ. 3, and the probability that the observed χ^2 will exceed the value listed by chance for a correct model, Q_{χ^2} (Press et al. 1992). We also execute a Kolmogorov-Smirnov (KS) test for each solution. The KS test provides a measure of how well the assumed parent distribution of lines with respect to redshift, given by Equ. 8, reflects the true redshift distribution of lines (cf. Murdoch et al. 1986, Press et al. 1992). The KS probability, $Q_{\rm KS}$, indicates the probability that a value of the KS statistic larger than the one calculated could have occurred by chance if the assumed parent is correct. The KS probability associated with each solution for $J(\nu_0)$ is listed in column 10 of Table 4.

6.1. Simulations

We tested our maximum likelihood methods, including our treatment of the variable equivalent width thresholds by running our analysis on a simulated data set. Each of the 151 spectra in this simulated data set had a redshift equal to that of an object in our data set. All objects including those showing associated absorption, damped Ly-α absorption, or blazar activity are included in this simulated set. Each spectrum is created using a Monte Carlo technique by which lines are placed in redshift and column density space according to Equ. 2. A background of known mean intensity modifies the column densities of the lines according to the BDO formulation given by Equ. 4. The same analysis done on the data, consisting of the line-finding algorithm and the maximum likelihood searches for γ and $J(\nu_0)$, is then used on the simulated spectra in order to recover the input $J(\nu_0)$. Three different values of $\log[J(\nu_0)]$ are input, -21, -22, and -23, and the results are listed in Table 5. In order to understand the possible range of recovered $\log[J(\nu_0)]$, we repeated the input $\log[J(\nu_0)] = -22$ simulation in the constant threshold case nine additional times, resulting in $\overline{J(\nu_0)} = 2.91 \pm 1.67 \times 10^{-22}$ ergs s^{-1} cm^{-2} Hz^{-1} sr^{-1}. In addition, since we observe the background to evolve with redshift from $z = 1$ to $z = 0$, we implement a model in which $J(\nu_0)$ varies as a power law in $(1 + z)$ over the redshift range of the data. This relationship is defined by the best fit to a power law variation of $J(\nu_0)$ with redshift: $\log[J(\nu_0)] = 0.017 \log(1 + z) - 21.87$. We recover this using both the constant threshold and the variable threshold analyses, at all redshifts and at $z < 1$ and $z > 1$ separately. The results of this exercise are shown in Table 5 and in Figure 12.

These simulation results indicate that both the constant and variable threshold analyses can overestimate the background by up to a factor of 3-5, though the uncertainties for the variable threshold solutions are consistently lower, as a factor of ~ 2 more lines are used in these solutions. We separated the first of the input $\log[J(\nu_0)] = -22$ simulated data samples into high and low redshift subsamples at $z = 1$, in order to determine if the change in $J(\nu_0)$ as a function of redshift could be falsely introduced in a case there the input background is constant with redshift. For both the constant and variable threshold treatments, this is not the case. The value found for the low redshift subsample is actually larger than the value found for the high redshift subsample in both treatments.

In the case of the varying input $\log[J(\nu_0)]$, the values recovered for the high redshift subsample and for the entire redshift range of the data are overestimates. The slope of the linear relationship between $\log[J(\nu_0)]$ and $\log(1 + z)$ is quite small, 0.017, resulting in a variable input $\log[J(\nu_0)]$ that is actually nearly constant with redshift. The solution for $z < 1$ matches the input well for both the constant and variable threshold cases. At $z > 1$, the variable threshold solution overestimates the input by a larger factor, $\sim$3, or 1.6σ, than does the constant threshold solution, $\sim$2, or less than 1σ.

In Paper II, we argued that curve-of-growth effects are likely to come into play in the proximity effect analysis and to play a larger role for cases in which $J(\nu_0)$ is large and the proximity effect signature is small. Here we find that the input $J(\nu_0)$ is recovered most effectively by the constant and variable threshold cases for the largest input value of $\log[J(\nu_0)]$, -21. However, nearly every case tested with these simulations results in a value of $J(\nu_0)$ larger than the input value, especially when a variable equivalent width threshold is used. The only case where the difference is significant is the input $\log[J(\nu_0)] = -23$, variable threshold case. The recovered $\log[J(\nu_0)]$, -22.47, is 4σ larger than the input. We will return to the discussion of the variable threshold in Section 6.3 below.

6.2. HI Ionization Rate

As described in Paper II, solving for the HI ionization rate,

$$\Gamma = \int_{\nu_0}^{\infty} \frac{4\pi J(\nu)\sigma_{HI}(\nu)}{h\nu} d\nu \ \ \mathrm{s}^{-1}, \tag{12}$$

instead of $J(\nu_0)$ avoids the assumption that the spectral indicies of the QSOs and the background are identical. We modified our maximum likelihood code to use the values of α for each QSO listed in Table 3 to measure this quantity and the results are listed in Table 6. For objects with no available measured value of α, we use $\alpha = 2.02$, the extreme ultraviolet spectral index measured from a composite spectrum of 101 HST/FOS QSO spectra by Zheng et al. (1997). The result for lines above a constant 0.32 Å rest equivalent width threshold is $\log(\Gamma) = -12.17^{+0.50}_{-0.40}$. This result is not substantially changed if we instead use $\alpha = 1.76$, the value found from a composite of 184 QSO spectra from HST/FOS, GHRS, and STIS by Telfer et al. (2001), giving $\log(\Gamma) = -12.25^{+0.47}_{-0.35}$. We also find little change in the result if we assume $\alpha = 2.02$ or $\alpha = 1.76$ for all QSOs. The variable threshold data result in a high HI ionization rate, and this is discussed further in the following section. The constant threshold result is plotted in Figure 13. Evolution in the UV background is more apparent in the HI ionization rate than in the solutions for $J(\nu_0)$. The result at $z > 1$ is 6.5 times larger than that at $z < 1$. The values of $J(\nu_0)$ implied by these solutions for Γ and a global source spectral index $\alpha_s = 1.8$ are also listed in Table 6.

We also parametrize the evolution of the HI ionization rate as a power law:

$$\Gamma(z) = A_{\rm pl}(1+z)^{B_{\rm pl}} \tag{13}$$

and solve for the parameters $A_{\rm pl}$ and $B_{\rm pl}$ in both the constant and variable threshold cases. The values we find are shown as the dashed line in Figure 13 also listed in Table 6.

HM96 parametrize their models of the HI ionization rate with the function:

$$\Gamma(z) = A_{\rm HM}(1+z)^{B_{\rm HM}} \exp\left(\frac{-(z-z_c)^2}{S}\right) \tag{14}$$

We combine our data set with that of Scott et al. 2000b to solve for the parameters $A_{\rm HM}$, $B_{\rm HM}$, z_c, and S. We find $(A_{\rm HM}, B_{\rm HM}, z_c, S)$= ($7.6 \times 10^{-13}$, 0.35, 2.07, 1.77) for β=1.46 and $(A_{\rm HM}, B_{\rm HM}, z_c, S)$ = (3.2×10^{-13}, 1.45, 2.13, 1.42) for β=1.7, while the parameters found by HM96 for $q_0 = 0.5$ are (6.7×10^{-13}, 0.43, 2.30, 1.95). These results are also represented by the solid curves in Figure 13, while the HM96 parametrization is shown by the dotted line for comparison.

6.3. Variable Equivalent Width Threshold

The variable threshold analysis yielded some unexpected results. As seen in the majority of the simulations, the values of $J(\nu_0)$ found were consistently larger than the values found using a constant equivalent width threshold, indicating that the inclusion of weaker lines suppresses the proximity effect. This is to be expected if clustering is occurring (Loeb & Eisenstein 1995), which in itself is to be expected to be more prominent at low redshift than at high redshift. However, the suppression of the proximity effect by the inclusion of weak lines is somewhat counterintuitive from the perspective of the curve of growth. Most of the lines included in a constant threshold solution are on the flat part of the curve of growth. Therefore, though the ionizing influence of the quasar may be translated directly into a change in the HI column density, as predicted by the BDO photoionization model, this will not necessarily result in a corresponding change in the line equivalent width. The solution for $z < 1$ is nearly a factor of 3 larger than the the solution found in the case of a constant, 0.32 Å equivalent width threshold. The solution for $z > 1$ is a factor of ~ 6 larger than the constant threshold solution, with no well-defined 1σ upper limit due to the flattening of the likelihood function towards high $J(\nu_0)$ This likelihood function for the total sample shows two peaks, the most prominent at $\log[J(\nu_0)] = -20.82$, the solution listed in Table 4, and a secondary peak at $\log[J(\nu_0)] \sim -18.4$.

This behavior is also exhibited, even more dramatically, in the solutions for the HI ionization rate, as discussed above. We conducted a jackknife resampling experiment (Babu & Feigelson 1996, Efron 1982) to determine the source of these likelihood function peaks at large $\log(\Gamma)$, or $\log[J(\nu_0)]$.

Two objects, 0743-6719 ($z_{\rm em} = 1.508$) and 0302-2223 ($z_{\rm em} = 1.402$), are found from jackknife experiments to produce all of this effect. In the jackknife experiment, we perform the maximum likelihood calculation of $J(\nu_0)$ N times, where N is the number of objects in the high redshift subsample. In each calculation, one object from the total sample is removed. The results of this experiment are shown in the histogram in Figure 14. The removal of 0743-6719 or 0302-2223 results in the two values of Γ that are well-defined and that are in reasonable agreement with the value calculated at high redshift in the constant threshold case. Removing only the one line from 0743-6719 nearest the Ly-α emission line with $z_{\rm abs} = 1.5058$ and observed equivalent width equal to 0.23 Å results in $\Gamma = 6.23 \times 10^{-12}$ s^{-1}. This object was part of the HST Key Project sample (Jannuzi et al. 1998) and they cite no evidence of associated aborption in its spectrum. Removing only the one line from 0302-2223 nearest the Ly-α emission line with $z_{\rm abs} = 1.3886$ and observed equivalent width equal to 0.27 Å results in $\Gamma = 8.14 \times 10^{-12}$ s^{-1}. This object shows an absorption system at $z_{\rm abs} = 1.406$ and is classified as an associated absorber. No metal absorption is seen at $z_{\rm abs} = 1.3886$, though this absorber is within 5000 km s^{-1} of the QSO, the canonical associated absorber region. Removing both of these lines gives $\Gamma = 3.88 \times 10^{-12}$ s^{-1}. Due to the small equivalent widths of both of these lines they are not included in the constant threshold analysis, and the solutions for $J(\nu_0)$ and Γ for $z > 1$ are well-defined.

It appears that this method has some trouble reliably recovering the background from a sample of absorption lines above an equivalent width threshold allowed to vary with S/N. As the method works well for the constant threshold case, we contend that the photoionization model, expressed in Equ. 3, used to create the likelihood function must not be an adequate model for the proximity effect when weak lines are included in the analysis. Liske & Williger (2001) introduce a method for extracting $J(\nu_0)$ from QSO spectra based on flux statistics. We shall return to this topic in future work.

7. Discussion

7.1. Radio Loudness

As the results listed in Table 4 indicate, the inclusion of the four blazars and one BL Lac object, all at $z < 1$, in our sample does not change the result significantly. However, there is much observational evidence that radio loud and radio quiet quasars inhabit different environments, namely that radio loud quasars reside in rich clusters while radio quiet quasars exist in galaxy environments consistent with the field (Stockton 1982, Yee & Green 1984, 1987, Yee 1987, Yates, Miller, & Peacock 1989, Ellingson, Yee, & Green 1991, Yee & Ellingson 1993, Wold et al. 2000, Smith, Boyle, & Maddox 2000). If there is a corresponding increase in the number of Ly-α absorption lines in the spectra of radio loud objects, this could cause the proximity effect to be suppressed, and the measured $\log[J(\nu_0)]$ to be artificially large. We have therefore divided our sample into radio loud and radio quiet subsamples using the ratio of radio to UV flux to characterize the radio loudness,

$$\mathrm{RL} = \log[\mathrm{S}(5\ \mathrm{GHz})]/\log[\mathrm{S}(1450\ \text{Å})]. \tag{15}$$

The value of RL for each object in our sample is listed in Table 3. A histogram of these values and the distribution of RL with z for the sample objects are shown in Figure 15. The division between radio loud and radio quiet was chosen to be RL=1.0. The resulting values of $\log[J(\nu_0)]$ for these subsamples are listed in Table 4. There is no significant trend for $\log[J(\nu_0)]$ to appear larger for radio loud objects than for radio quiet objects.

7.2. Non-Zero Ω_Λ

We performed the maximum likelihood calculation for the case of a non-zero cosmological constant. This means that the observer-QSO and absorber-QSO luminosity distances that appear in the relationship between ω and z (BDO) must be calculated numerically from the expression:

$$d_L = (1+z)\frac{c}{H_0}\int_0^z \frac{dz'}{E(z')}, \tag{16}$$

where

$$E(z) \equiv \sqrt{\Omega_{\mathrm{M}}(1+z)^3 + \Omega_{\mathrm{k}}(1+z)^2 + \Omega_\Lambda}, \tag{17}$$

(Peebles, 1993) as this integral cannot be reduced to an analytical form for $\Omega_\Lambda \neq 0$.

The calculations in the sections above assume $(\Omega_{\mathrm{M}},\Omega_\Lambda) = (1.0,0.0)$. Here, we perform the maximum likelihood search for $J(\nu_0)$ using $(\Omega_{\mathrm{M}},\Omega_\Lambda) = (0.3,0.7)$. For a QSO at $z = 0.5$

with a Lyman limit flux density of 0.1 μJy, an absorber at z = 0.48, and an assumed background of log[$J(\nu_0)$]= $-22.$, this ($\Omega_{\rm M}$,Ω_Λ) results in a value of ω that is $\sim$ 25% smaller than that inferred in the $\Omega_\Lambda = 0$ case. Unlike all the other solutions performed, we ignore redshift path associated with metal lines and use all redshifts between $z^q_{\rm min}$ and $z^q_{\rm max}$. This does not change the results significantly, but cuts down the computation time substantially. The results are listed in Table 4 and are plotted in Figure 11. For comparison, we also give the solutions for $J(\nu_0)$ found using the standard parameters, ($\Omega_{\rm M}$,Ω_Λ) = (1.0,0.0), with this redshift path neglected. We find that ($\Omega_{\rm M}$,Ω_Λ) = (0.3,0.7), does not change the value of $J(\nu_0)$ derived significantly from the value found using ($\Omega_{\rm M}$,Ω_Λ) = (1.0,0.0).

We performed a slightly modified re-analysis of the Scott et al. (2000b) sample of objects at $z \sim 2$ and found little effect at high redshift as well. The solution found for ($\Omega_{\rm M}$,Ω_Λ) = (1.0,0.0) was log[$J(\nu_0)$]= $-21.09^{+0.20}_{-0.17}$, while for ($\Omega_{\rm M}$,Ω_Λ) = (0.3,0.7), we find log[$J(\nu_0)$]= $-21.25^{+0.20}_{-0.17}$ for these data.

7.3. $d\mathcal{N}/dz$

In the case of a size distribution of Ly-α absorbers that is constant in redshift, the evolution of the number of Ly-α absorption lines per unit redshift is given by:

$$d\mathcal{N}/dz = \mathcal{N}_0(1+z)^2[\Omega_M(1+z)^3 + (1-\Omega_M-\Omega_\Lambda)(1+z)^2 + \Omega_\Lambda]^{-0.5}, \tag{18}$$

(Sargent et al. 1980) where $\mathcal{N}_0$ equals the absorber cross section times the absorber comoving number density times the Hubble distance, $\pi r_0^2 \phi_0 c H_0^{-1}$. A plot of $d\mathcal{N}/dz$ versus z for non-evolving Ly-α absorbers in (Ω_M,Ω_Λ) = (1.0,0.0) and (0.3,0.7) cosmologies is shown in Figure 17. It is clear that non-evolving models are too shallow to fit points at $z > 1.7$, so the normalization is found from a fit to the FOS data. The FOS data at $z < 1.7$ are consistent with a non-evolving population for $(\Omega_M, \Omega_\Lambda) = (1.0, 0.0)$. The data are less consistent with a non-evolving concordance model in which $(\Omega_M, \Omega_\Lambda) = (0.3, 0.7)$, though not significantly so.

The number density evolution of Ly-α absorbers over the redshift range $z = 0-5$ cannot be approximated with a single power law. There is a significant break in the slope of the line number density with respect to redshift, near z = 1.7 (Weymann et al. 1998, Paper IV) though Kim, Cristiani, & D'Odorico (2001) argue that the break occurs at z = 1.2. Davé et al. (1999) show from hydrodynamical simulations of the low redshift Ly-α forest, that the evolution of the line density is sensitive mainly to the HI photoionization rate, but also to the evolution of structure (cf. their Figure 7). The flattening of $d\mathcal{N}/dz$ observed by Weymann et al. (1998) is mostly attributed to a dramatic decline in $\Gamma(z)$ with decreasing z.

Davé et al. (1999) derive an expression for the density of Ly-α forest lines per unit redshift as a function of the HI photoionization rate:

$$\frac{d\mathcal{N}}{dz} = C[(1+z)^5\Gamma^{-1}(z)]^{\beta-1}H^{-1}(z), \tag{19}$$

where C is the normalization at some fiducial redshift which we choose to be $z = 0$ and $\Gamma(z)$ can be expressed by Equ. 14.

We fit the FOS and MMT absorption line data, binned in $d\mathcal{N}/dz$ as presented in Paper IV and Scott et al. (2000a, Paper I), to this function in order to derive the parameters describing $\Gamma(z)$ implied by the evolution in Ly-α forest line density. We observe flattening of $d\mathcal{N}/dz$ at $z < 1.7$, but not to the degree seen by Weymann et al. (1998) in the Key Project data. As described in Paper IV, we find $\gamma = 0.54 \pm 0.21$, for lines above a 0.24 Å threshold, while Weymann et al. (1998) measure $\gamma = 0.15 \pm 0.23$. See Paper IV for more discussion of the significance and underlying causes of this difference. We find $(A_{\rm HM}, B_{\rm HM}, z_c, S) = (3.0\times10^{-12}, 0.61, 5.5\times10^{-7}, 7.07)$ and $(1.9\times10^{-11}, 0.38, 3.4\times10^{-7}, 6.21)$ for $(\Omega_{\rm M}, \Omega_\Lambda) = (1., 0.)$ and lines with rest equivalent widths above 0.24 and 0.32 Å respectively. These fits to Equ. 19 are shown in Figure 18(a). In panel (b), we plot $\Gamma(z)$, as expressed in Equ. 14, evaluated using the parameters found from the fit to Equ. 19 above. The HM96 solution and the solution derived from the full FOS and MMT data sets are represented by the thick and thin solid lines respectively. The small values of z_c derived from $d\mathcal{N}/dz$ above translate into ionization rates that do not decrease dramatically with decreasing redshift and result from the less pronounced flattening of $d\mathcal{N}/dz$ relative to the Key Project. These fits are particularly insensitive to the normalization, $A_{\rm HM}$, so the errors on this parameter are large. These fits should therefore not be interpreted as measurements of $\Gamma(z)$ as reliable as those found directly from the absorption line data. But we find them instructive nonetheless. The observed $\Gamma(z)$ falls short of the ionization rate needed to fully account for the change in the Ly-α line density with redshift, indicating that if the value of γ at low redshift is indeed slightly larger than that found by the Key Project, $d\mathcal{N}/dz$ may still be consistent with a non-evolving population of Ly-α absorbers in the sense noted above, but the formation of structure in the low redshift universe must play a significant role in determining the character of the Ly-α forest line density.

7.4. Comparison with Previous Results

7.4.1. Proximity Effect

KF93 performed a similar measurement with a small subsample of this total sample- the HST Quasar Absorption Line Key Project data of Bahcall et al. (1993). We compare our result to that from Sample 2 of KF93, which was constructed from the Bahcall et al. (1993) data excluding one BAL quasar and all heavy element absorption systems. The Key Project sample has since been supplemented (Bahcall et al. 1996, Jannuzi et al. 1998) and those data have been included when appropriate in the complete archival sample of FOS spectra presented in Paper III.

The mean intensity KF93 derive from their Sample 2 ($b = 35$ km s^{-1}, β=1.48, γ=0.21) is $5.0^{+20.}_{-3.4} \times 10^{-24}$ ergs s^{-1} cm^{-2} Hz^{-1} sr^{-1}. This result is lower than ours for $z < 1$ by a factor of ~ 13, though the errors are large on both results are large enough that they are consistent. We use 162 lines in our low redshift solution for $J(\nu_0)$, 65 more than KF93.

7.4.2. Direct Measurements

Several authors have examined the sharp cutoffs observed in the HI disks of galaxies in the context of using these signatures to infer the local ionizing background (Maloney 1993, Corbelli & Salpeter 1993, Dove & Shull 1994). The truncations are modeled as arising primarily from photoionization of the disk gas by the local extragalactic background radiation field. Using 21 cm observations (Corbelli, Scheider, & Salpeter 1989, van Gorkom 1993) to constrain these models, limits on the local ionizing background are placed at $10^4 < \Phi_{\rm ion} < 5 \times 10^4$ cm^{-2} s^{-1}, where

$$\Phi_{\rm ion} = 2\pi \int_0^1 \mu d\mu \int_{\nu_0}^{\infty} \frac{J_\nu}{h\nu} d\nu = \frac{\pi J(\nu_0)}{h\alpha_s}, \tag{20}$$

and where $J_\nu = I_\nu$ for an isotropic radiation field.

Additionally, narrow-band and Fabry-Perot observations of Hα emission from intergalactic clouds (Stocke et al. 1991, Bland-Hawthorn et al. 1994, Vogel et al. 1995, Donahue, Aldering, & Stocke 1995) place limits of $\Phi_{\rm ion} \lesssim 10^4$ cm^{-2} s^{-1}, or $J(\nu_0) < 7.6 \times 10^{-23}$ ergs s^{-1} cm^{-2} Hz^{-1} sr^{-1} for $\alpha_s = 1.8$, while results from measurements of Galactic high velocity clouds (Kutyrev & Reynolds 1989, Songaila, Bryant, & Cowie 1989, Tufte, Reynolds, & Haffner 1998) imply $\Phi_{\rm ion} \lesssim 6 \times 10^4$ cm^{-2} s^{-1}, though the ionization of high velocity clouds may be contaminated by a Galactic stellar contribution.

Tumlinson et al. (1999) have reanalyzed the 3C273/NGC3067 field using the Hα imaging data from Stocke et al. (1991) as well as new GHRS spectra of 3C273, in order to model the ionization balance in the absorbing gas in the halo of NGC3067. From this analysis, they derive the limits, $2600 < \Phi_{\rm ion} < 10^4$ cm^{-2} s^{-1}, or $10^{-23} < J(\nu_0) < 3.8 \times 10^{-23}$ ergs s^{-1} cm^{-2} Hz^{-1} sr^{-1} at $z = 0.0047$. Weymann et al. (2001) have recently reported an upper limit of $\Phi_{\rm ion} < 1.01 \times 10^4$ cm^{-2} s^{-1}, or $J(\nu_0) < 3.84 \times 10^{-23}$ ergs s^{-1} cm^{-2} Hz^{-1} sr^{-1} from

Fabry-Perot observations of the intergalactic HI cloud, 1225+01, for a face-on disk geometry. If an inclined disk geometry is assumed, this lower limit becomes $J(\nu_0) < 9.6 \times 10^{-24}$ ergs s^{-1} cm^{-2} Hz^{-1} sr^{-1}. These results are summarized in Figure 16. It is encouraging that the proximity effect value is consistent with the limits on the background set by these more direct estimates which are possible locally.

7.5. Comparison with Models

Haardt & Madau (1996) calculated the spectrum of the UV background as a function of frequency and redshift using a model based on the integrated emission from QSOs alone. The QSO luminosity function is drawn from Pei (1995). The opacity of the intergalactic medium is computed from the observed redshift and column density distributions of Ly-α absorbers given by Equ. 2. The effects of attenuation and reemission of radiation by hydrogen and helium in Ly-α absorbers are included in these models. Their result for $q_0 = 0.5$ and $\alpha_s = 1.8$ at $z = 0$ is $J(\nu_0) = 1.6 \times 10^{-23}$ ergs s^{-1} cm^{-2} Hz^{-1} sr^{-1}.

Fardal et al. (1998) compute opacity models for the intergalactic medium (IGM) based on high resolution observations of the high redshift Ly-α forest from several authors. Shull et al. (1999) extend the models of Fardal et al. (1998) to $z = 0$, treating opacity of low redshift Ly-α forest from observations made with HST/GHRS (Penton et al. 2000a,b) and with HST/FOS (Weymann et al. 1998). Like Haardt & Madau (1996), they also incorporate the observed redshift distribution of Lyman limit systems with $\log(N_{HI}) > 17$ (Stengler-Larrea et al. 1995, Storrie-Lombardi et al. 1994). Their models also allow for a contribution from star formation in galaxies in addition to AGN. The QSO luminosity function again is taken to follow the form given by Pei (1995) with upper/lower cutoffs at 0.01/10 L_*. QSO UV spectral indicies are assumed to equal 0.86, while the ionizing spectrum at $\nu > \nu_0$ has $\alpha_s = 1.8$. The contribution to the background from stars was normalized to the Hα luminosity function observed by Gallego et al. (1995) and the escape fraction of photons of all energies from galaxies was taken to be $< f_{\rm esc} >= 0.05$. The full radiative transfer model described in Fardal et al. (1998) was used to calculate the contribution to the mean intensity by AGN, but not the contribution from stars, as they were assumed to contribute no flux above 4 Ryd, the energies at which the effects of IGM reprocessing become important. These authors find $J(\nu_0) = 2.4 \times 10^{-23}$ ergs s^{-1} cm^{-2} Hz^{-1} sr^{-1} at $z \sim 0$, with approximately equal contributions from AGN and stars, a value somewhat lower than our result for $z < 1$, but which is allowed within the errors.

We estimate the contribution to the UV background from star-forming galaxies using the galaxy luminosity function of the Canada-France Redshift Survey (Lilly et al. 1995). At

$z \sim 0.5$, we derive $J^{\rm gal}(\nu_0) = 1.5 \times 10^{-22}$ ergs s^{-1} cm^{-2} Hz^{-1} sr^{-1}, assuming $< f_{\rm esc} >= 1$. The HM96 models for the QSO contribution give $J^{\rm QSO}(\nu_0) = 5.2 \times 10^{-23}$ ergs s^{-1} cm^{-2} Hz^{-1} sr^{-1} at $z \sim 0.5$. These estimates, and the range of measured $J(\nu_0)$ in this paper, $\sim 5 - 16 \times 10^{-23}$ ergs s^{-1} cm^{-2} Hz^{-1} sr^{-1} imply an escape fraction of UV photons from galaxies between 4% and 70%. The $J(\nu_0)$ inferred from $d\mathcal{N}/dz$ in Section 7.3 implies escape fractions well over 100%.

Bianchi et al. (2001) make updated estimates of the mean intensity of the background with contributions from both QSOs and star-forming galaxies. Their models incorporate various values of the escape fraction of Lyman continuum photons from galaxies which are constant with redshift and wavelength. Our new results at $z < 1.7$ are most consistent with their models of the QSO contribution alone, though some contribution from galaxies, ie. a small $f_{\rm esc}$, is allowed within the uncertainties. At $z \sim 3.5$, recent results from Steidel, Pettini, & Adelberger (2001) on the Lyman-continuum radiation from high redshift galaxies suggest that these sources become a more important component of the UV background at high redshift.

7.6. Systematics

Drawing on lessons learned from our work on high redshift objects in Paper II, we have made corrections for quasar systemic redshifts before performing the proximity effect analysis, as discussed in §3. This correction, $\sim$ 300 km s^{-1}, was made to QSO redshifts measured from Ly-α emission for objects for which no systemic redshift measurement was available. For the low redshifts considered in this paper, redshifts measured from [OIII], MgII, or Balmer emission lines were deemed suitable as QSO systemic redshift measurements.

We have removed known gravitational lenses from the sample. As discussed above, we perform the proximity effect analysis omitting and including spectra that show associated absorption and damped Ly-α absorption and determined that neither of these populations significantly biases our results.

Because we are working with low redshift data where line densities are low, we expect that blending has not contributed as strong a systematic effect as in the high redshift sample of Paper II. The curve-of-growth effects discussed in Paper II may still be present, since many lines in the sample have equivalent widths which place them on the flat part of the curve of growth.

However, the effects of clustering may be even more important at low redshift than at high redshift. Loeb & Eisenstein (1995) showed how the fact that quasars reside in the dark matter potentials of galaxies and small groups of galaxies can influence the proximity effect signature. The peculiar velocities of matter clustered in these potentials can result in Ly-α absorption at redshifts greater than the quasar emission redshift. We found that including associated absorbers in our sample did not significantly change our results. Recently, Pascarelle et al. (2001) report evidence for a lower incidence of Ly-α absorption lines arising in the gaseous halos of galaxies in the vicinities of QSOs than in regions far from QSOs. They argue that galaxy-QSO clustering may lead proximity effect measurements to overestimate $J(\nu_0)$ at $z < 1$ by a up to a factor of 20. While we agree that most systematic effects in this type of analysis, including clustering, will lead to overestimates of $J(\nu_0)$, the agreement between our results and the direct measurements discussed in Section 7.4.2 give us confidence that our results are not biased by this large a factor.

The hydrodynamic simulations of the low redshift Ly-α forest of Davé et al. (1999) indicate that, at low redshift, structures of the same column density correspond to larger overdensities and more advanced dynamical states than at high redshift. For a $(\Omega_{\rm M}, \Omega_\Lambda) = (0.4, 0.6)$ cosmology, an equivalent width limit of 0.32 Å corresponds to an overdensity of ~ 1.4 at $z \sim 3$, while at $z \sim 0.6$, this limit corresponds to $\rho_H/\overline{\rho_H} \sim 13$. This may have implications on the clustering of Ly-α absorption lines around QSOs and hence on the values of $J(\nu_0)$ derived from the proximity effect. It is possible that we are seeing this clustering effect in the variable threshold solution at $z > 1$, in which the two highest $\omega(z)$ lines in the sample are responsible for the inability to isolate a reasonable maximum likelihood $J(\nu_0)$.

8. Summary

We have analyzed a set of 151 QSOs and 906 Ly-α absorption lines, the subset of the total data set presented in Paper III that is appropriate for the proximity effect. The primary results of this paper are as follows:

(1) At low redshift, Balmer, [OIII], and Mg II emission lines are reasonable indicators of QSO systemic redshifts. Ly-α emission is blueshifted by ~ 300 km s^{-1} with respect to [OIII].

(2) The value of $J(\nu_0)$ is observed to increase with redshift over the redshift range of the sample data, $0.03 < z < 1.67$. Dividing the sample at $z = 1$, we find $J(\nu_0) = 6.5^{+38.}_{-1.6} \times 10^{-23}$ ergs s^{-1} cm^{-2} Hz^{-1} sr^{-1}, at low redshift and $J(\nu_0) = 1.0^{+3.8}_{-0.2} \times 10^{-22}$ ergs s^{-1} cm^{-2} Hz^{-1} sr^{-1} at high redshift.

(3) The inclusion of blazars at $z < 1$ has no significant effect on the result. There is no significant difference between the values of $J(\nu_0)$ derived from radio loud (RL > 1.0) and

radio quiet (RL < 1.0) objects, indicating that the observed richness of quasar environments does not distinctly bias the proximity effect analysis.

(4) Using information measured and gathered from the literature on each QSO's UV spectral index and solving for the HI ionization rate, yields 1.9×10^{-13} s^{-1} for $z < 1$ and 1.3×10^{-12} s^{-1} for and $z > 1$. Solving directly for the parameters $(A_{\rm HM}, B_{\rm HM}, z_c, S)$ in the HM96 parametrization of $\Gamma(z)$ using the HST/FOS data presented by Bechtold et al. (2001) combined with the high redshift, ground-based data presented by Scott et al. (2000a,b) results in $(A_{\rm HM}, B_{\rm HM}, z_c, S) = (7.6 \times 10^{-13},\ 0.35,\ 2.07,\ 1.77)$ for $\beta = 1.46$ and $(A_{\rm HM}, B_{\rm HM}, z_c, S) = (3.2 \times 10^{-13},\ 1.45,\ 2.13,\ 1.42)$ for $\beta = 1.7$ for $1.7 < z < 3.8$.

(5) Allowing for a varying equivalent width threshold across each QSO spectrum results in consistently higher values of $J(\nu_0)$ than are found from the constant threshold treatments. At $z > 1$, the variable threshold solution is not well-constrained. Jackknife experiments indicate that this is due the objects 0743-6719 and 0302-2223, namely the highest $\omega(z)$ absorption lines in each of their spectra.

(6) Allowing for a cosmology in which $(\Omega_{\rm M}, \Omega_\Lambda) = (0.3, 0.7)$, rather than (1.,0.) has no significant effect on the value of $J(\nu_0)$ derived from these data.

(7) The $z < 1$ result is in agreement with the range of values of the mean intensity of the hydrogen-ionizing background allowed by a variety of local estimates, including Hα imaging and modeling of galaxy HI disk truncations. To within the uncertainty in the measurement, this result agrees with the one previous proximity effect measurement of the low redshift UV background (KF93). These results are consistent with calculated models based upon the integrated emission from QSOs alone (HM96) and with models which include both QSOs and starburst galaxies (Shull et al. 1999). The uncertainties do not make a distinction between these two models possible.

(8) The results presented here tentatively confirm the IGM evolution scenario provided by large scale hydrodynamic simulations (Davé et al. 1999). This scenario, which is successful in describing many observed properties of the low redshift IGM, is dependent upon an evolving $J(\nu_0)$ which decreases from $z = 2$ to $z = 0$. However, the low redshift UV background required to match the observations of the evolution of the Ly-α forest line density is larger than found from the data, indicating that structure formation is playing a role in this evolution as well. Our results and the work of others are summarized in Figure 16. We find some evidence of evolution in $J(\nu_0)$, though it appears that even larger data sets, especially at $z < 1$ and/or improved proximity effect ionization models will be required to improve the significance.

The authors thank the anonymous referee for a careful review of the paper and for helpful suggestions. This research has made use of the NASA/IPAC Extragalactic Database (NED) which is operated by the Jet Propulsion Laboratory, California Institute of Technology, under contract with the National Aeronautics and Space Administration. This project was supported by STScI grant No. AR-05785.02-94A and STScI grant No. GO 066060195A. JS acknowledges support of the National Science Foundation Graduate Research Fellowship and the Zonta Foundation Amelia Earhart Fellowship. JS, JB, and MM received financial support from NSF grant AST-9617060B. AD acknowledges support from NASA Contract No. NAS8-39073 (CXC). VPK acknowledges partial support from an award from the William F. Lucas Foundation and the San Diego Astronomers' Association.

REFERENCES

Aldcroft, T. L., Bechtold, J., & Elvis, M. 1994, ApJS, 93, 1

Appenzeller, I., Krautter, J., Mandel, H., Bowyer, S., Dixon, W. V., Hurwitz, M., Barnstedt, J., Grewing, M., Kappelmann, N., & Krm̈er, G. 1998, ApJ, 500, L9

Babu, G. J. & Feigelson, E. D. 1996, Astrostatistics, (London: Chapman & Hall)

Bahcall, J. N., Jannuzi, B. T., Schneider, D. P., Hartig, G. F., Bohlin, R., Junkkarinen, V. 1991, ApJ, 377, L5

Bahcall, J. N., Bergeron, J., Boksenberg, A., Hartig, G. F., Jannuzi, B. T., Kirhakos, S., Sargent, W. L. W., Savage, B. D., Schneider, D. P., Turnshek, D. A., Weymann, R. J., & Wolfe, A. M. 1993, ApJS, 87, 1

Bahcall, J. N., Bergeron, J., Boksenberg, A., Hartig, G. F., Jannuzi, B. T., Kirhakos, S., Sargent, W. L. W., Savage, B. D., Schneider, D. P., Turnshek, D. A., Weymann, R. J., & Wolfe, A. M. 1996, ApJ, 457, 19

Bajtlik, S., Duncan, R. C., & Ostriker, J. P. 1988, ApJ, 327, 570 (BDO)

Barthel, P. D., Tytler, D., & Thompson, B. 1990, A&AS, 82, 339

Basu, D. 1994, Ap&SS, 222, 91

Bechtold, J. 1994, ApJS, 91, 1 (B94)

Bechtold, J., Dobrzycki, A., Wilden, B., Morita, M., Scott, J., Dobrzycka, D., & Tran, K.-V., Aldcroft, T. L. 2001, ApJ, in press (Paper III, astro-ph/0111486)

Bi, H. & Davidsen, A. 1997, ApJ, 479, 523

Bianchi, S., Cristiani, S., & Kim, T. -S. 2001, A&A, 376, 1

Bland-Hawthorn, J., Taylor, K., Veilleux, S., & Shopbell, P. L. 1994, ApJ, 437, L95

Bolton, J. G., Peterson, B. A., Wills, B. J., Wills, D. 1976, ApJ, 210, L1

Browne, I. W. A., Savage, A., & Bolton, J. G. 1975, MNRAS, 173, 87P

Bryan, G. L., Machacek, M., Anninos, P., & Norman, M. L. 1999, ApJ, 517, 13

Bunker, A. J., Marleau, F. R., & Graham, J. R. 1998, AJ, 116, 2086

Burbidge, E. M. & Kinman, T. D. 1966, ApJ, 145, 654

Burstein, D. & Heiles, C. 1982, AJ, 87, 1165

Buson, L. M. & Ulrich, M.-H. 1990, A&A 240, 247

Carswell, R. F., Webb, J. K., Baldwin, J. A., & Atwood, B. 1987, ApJ, 319, 709

Cen, R., Miralda-Escudé, J., Ostriker, J. P., & Rauch, M. 1994, ApJ, 437, L9

Chen, H.- W., Lanzetta, K. M., Webb, J. K., & Barcons, X. 1998, ApJ, 498, 77

Cheng, F. H., You, J. H., & Yan, M. 1990, ApJ, 358, 18

Cooke, A. J., Espey, B., & Carswell, R. F. 1997, MNRAS, 284, 552

Corbelli, E., Schneider, S. E, & Salpeter, E. E. 1989, AJ, 97, 390

Corbelli, E. & Salpeter, E. E. 1993, ApJ419, 104

Corbin, M. R. 1997, ApJS, 113, 245

Corbin, M. R. & Boroson, T. A. 1996, ApJ, 107, 69

Cristiani, S. & Koehler, B. 1987, A&AS, 68, 339

Cristiani, S., D'Odorico, S., Fontana, A., Giallongo, E., & Savaglio, S. 1995, MNRAS, 273, 1016

Davé, R., Hernquist, L., Katz, N., & Weinberg, M. 1999, ApJ, 511, 521

Dobrzycki, A., Bechtold, J., Scott, J., & Morita, M. 2001, ApJ, in press (Paper IV, astro-ph/0111487)

Donahue, M., Aldering, G., & Stocke, J. T. 1995, ApJ, 450, L45

Dove, J. B. & Shull, J. M. 1994, ApJ, 423, 196

Efron, B. 1982, The Jackknife, the Bootstrap, and Other Resampling Plans, (Philadelphia: Society for Industrial and Applied Mathematics)

Ellingson, E., Yee, H. K. C., & Green, R. F. 1991, ApJ, 371, 49

Fabricant, D., Cheimets, P., Caldwell, N., & Geary, J. 1998, PASP, 110 79

Falomo, R., Pesce, J. E., & Treves, A. 1993, ApJ, 411, L63

Fardal, M., Giroux, M., & Shull, J. M. 1998, AJ, 115, 2206

Fernández-Soto, A., Barcons, X., Carballo, R., & Webb, J. K. 1995, MNRAS, 277, 235

Gallego, J. M., Zamorano, J., Aragón-Salamanca, A., & Rego, M. 1995, ApJ, 455, L1

Gaskell, C. M. 1982, ApJ, 263, 79

Giallongo, E., Cristiani, S., Fontana, A., & Trèvese, D. 1993, ApJ, 417, 137

Giallongo, E., Cristiani, S., D'Odorico, S., Fontana, A., & Savaglio, S. 1996, ApJ, 466, 46

Green, R. F., Schmidt, M., & Liebert, J. 1986, ApJS, 61, 305

Green, P. J. 1996, ApJ, 467, 61

Haardt, F. & Madau, P. 1996, ApJ, 461, 20 (HM96)

Hamann, F., Zuo, L., & Tytler, D. 1995, ApJ, 444, L69

Hernquist, L., Katz, N., Weinberg, D., Miralda-Escudé, J. 1996, ApJ, 457, L51

Hewitt, A. & Burbidge, G. 1987, ApJS, 63, 1

Hu, E. M., Kim, T. -S., Cowie, L. L., & Songaila, A. 1995, AJ, 110, 2553

Impey, C. D., Petry, C. E., & Flint, K. P. 1999, ApJ, 524, 5361

Jannuzi, B. T., Bahcall, J. N., Bergeron, J., Boksenberg, A., Hartig, G. F., Kirhakos, S., Sargent, W. L. W., Savage, B. D., Schneider, D. P., Turnshek, D. A., Weymann, R. J., & Wolfe, A. M. 1998, ApJS, 118, 1

Jauncey, D. L., Wright, A. E., Peterson, B. A., & Condon, J. J. 1978, ApJ, 219, L1

Kim, T.- S., Hu, E. M., Cowie, L. L., Songaila, A. 1997, AJ, 114, 1

Kim, T.- S., Cristiani, S., & D'Odorico, S. 2001, A&A, 373, 757

Kinman, T. D. & Burbidge, E. M. 1967, ApJ, 148, L59

Kinney, A. L., Bohlin, R. C., Blades, J. C., & York, D. G. 1991, ApJS, 75, 645

Knezek, P. M. & Bregman, J. N. 1998, ApJ, 115, 1737

Kulkarni, V. P. & Fall, S. M. 1993, ApJ, 413, L63 (KF93)

Kutyrev, A. S. & Reynolds, R. J. 1989, ApJ, 344, L9

Lanzetta, K. M., Turnshek, D. A., Sandoval, J. 1993, ApJS, 84, 109

Lanzetta, K. M., Bowen, D. V., Tytler, D., & Webb, J. K. 1995, ApJ, 442, 538

Lanzetta, K. M., Webb, J. K., & Barcons, X. 1996, ApJ, 456, L17

Laor, A., Bahcall, J. N., Jannuzi, B. T., Schneider, D. P., Green, R. F., & Hartig, G. F. 1994, ApJ, 420, 110

Laor, A., Bahcall, J. N., Jannuzi, B. T., Schneider, D. P., & Green, R. F. 1995, ApJS, 99, 1

Lawrence, C. R., Zucker, J. R., Readhead, A. C. S., Unwin, S. C., Pearson, T. J., Xu, W. 1996, ApJS, 107, 541

Lilly, S. J., Tresse, L., Hammer, F., Crampton, D., & Le Fèvre, O. 1995, ApJ, 455, 108

Liske, J. & Williger, G. M. 2001, MNRAS, 328, 653

Lockman, F. J. & Dickey, J. M. 1995, ADIL FL 01L (NCSA Astronomy Digital Image Library)

Loeb, A. & Eisenstein, D. J. 1995, ApJ, 448, 17L

Lu, L., Wolfe, A. M., & Turnshek, D. A. 1991, ApJ, 367, 19

Lu, L., Sargent, W. L. W., Wonble, D. S., & Takada-Hidai, M. 1996, ApJ, 472, 509

Lynds, C. R., Hill, S. J., Heere, K., & Stockton, A. 1966, ApJ, 144, 1244

Lynds, R. & Wills, D. 1968, ApJ, 153, L23

Lynds, C. R. 1971, ApJ, 164, L73

Maloney, P. 1993, ApJ, 414, 41

McDowell, J. C., Canizares, C., Elvis, M., Lawrence, A., Markoff, S., Mathur, S., & Wilkes, B. 1995, ApJ, 450, 585

McIntosh, D. H., Rix, H. -W., Rieke, M., Foltz. C. B. 1999, ApJ, 517L, 73

Miralda-Escudé, J., Cen, R., Ostriker, J. P. & Rauch, M. 1996, ApJ, 471, 582

Morris, S. L. & Ward, M. J. 1988 MNRAS, 230, 639

Morris, S. L., Weymann, R. J., Savage, B. D., & Gilliland, R. L. 1991, ApJ, 377, L21

Murdoch, H. S., Hunstead, R. W., Pettini, M., & Blades, J. C. 1986, ApJ, 309, 19

Netzer, H., Kazanas, D., Wills, B. J., Wills, D., Mingsheng, H., Brotherton, M. S., Baldwin, J. A., Ferland, G. J., & Browne, I. W. A. 1994, ApJ, 430, 191

Nishihara, E., Yamashita, T., Yoshida, M., Watanbe, E., Okumura, S.-I., Mori, A., & Iye, M. 1997, ApJ, 488, L27

Ortiz-Gil, A., Lanzetta, K. M., Webb, J. K., Barcons, X., & Fernández-Soto, A. 1999, ApJ, 523, 720

Osmer, P. S., Porter, A. C., & Green, R. F. 1994, ApJ, 436, 678

Pascarelle, S. M., Lanzetta, K. M., Chen, H. -W., & Webb, J. K. 2001, ApJ, 560, 101

Peebles, P. J. E. 1993, Principles of Physical Cosmology, (Princeton: Princeton University Press)

Pei, Y. 1995, ApJ, 438, 623

Penton, S. V., Stocke, J. T., & Shull, J. M. 2000a, ApJS, 130, 121

Penton, S. V., Shull, J. M., & Stocke, J. T. 2000b, ApJ, 544, 140

Press, W. H., Teukolsky, S. A., Vetterling, W. T., & Flannery, B. P. 1992, Numerical Recipes in Fortran 77, The Art of Scientific Computing, Second Edition, Cambridge: Cambridge University Press

de Robertis, M. 1985, ApJ, 289, 67

Sanduleak, N. & Pesch,P. 1984, ApJS, 55, 517

Sargent, W. L. W., Young, P., Boksenberg, A., & Tytler, D. 1980, ApJ, 42, 41

Savaglio, S., Cristiani, S., D'Odorico, S., Fontana, A., Giallongo, E., & Molaro, P. 1997, A&A, 318, 347

Schmidt, M. 1977, ApJ, 217, 358

Scott, J., Bechtold, J., & Dobrzycki, A. 2000a, ApJS, 130, 37 (Paper I)

Scott, J., Bechtold, J., Dobrzycki, A., & Kulkarni, V. 2000b, ApJS, 130, 67 (Paper II)

di Serego-Alighieri, S., Danziger, I. J., Morganti, R., & Tadhunter, C. N. 1994, MNRAS, 269, 998

Shull, J. M., Roberts, D., Giroux, M. L., Penton, S. V., Fardal, M. A. 1999, AJ, 118, 1450

Smith, H. E., Burbidge, E. M., Baldwin, J. A., Tohline, J. E., Wampler, E. J., Hazard, C., & Murdoch, H. S. 1977, ApJ, 215, 427

Smith, R. J., Boyle, B. J., & Maddox, S. J. 2000, MNRAS, 313, 252

Songaila, A., Bryant, W., & Cowie, L. L. 1989, ApJ, 345, L71

Stark, A. A., Gammie, C. F., Wilson, R. W., Bally, J., Linke, R. A., Heiles, C., & Hurwitz, M. 1992, ApJS, 79, 77

Steidel, C. C. & Sargent, W. L. W. 1991, ApJ, 382, 433

Steidel, C. C., Pettini, M., & Adelberger, K. L. 2001, ApJ, 546, 665

Stengler-Larrea, E. et al. 1995, ApJ, 444, 64

Stocke, J. T., Case, J., Donahue, M., Shull, J. M., & Snow, T. P. 1991, ApJ, 374, 72

Stockton, A. 1982, ApJ, 257, 33

Stockton, A. & MacKenty, J. W. 1987, ApJ, 316, 584

Storrie-Lombardi, L. J., M^{c}Mahon, R. G., Irwin, M. J., & Hazard, C. 1994, ApJ, 427, L13

Telfer, R. C., Zheng, W., Kriss, G. A., & Davidsen, A. F. 2001, ApJ, in press (astro-ph/0109531)

Theuns, T., Leonard, A., Efstathiou, G. 1998, MNRAS, 297, L49

Tufte, S. L., Reynolds, R. J., & Haffner, L. M. 1998, ApJ, 504, 773

Tumlinson, J., Giroux, M. L., Shull, J. M., & Stocke, J. T. 1999, AJ, 118, 2148

Tytler, D., Boksenberg, A., Sargent, W. L. W., Young, P., & Kunth, D. 1987, ApJS, 64, 667

Tytler, D. & Fan, X. -M. 1992, ApJS, 79, 1

Ulrich, M.- H. 1976, ApJ, 206, 364

van Gorkom, J. H. 1993, in The Environment and Evolution of Galaxies, ed. J. M Shull & H. A. Thronson (Dordrecht:Kluwer), 343

Vogel, S. N., Weymann, R., Rauch, M., & Hamilton, T. 1995, ApJ, 441, 162

Weymann, R. J., Carswell, R. F., & Smith, M. G. 1981, ARA&A, 19, 41

Weymann, R. J., Jannuzi, B. T., Lu, L., Bahcall, J. N., Bergeron, J., Boksenberg, A., Hartig, G. F., Kirhakos, S., Sargent, W. L. W., Savage, B. D., Schneider, D. P., Turnshek, D. A., & Wolfe, A. M. 1998, ApJ, 506, 1

Weymann, R. J., Vogel, S. N., Veilleux, S., & Epps, H. 2001, ApJ, 561, 559

Wilkes, B. J. 1986, MNRAS, 218, 331

Williger, G. M., Baldwin, J. A., Carswell, R. F., Cooke, A. J., Hazard, C., Irwin, M. J., McMahon, R. G., & Storrie-Lombardi, L. J. 1994, ApJ, 428, 574

Wills, D. & Wills, B. J. 1976, ApJS, 31, 143

Wold, M., Lacy, M., Lilje, P. B., & Serjeant, S. 2000, MNRAS, 316, 267

Yates, M. G., Miller, L., & Peacock, J. A. 1989, MNRAS, 240, 129

Yee, H. K. C. & Ellingson, E. 1993, ApJ, 411, 43

Yee, H. K. C. 1987, AJ, 94, 1461

Yee, H. K. C. & Green R. F. 1987, AJ, 94, 618

Yee, H. K. C. & Green R. F. 1984, ApJ, 280, 79

Young, P., Sargent, W. L. W., & Boksenberg, A. 1982, ApJ, 252, 10

Zhang, Y., Anninos, P., & Norman, M. L. 1995, ApJ, 453, L57

Zheng, W. & Sulentic, J. W. 1990, ApJ, 350, 512

Zheng, W. & Malkan, M. A. 1993, ApJ, 415, 517

Zheng, W., Kriss, G. A., Davidsen, A. F., Lee, G., Code, A. D., Bjorkman, K. S., Smith, P. S., Weistrop, D., Malkan, M. A., Baganoff, F. K., & Peterson, B. M. 1995, ApJ, 444, 632

Zheng, W., Kriss, G. A., Telfer, R. C., Grimes, J. P., & Davidsen, A. F. 1997, ApJ, 475, 469

Zotov, N. 1985, ApJ, 295, 94

This preprint was prepared with the AAS LaTeX macros v5.0.

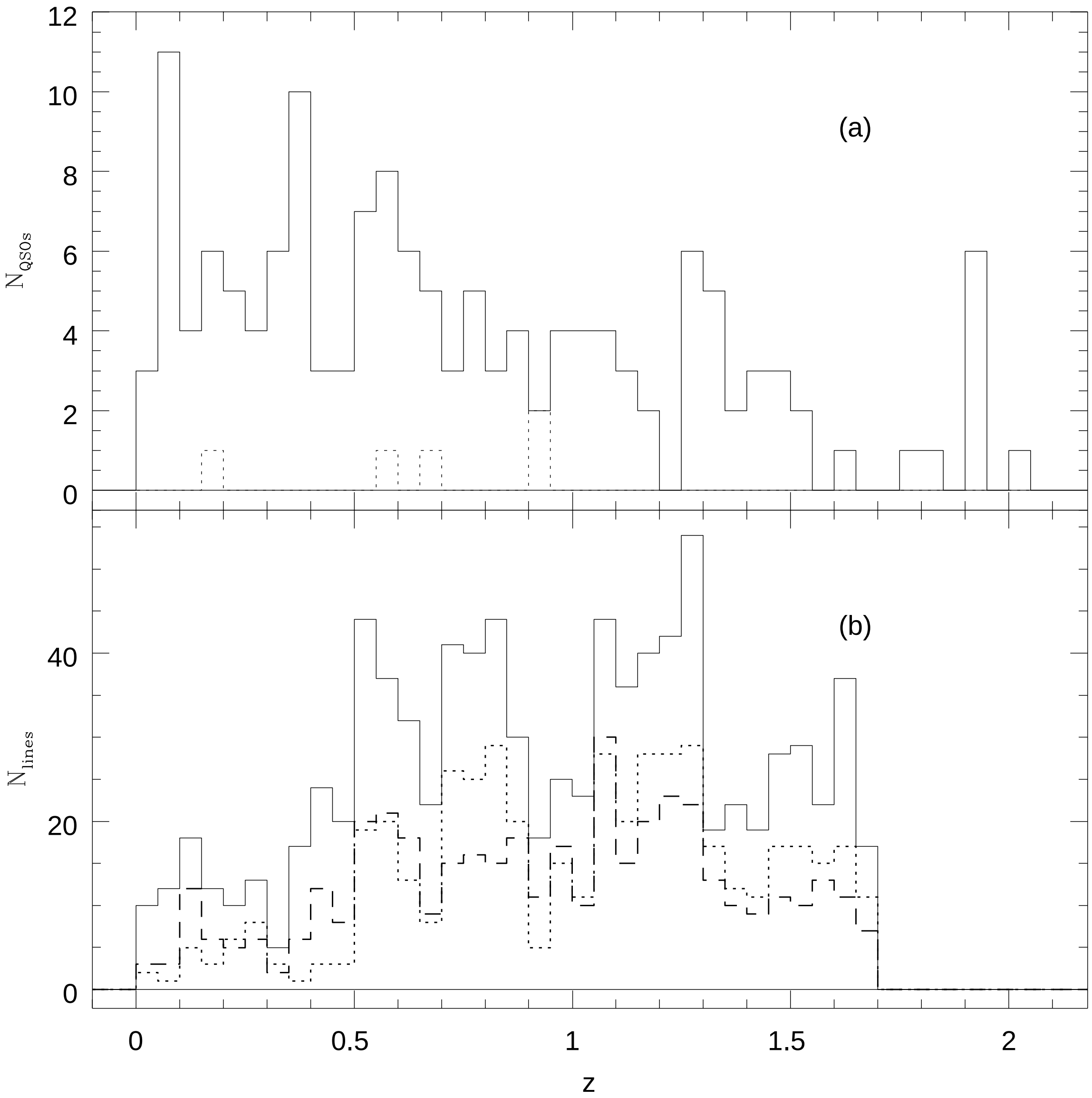

Fig. 1.— Histograms of (a) QSO redshifts in proximity effect sample, dotted line indicates objects classified as blazars or BL Lacs, and (b) Ly-α line redshifts in proximity effect sample, (solid line)- lines above variable threshold, (dashed line)- lines with $W > 0.32$ Å (dotted line)- lines with $W > 0.24$ Å

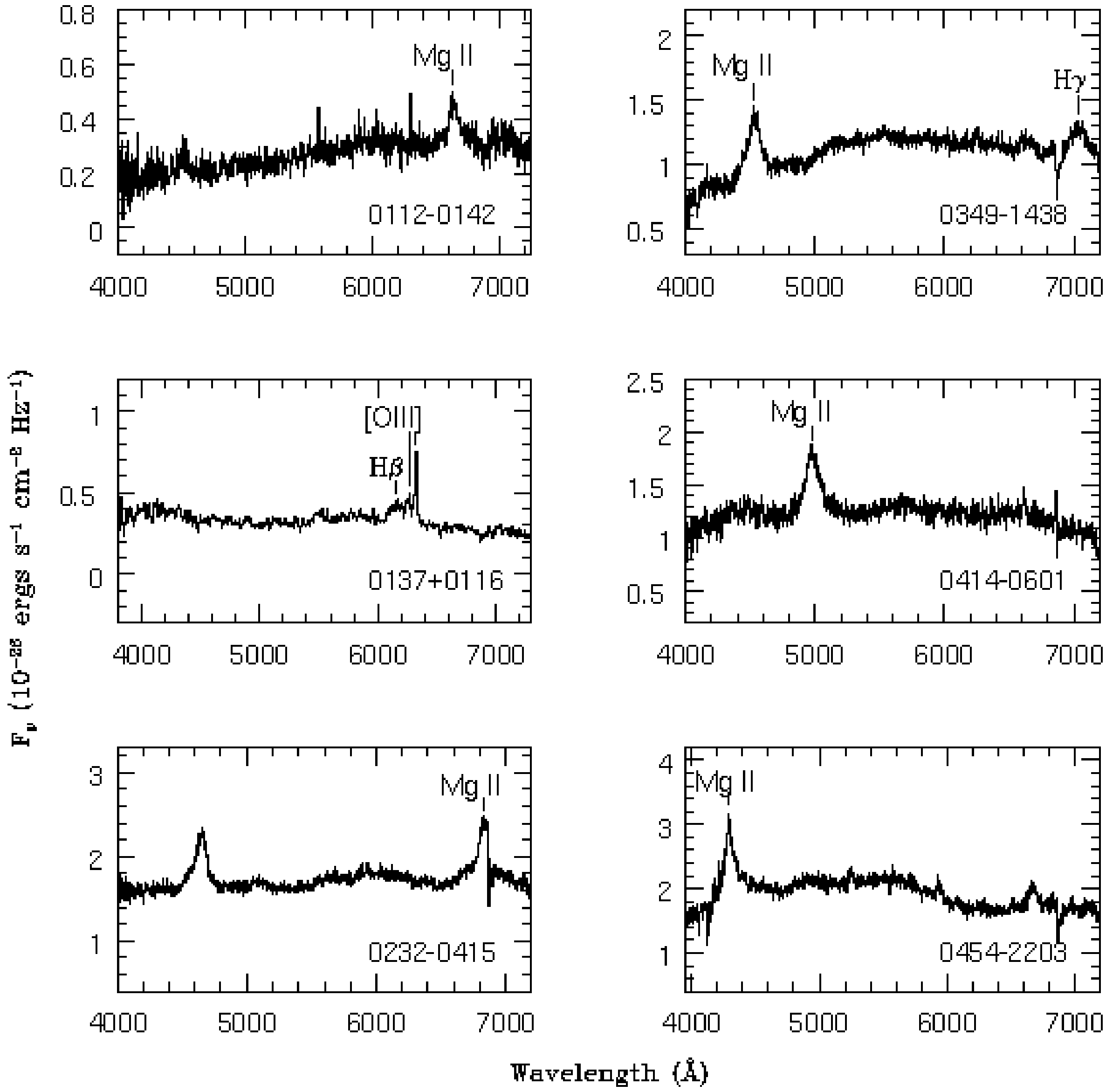

Fig. 2.— Emission line spectra of sample QSOs used to measure redshifts

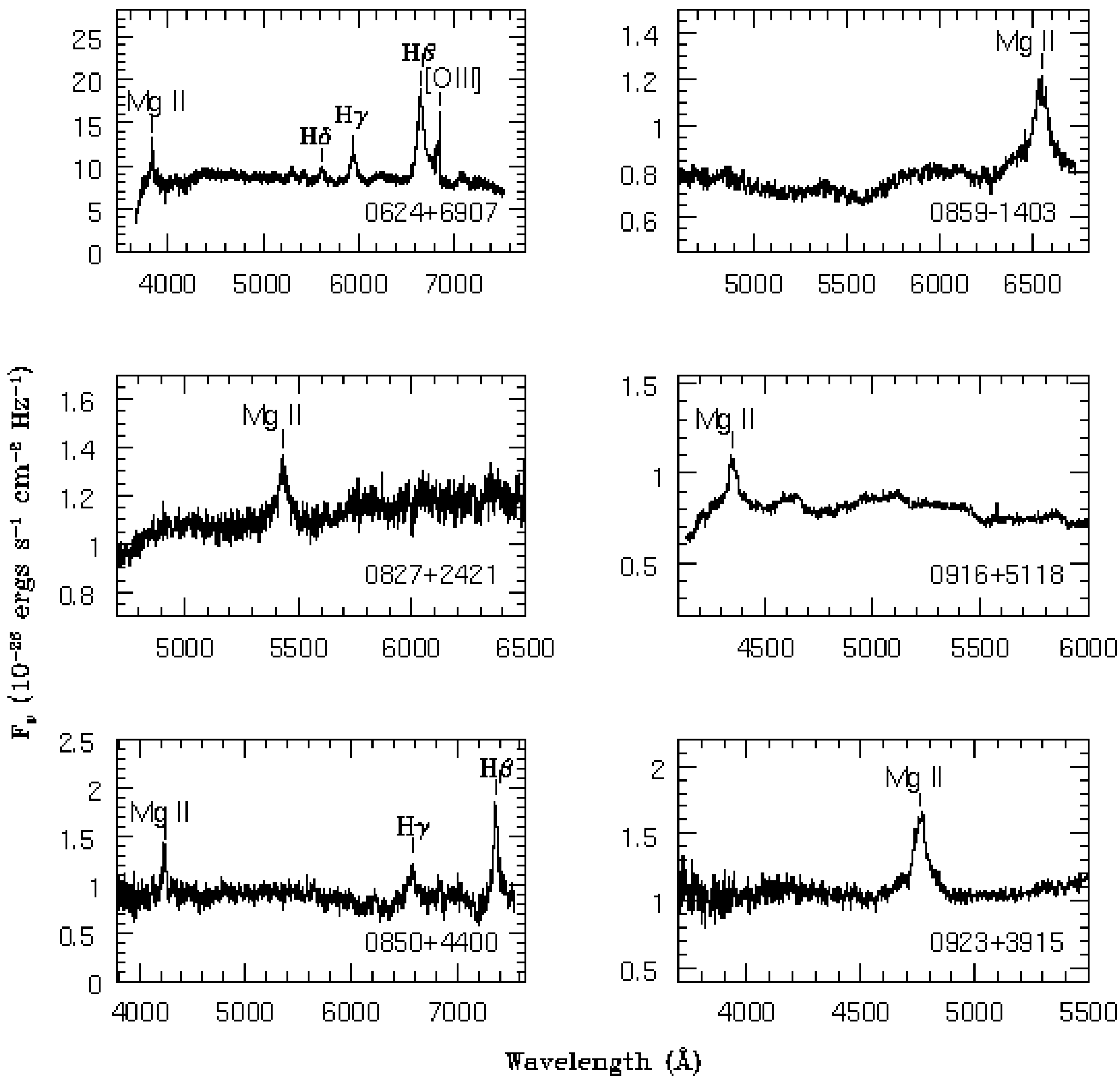
Mg II
Hδ
Hγ
Hβ
[OIII]
0624+6907
Mg II
0859-1403
Mg II
0827+2421
Mg II
0916+5118
Mg II
Hγ
Hβ
0850+4400
Mg II
0923+3915
F_ν (10^{-28} ergs s^{-1} cm^{-2} Hz^{-1})
Wavelength (Å)

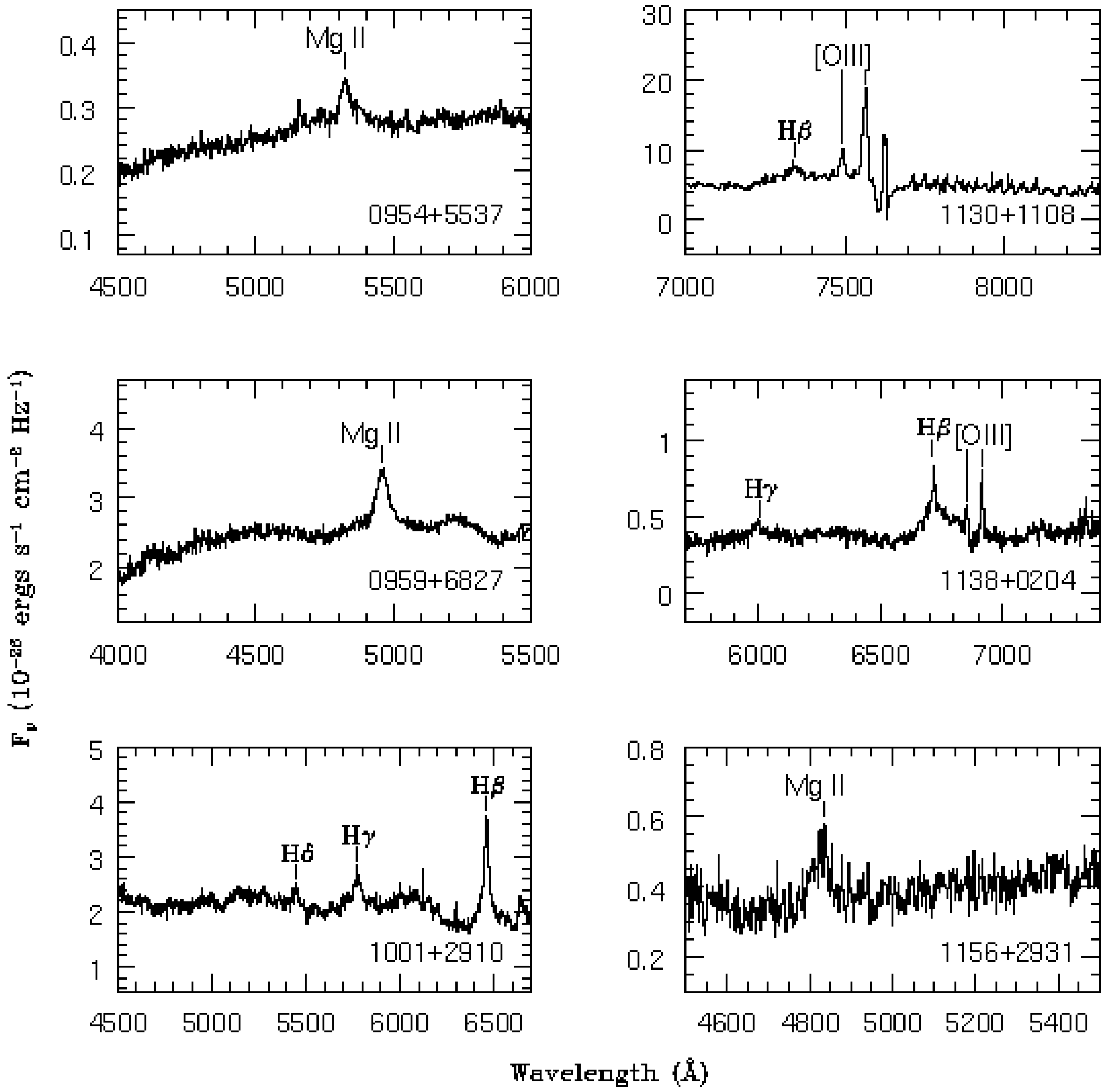
Mg II
0954+5537
[OIII]
Hβ
1130+1108
Mg II
0959+6827
Hβ
[OIII]
Hγ
1138+0204
Hδ
Hγ
Hβ
1001+2910
Mg II
1156+2931
F_ν (10^{-28} ergs s^{-1} cm^{-2} Hz^{-1})
Wavelength (Å)

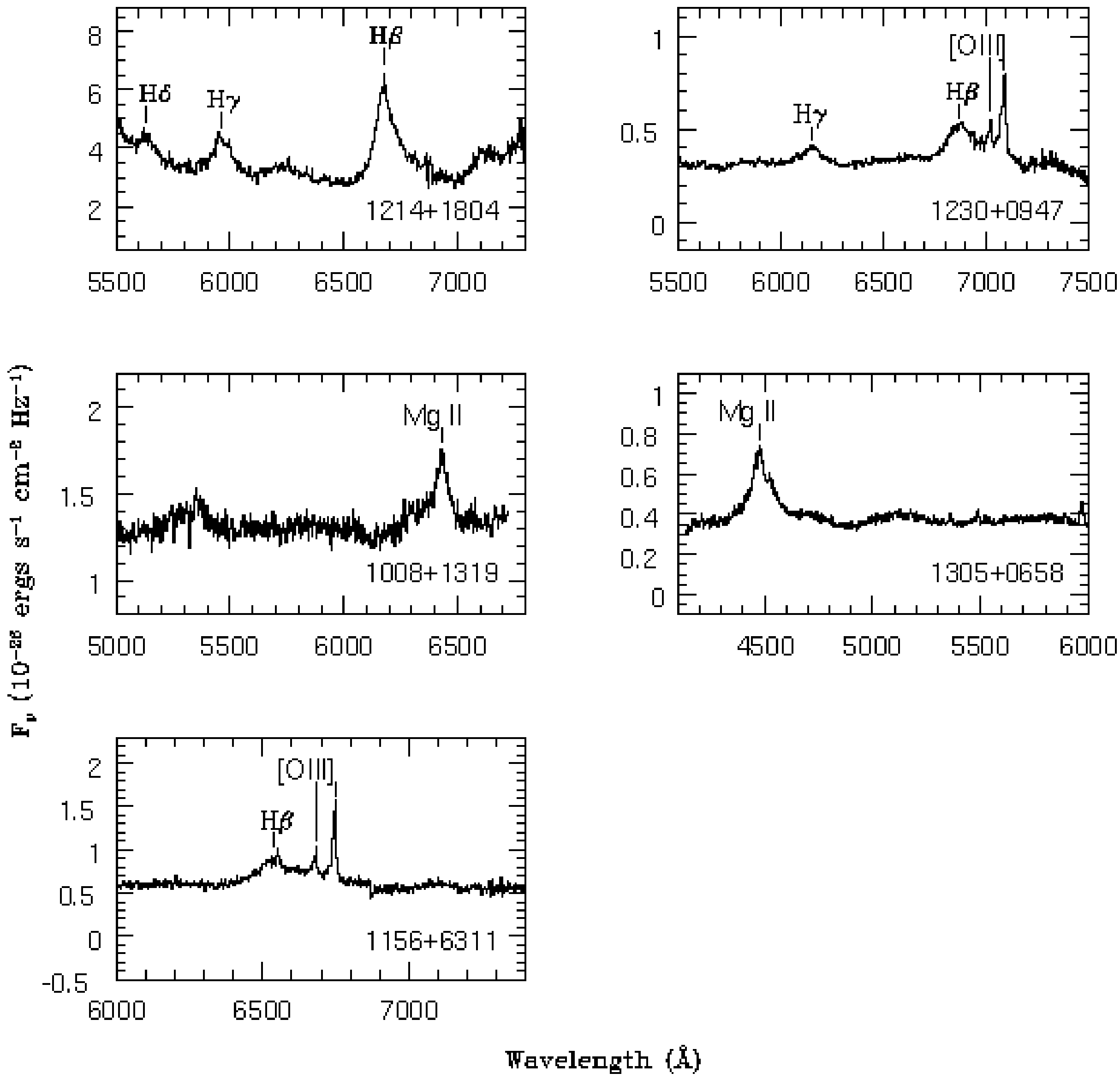
Hδ
Hγ
Hβ
1214+1804
[OIII]
Hγ
Hβ
1230+0947
Mg II
1008+1319
Mg II
1305+0658
[OIII]
Hβ
1156+6311
F_ν (10^{-28} ergs s^{-1} cm^{-2} Hz^{-1})
Wavelength (Å)

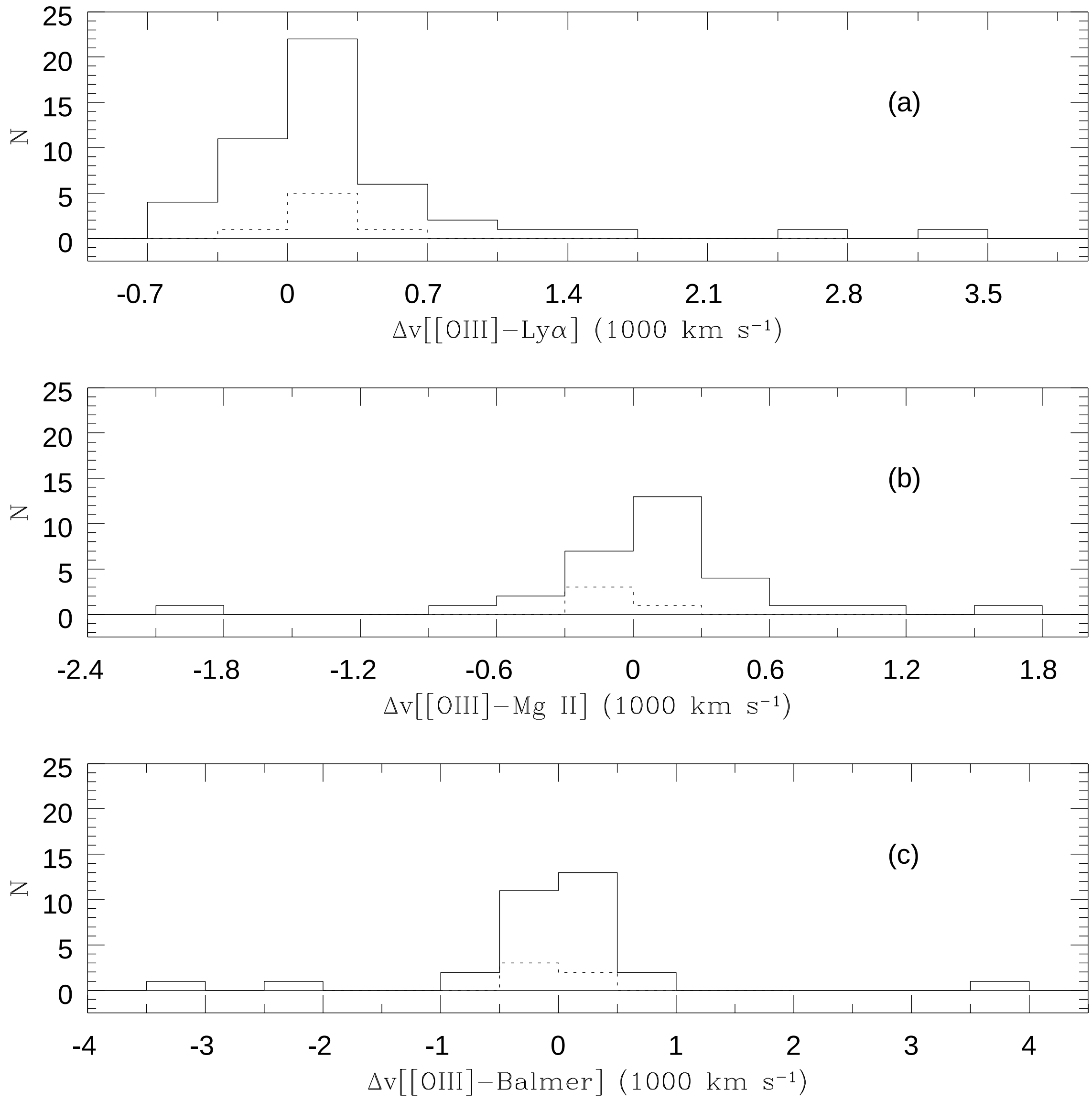

Fig. 3.— Histograms of redshift differences between [OIII] and (a) Ly-α, (b) Mg II, and (c) Balmer emission lines, dotted lines show results from Laor et al. (1995)

Available in:

`http://lithops.as.arizona.edu/~jill/QuasarSpectra/`

or

`http://hea-www.harvard.edu/QEDT/QuasarSpectra/`

Fig. 4.— FOS spectra used to extrapolate to the Lyman limit flux of each object

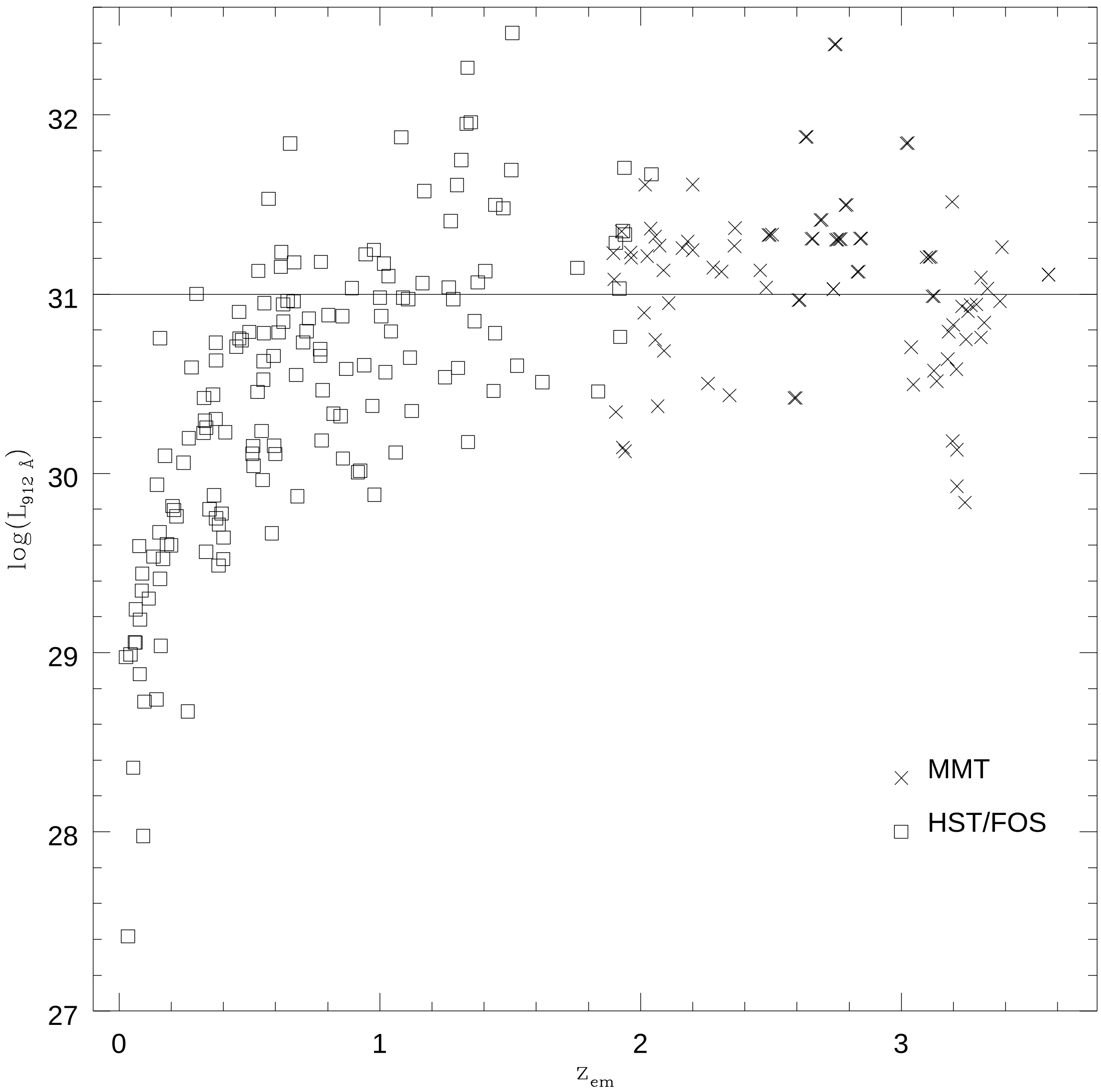

Fig. 5.— Lyman limit luminosity versus redshift for objects in the HST/FOS sample (squares) and in the MMT sample presented in Papers I and II (crosses), solid line indicates the boundary between low and high luminosity objects

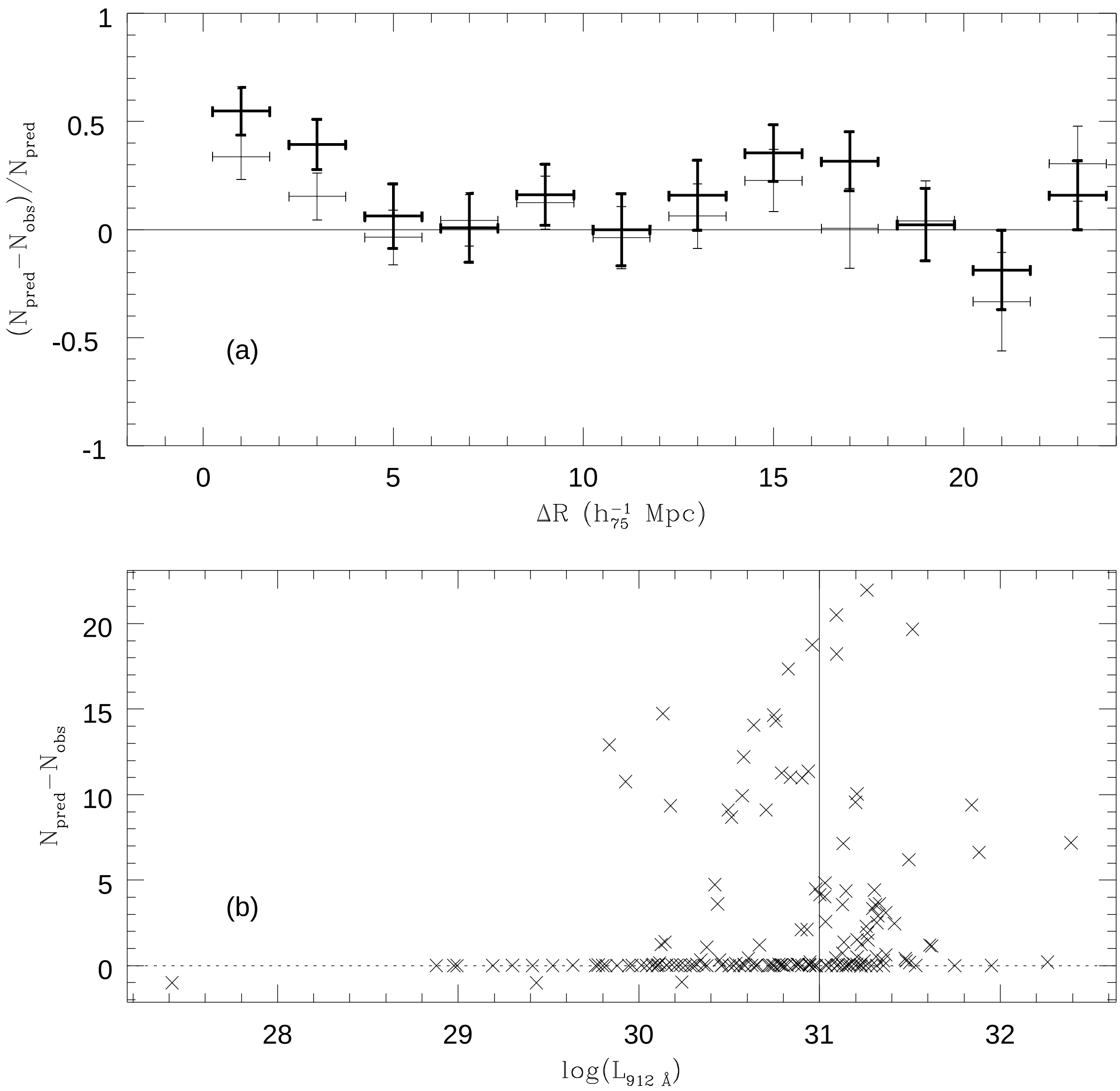

Fig. 6.— (a) Relative deficit of lines with respect to the number predicted by Equ. 1 for $W_{thr} = 0.32$ Å versus distance from the QSO for high and low luminosity QSOs (thick and thin solid lines, respectively) in both the HST/FOS sample presented in Paper III and the MMT sample presented in Paper I; (b) Deficit of lines within 2 h_{75}^{-1} Mpc as a function of QSO Lyman limit luminosity for the HST/FOS and MMT samples, the vertical line delineates the boundary between low and high luminosity objects

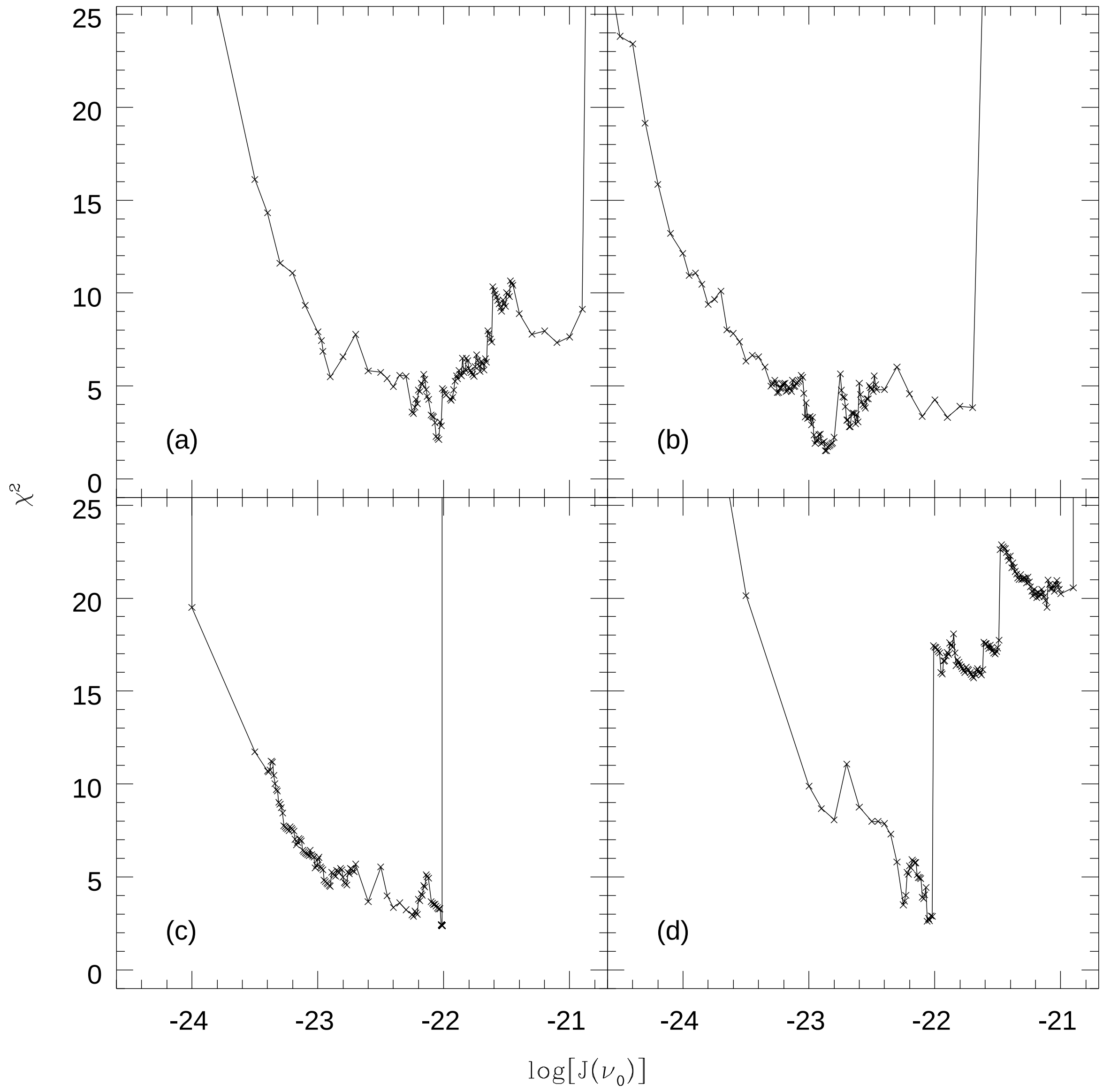

Fig. 7.— χ^2 of binned data with respect to the ionization model expressed in Equ. 11 versus $\log[J(\nu_0)]$ for various redshift ranges and equivalent width thresholds: (a) $W_{thr} = 0.32$ Å; (b) $W_{thr} = 0.32$ Å, $z < 1$; (c) $W_{thr} = 0.32$ Å, $z > 1$; (d) $W_{thr} = 0.24$ Å

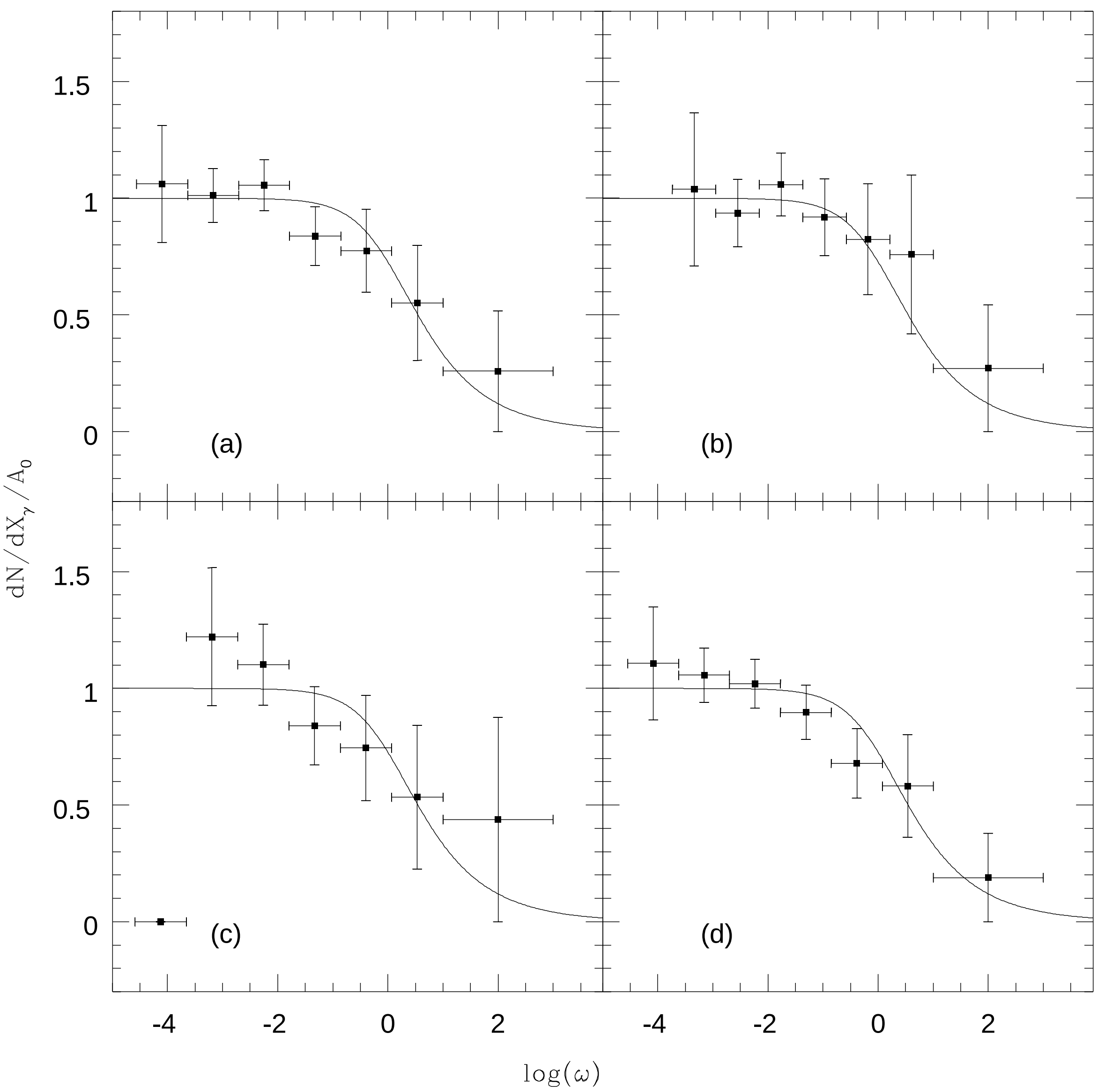

Fig. 8.— Number distribution per coevolving redshift coordinate expressed in Equ. 11 for the best fit values of $J(\nu_0)$ (BDO method); (a-d) same as Fig. 7

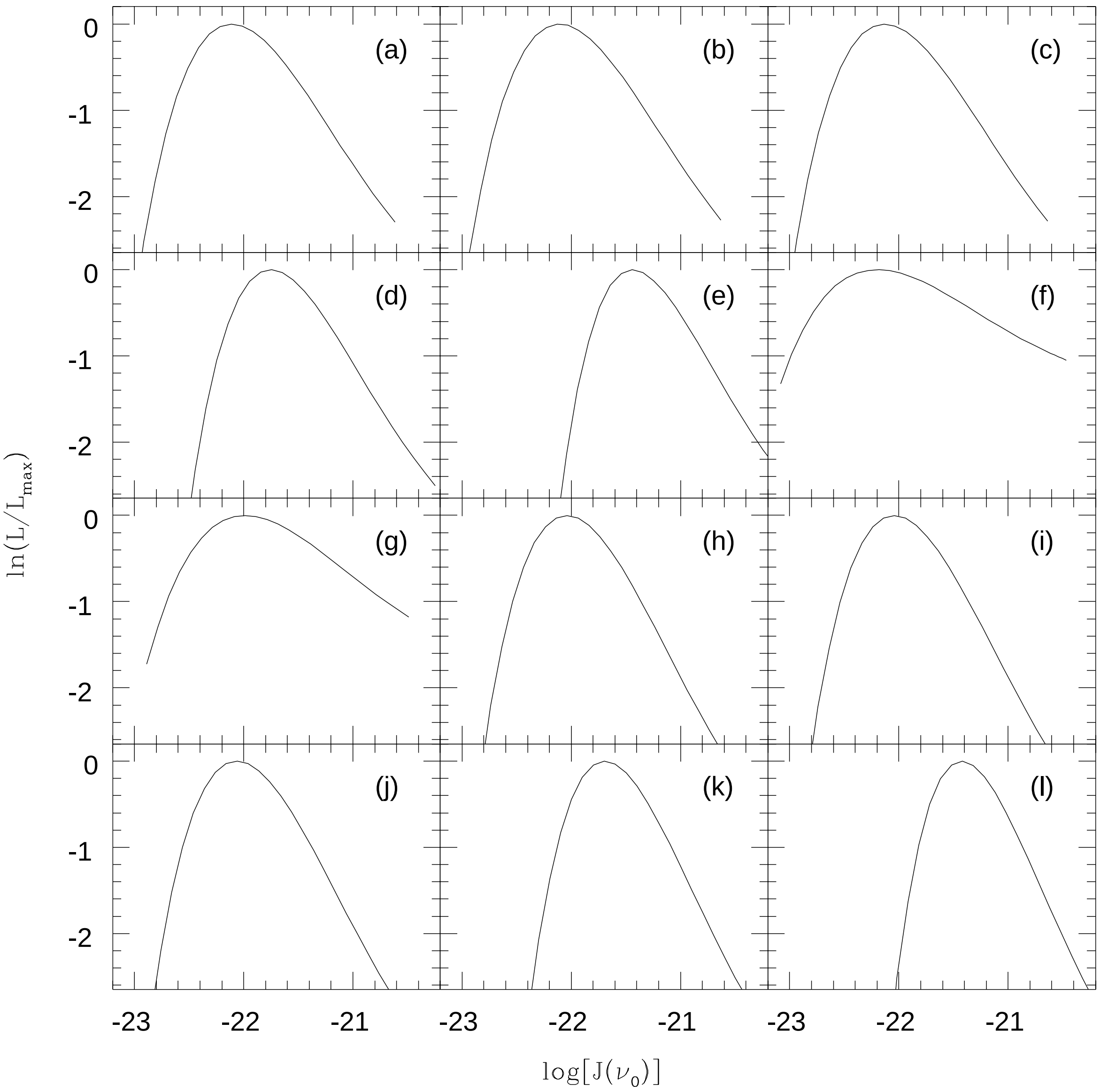

Fig. 9.— Likelihood function versus $\log[J(\nu_0)]$ for $W_{thr} = 0.32$ Å $(\beta, b) =$ (a) (1.46,35); (b) (1.46,25); (c) (1.45,25); (d) (1.70,30); (e) (2.04,25); (f) (1.46,35), $z < 1$; (g) (1.46,35), $z > 1$; and for $W_{thr} = 0.24$ Å $(\beta, b) =$ (h) (1.46,35); (i) (1.46,25); (j) (1.45,25); (k) (1.70,30); (l) (2.04,25)

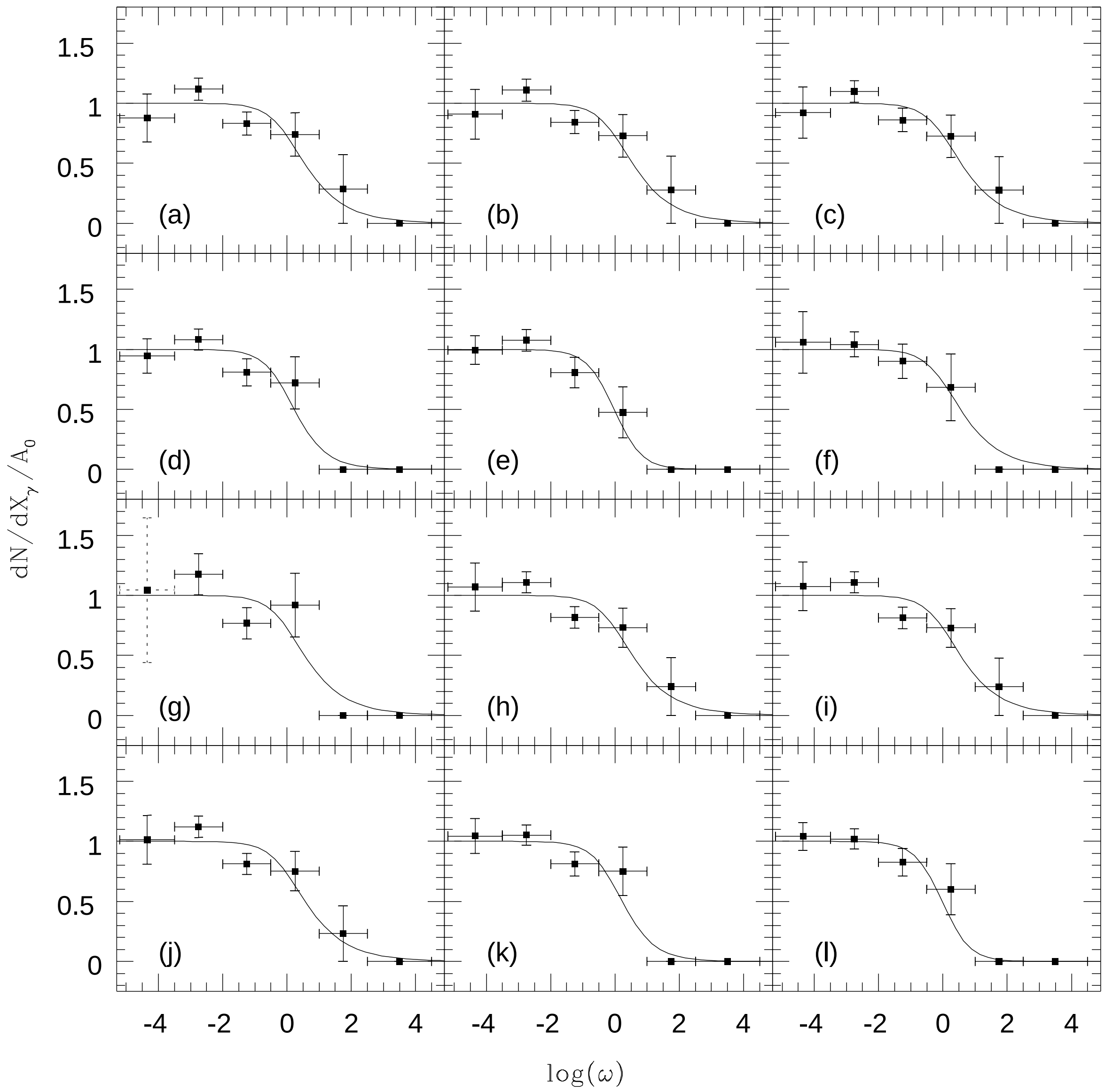

Fig. 10.— Number distribution per coevolving redshift coordinate for the best fit values of $J(\nu_0)$ (KF method); (a-l) same as Fig. 9; the dotted point and error bars in (g) has been divided by 5 for clarity

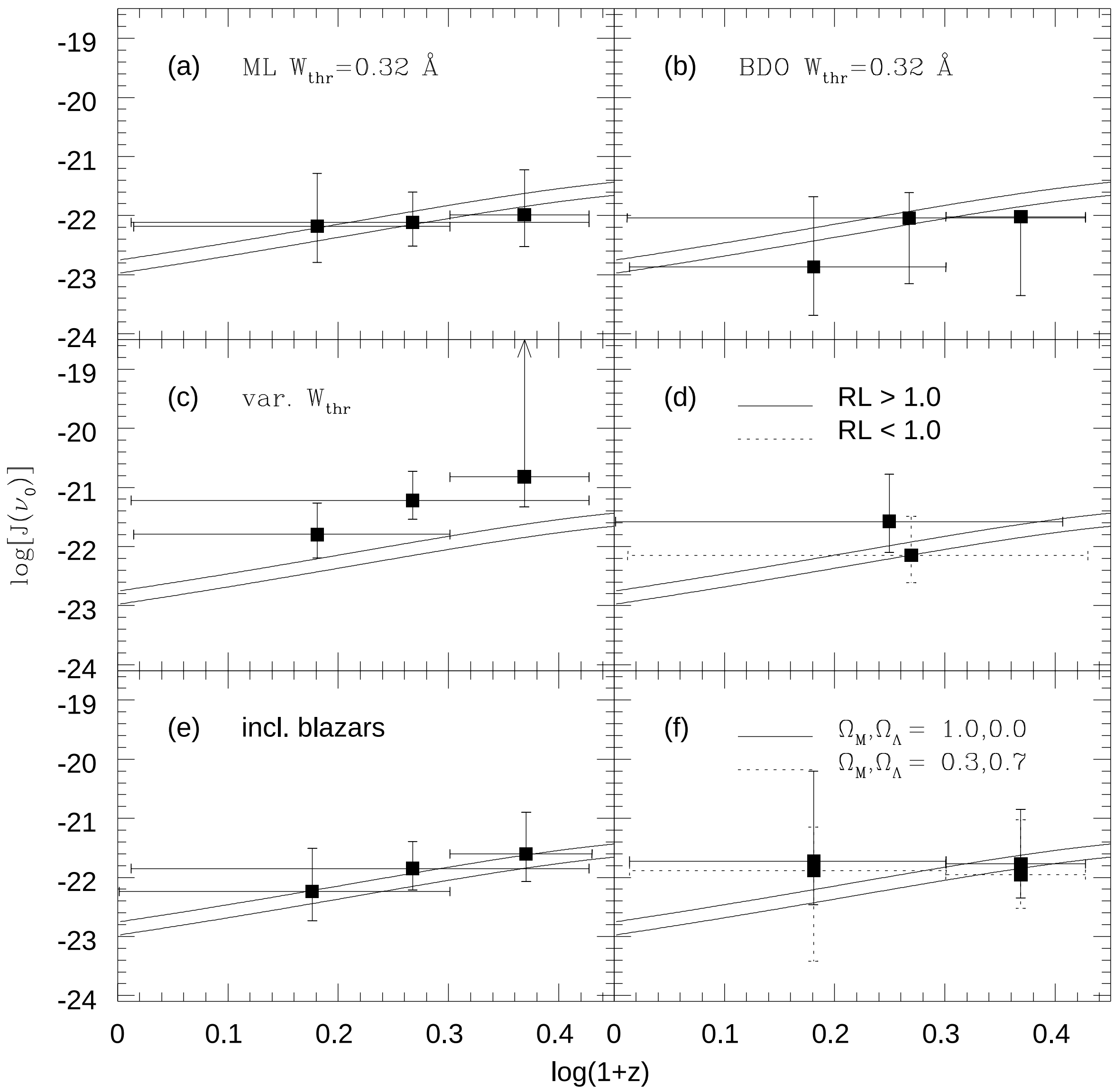

Fig. 11.— $\log[J(\nu_0)]$ versus redshift, solid curves in (a)-(f) correspond to HM96 models: (a) $W_{thr} = 0.32$ Å all redshifts, $0.03 < z < 1.67$, and $z < 1$, $z > 1$ separately, ML method; (b) same as (a), BDO method; (c) variable threshold, all redshifts $0.03 < z < 1.67$, and $z < 1$, $z > 1$ separately; (d) $W_{thr} = 0.32$ Å all redshifts, RL > 0.3 and RL < 0.3; (e) $W_{thr} = 0.32$ Å all redshifts, $0.03 < z < 1.67$, and $z < 1$, total sample including blazars; (f) $W_{thr} = 0.32$ Å $z < 1$ and $z > 1$, (solid points) $(\Omega_M, \Omega_\Lambda) = (1.0, 0.0)$, (dotted points) $(\Omega_M, \Omega_\Lambda) = (0.3, 0.7)$, metal line dz neglected in both cases

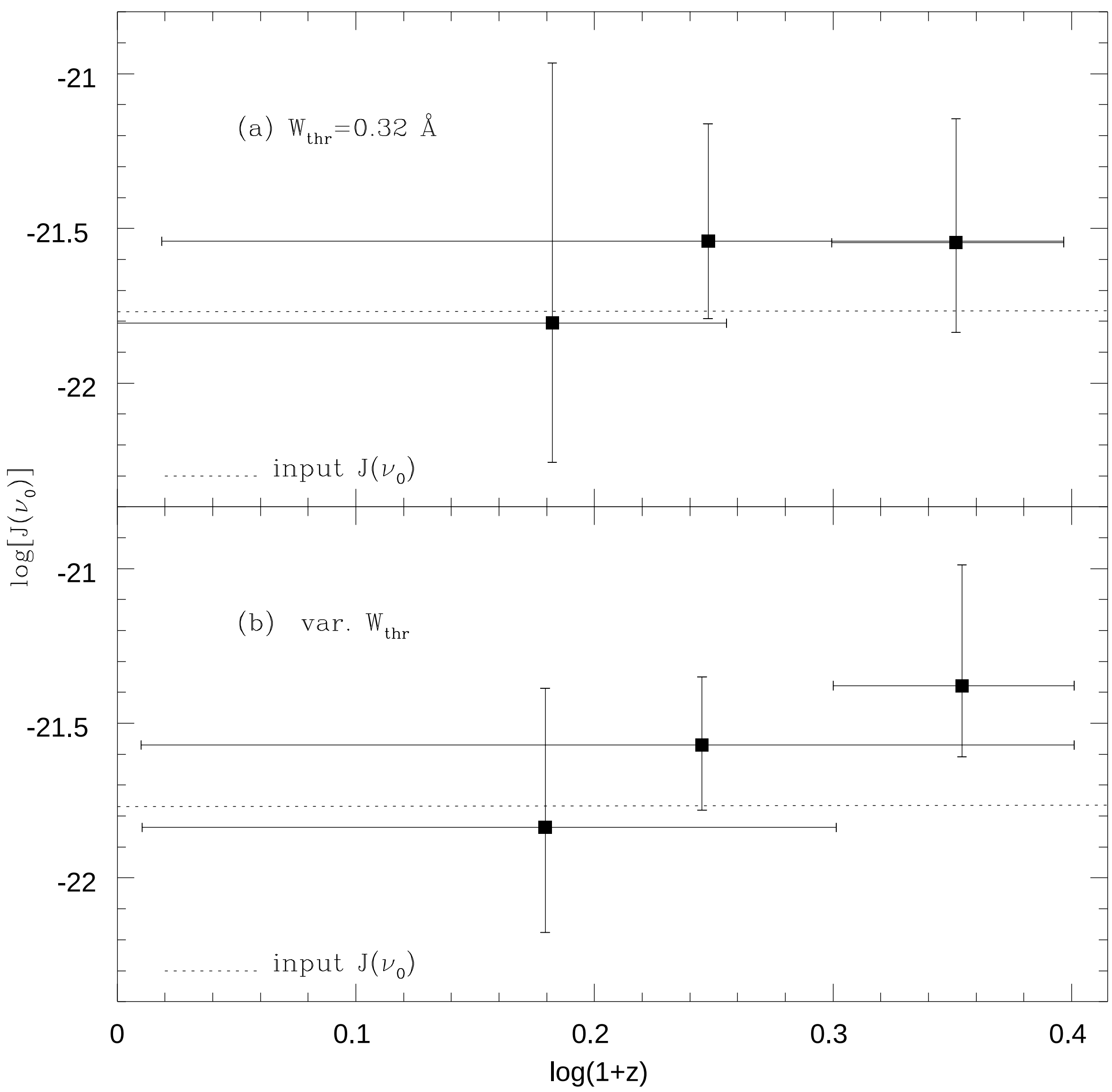

Fig. 12.— (a) Values of $\log[J(\nu_0)]$ recovered from simulated QSO spectra with proximity effect included: (dotted lines)- input $J(\nu_0, z)$, see Figure 11(a) (solid points)- recovered $J(\nu_0)$ for $W_{thr} = 0.32$ Å at all redshifts and at $z < 1$ and $z > 1$ separately; (b) same as (a), but $J(\nu_0)$ recovered using variable threshold

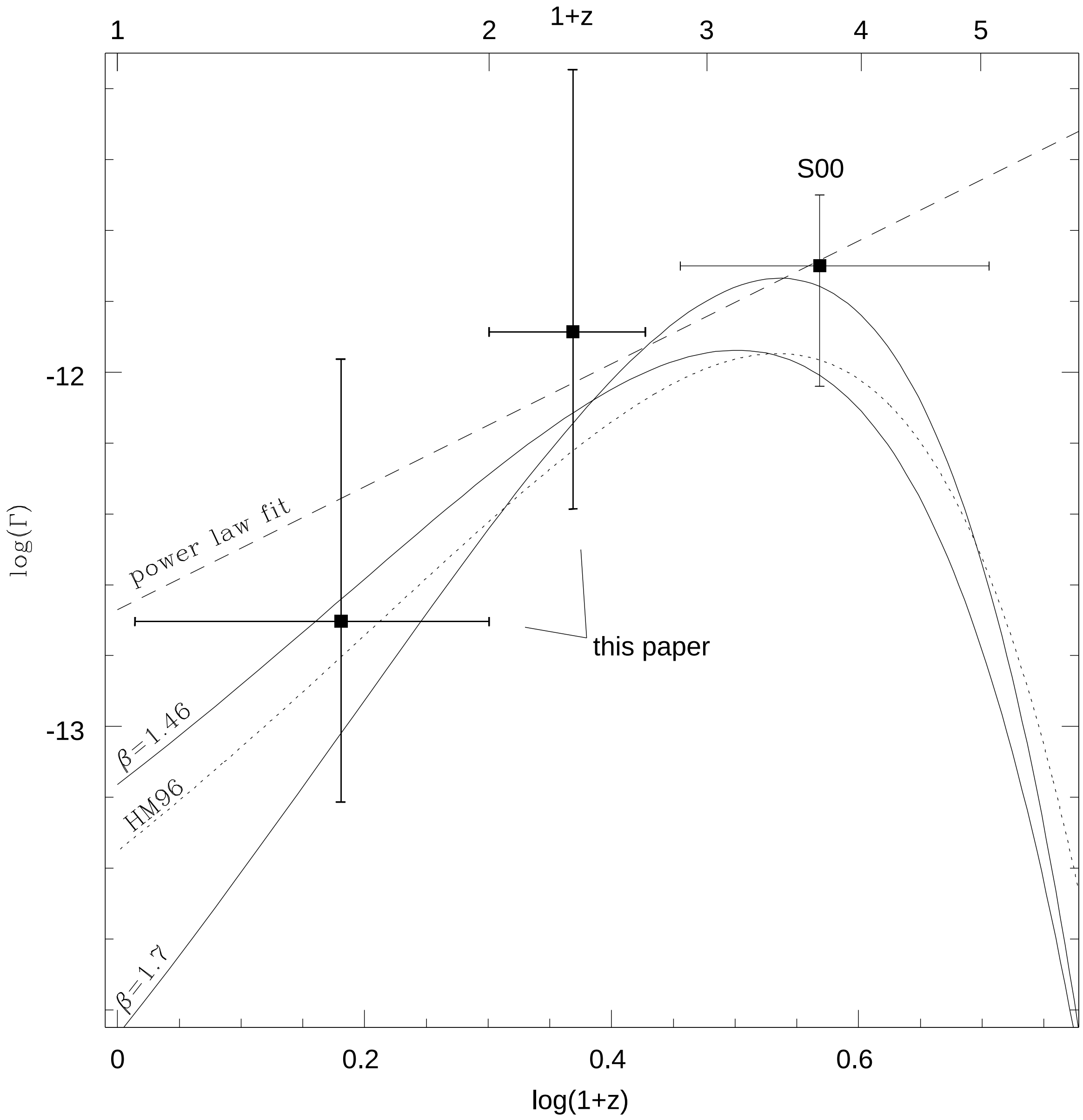

Fig. 13.— HI ionization rate versus redshift: (points)- constant equivalent width threshold maximum likelihood solutions from this paper, at $z < 1$ and $z > 1$, and from Paper II for $1.7 < z < 3.8$; (dashed line)- constant threshold solution to Equ. 13 for HST/FOS data alone; (solid line)- constant threshold solution to Equ. 14 with $\beta = 1.46$ and $\beta = 1.7$ for HST/FOS data and ground-based data from Papers I and II, (dotted line)- HM96 solution to Equ. 14

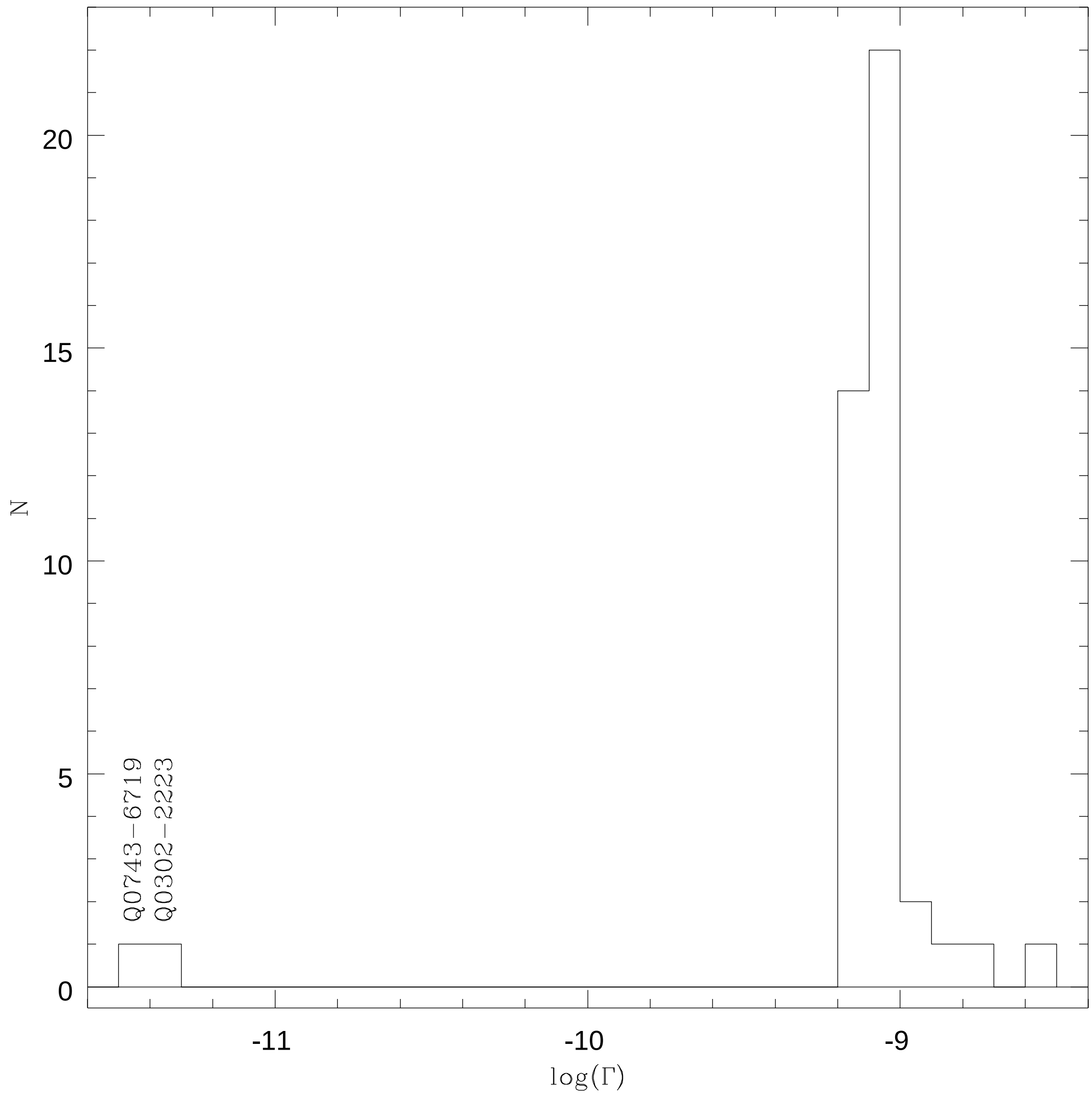

Fig. 14.— Histogram of results of jackknife measurements of HI ionization rate, Γ, for all lines at $z > 1$ above variable equivalent width threshold; labels on highest Γ bins indicate objects removed, see § 6.3

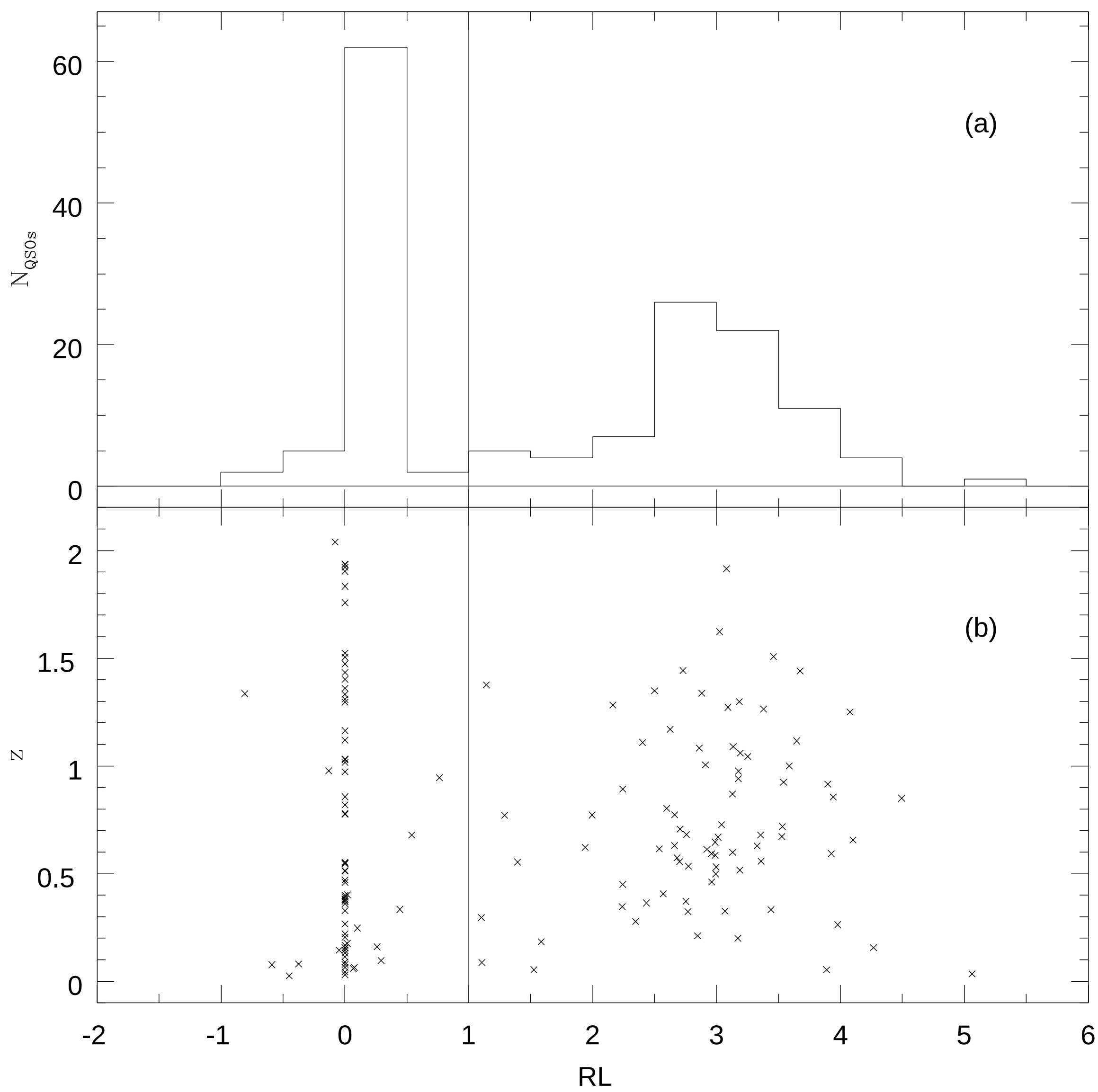

Fig. 15.— (a) Histogram of radio loudness (RL) values for QSOs in proximity effect sample, where RL = log[S(5 GHz)]/log[S(1450 Å)], includes blazars and objects with damped Ly-α absorption; (b) redshift versus RL for QSOs in proximity effect sample

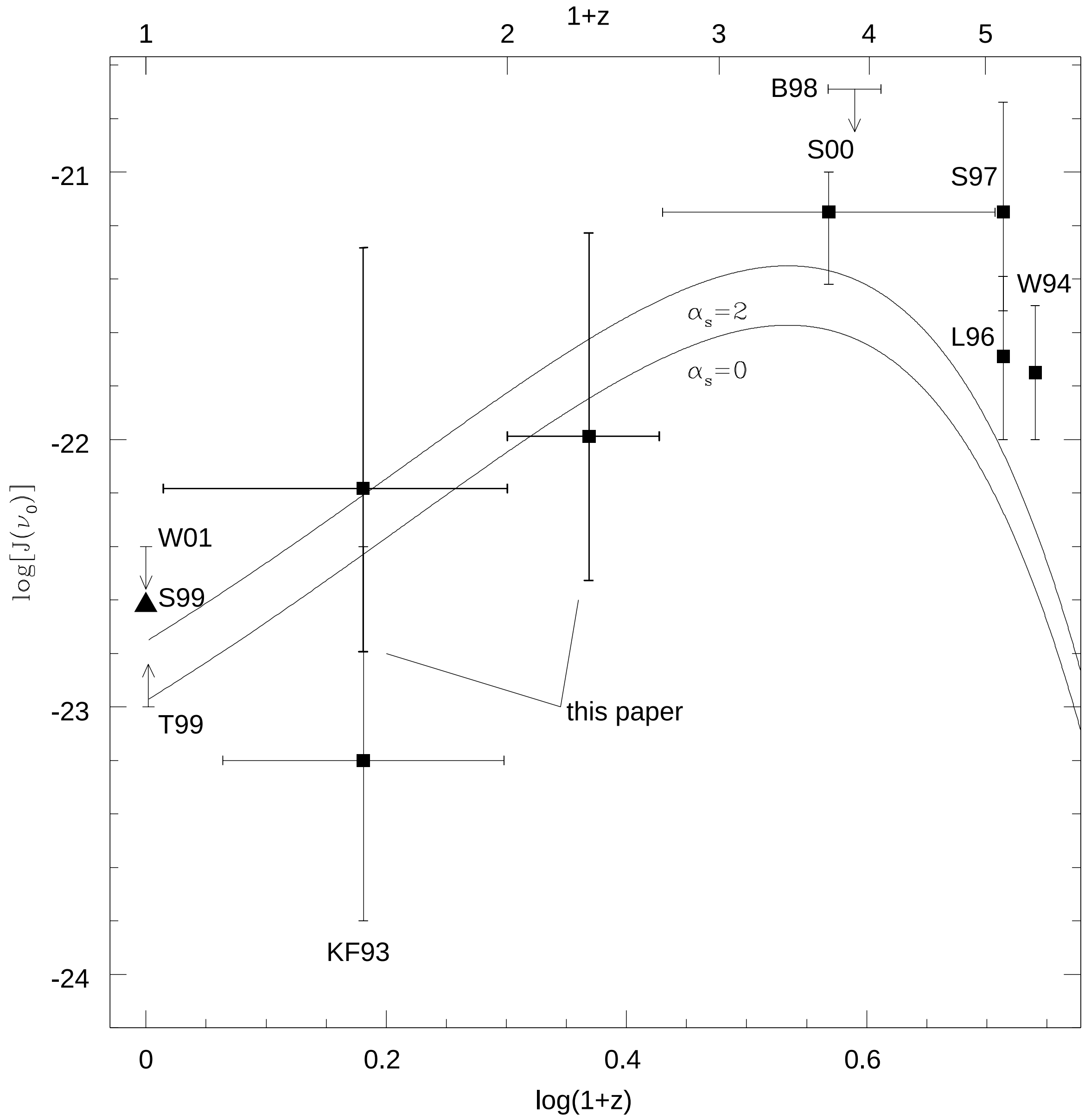

Fig. 16.— $\log[J(\nu_0)]$ versus redshift: (lower limit at $z \sim 0$)- Tumlinson et al. (1999); (upper limit at $z \sim 0$)- Weymann et al. (2001); (filled triangle)- Shull et al. (1999); (upper limit at $z = 0$)- Weymann et al. (2001); (filled squares, bold error bars)- our results for $z < 1$ and $z > 1$; (other filled squares)- results from KF93, Paper II, Lu et al. (1996), Savaglio et al. (1997), and Williger et al. (1994); (upper limit at $z \sim 3$)- Bunker et al. (1998); (solid curves)- HM96 models for two values of the global source spectral index, α_s

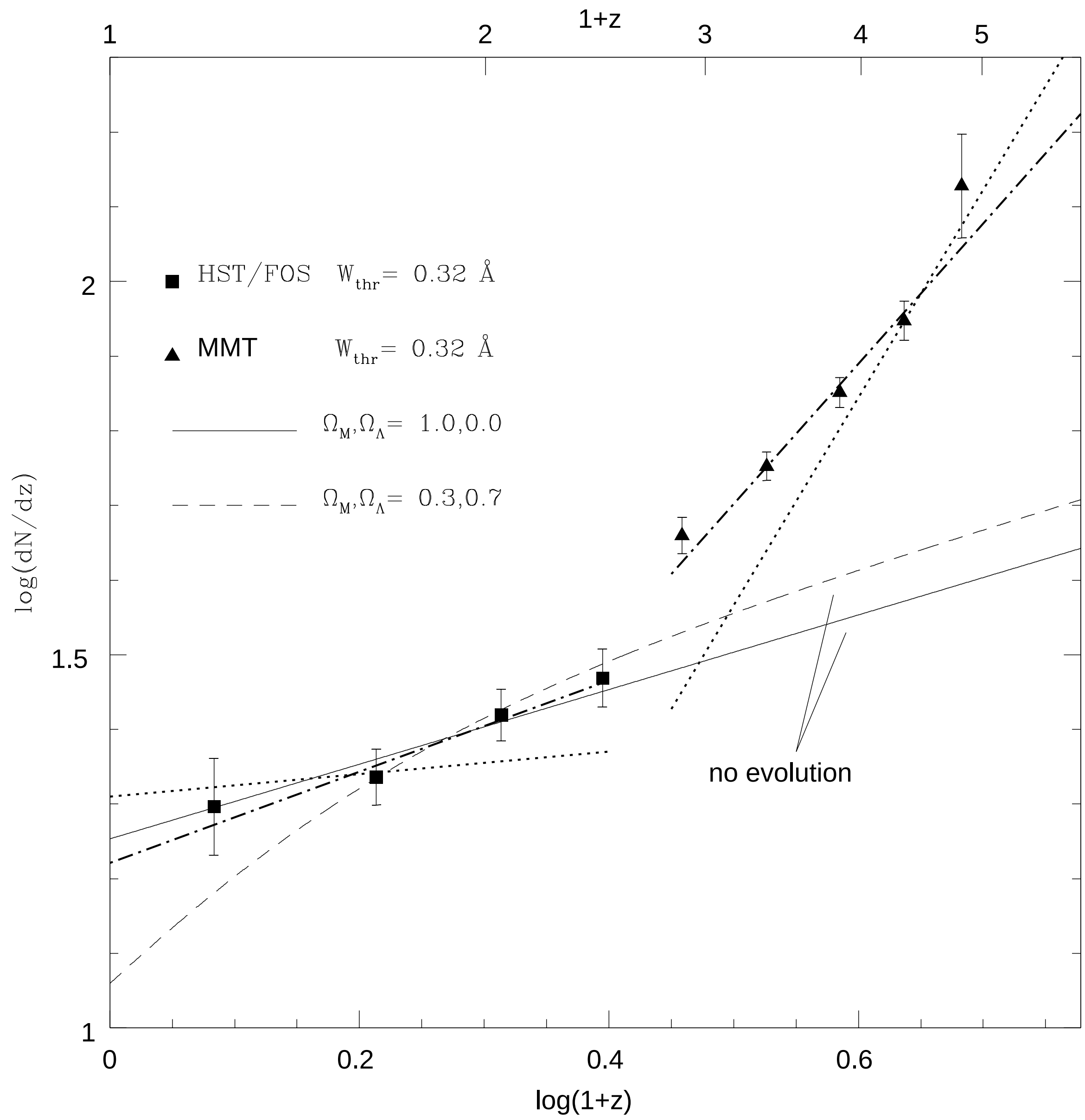

Fig. 17.— $d\mathcal{N}/dz$ versus z: solid and dashed lines show the relation for non-evolving Ly-α absorbers given by Equ. 18 for $(\Omega_M, \Omega_\Lambda) = (1.0, 0.0)$ and $(0.3, 0.7)$, respectively; dotted lines are fits to low redshift data from Weymann et al. (1998) and to high redshift data of Kim et al. (1997); dashed-dotted lines are fits to low redshift data from Paper IV and to high redshift data from Paper I

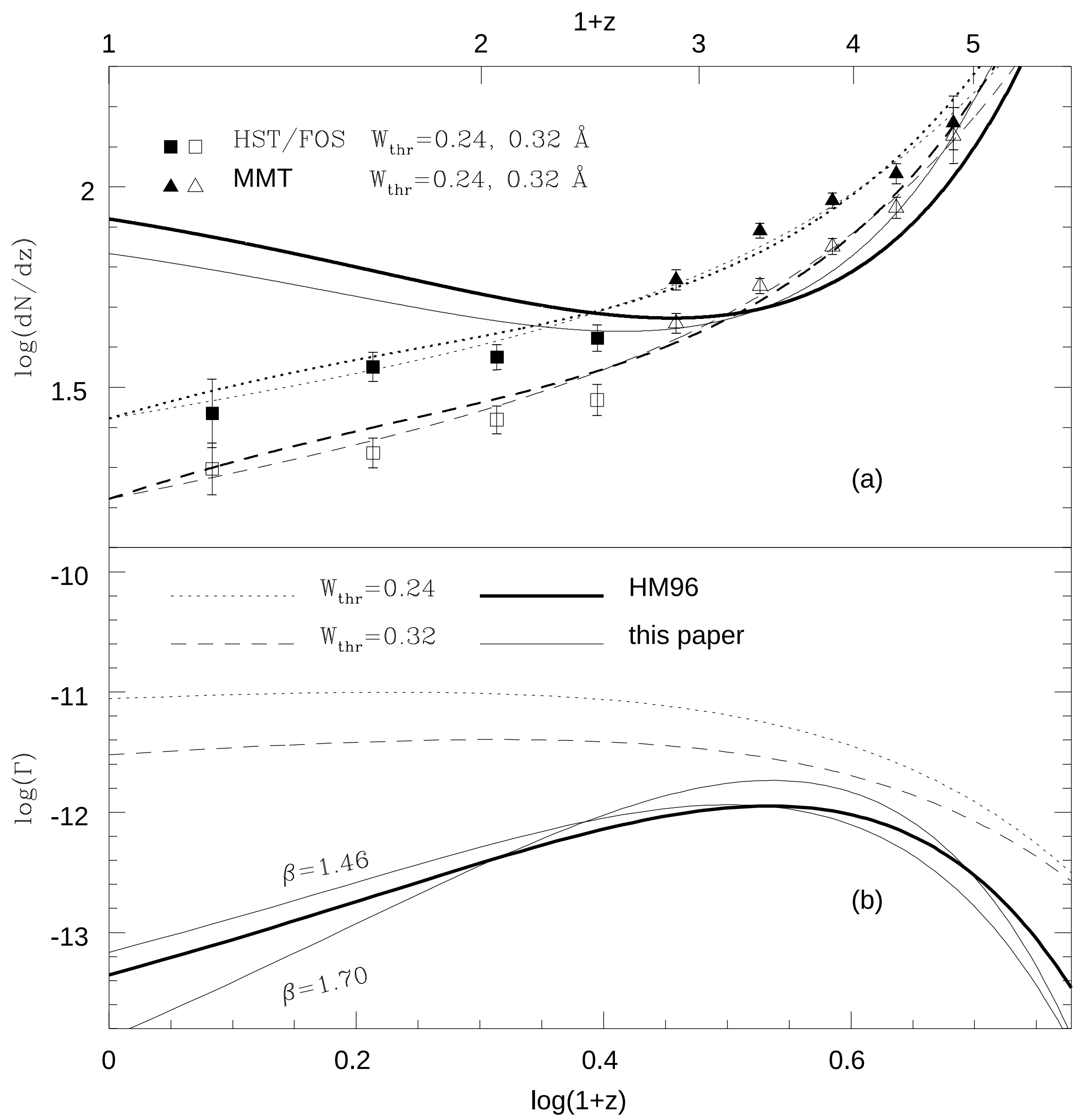

Fig. 18.— (a) $d\mathcal{N}/dz$ versus z: (solid points, dotted lines) $W_{thr} = 0.24$ Å with fit to Equ. 19, (open points, dashed lines) $W_{thr} = 0.32$ Å with fit to Equ. 19, (thick solid line) Equ. 19 evaluated with HM96 parameters for $\Gamma(z)$ expressed by Equ. 14, (thin solid lines) Equ. 19 evaluated with parameters for $\Gamma(z)$ found in this paper; (b) $\Gamma(z)$ versus redshift expressed by Equ. 14 using HM96 parameters (thick solid line), using parameters found in this paper (thin solid lines), and using parameters found from fits to $d\mathcal{N}/dz$ for $W_{thr} = 0.24$ Å and $(\Omega_M, \Omega_\Lambda) = (1.0, 0.0)$ (dotted line) and $W_{thr} = 0.32$ Å and $(\Omega_M, \Omega_\Lambda) = (1.0, 0.0)$ (dashed line),

Table 1. Sample QSOs and Emission Line Redshifts

QSO[1]	NED description	Ly-α	MgII	OIII	Balmer	References			
		(a)	(b)	(c)	(d)	(a)	(b)	(c)	(d)
0003+1553	opt.var.	0.4497	0.4502	0.4503	···	(1)	(2)	(3)	
0003+1955	opt.var.	0.0264	0.0264	0.0261	···	(1)	(1)	(4)	
0007+1041	opt.var.	0.0902	0.0890	0.089	0.0895	(1)	(1)	(5)	(6)
0015+1612	RQQ	0.5492	···	···	···	(1)			
0017+0209	LINER	0.3994	···	···	···	(1)			
0024+2225	···	1.1081	1.1096	···	···	(1)	(7)		
0026+1259	Sy1	0.1453	0.1463	0.1452	0.1458	(1)	(1)	(5)	(6)
0042+1010	···	0.5854	0.583	0.586	0.584	(1)	(8)	(8)	(8)
0043+0354	BAL?[2]	0.3803	···	···	···	(1)			
0044+0303	Sy1?	0.6219	0.6222	···	···	(1)	(2)		
0050+1225	Compact,Sy1	0.0594	···	···	···	(1)			
0100+0205	opt.var.	0.3937	···	0.3936	···	(1)		(3)	
0102-2713	···	0.7763	···	···	···	(1)			
0107-1537	···	0.8574	···	···	···	(1)			
0112-0142[3]	···	1.3739	1.3727	···	···	(1)	(1)		
0115+0242[3]	opt.var.	0.6652	0.6700	···	···	(1)	(9)		
0117+2118	···	1.4925	1.499	1.504	1.499	(1)	(10)	(11)	(11)
0121-5903	Sy1	0.0461	0.0462	0.044	···	(1)	(1)	(5)	
0122-0021	opt.var.,LPQ	1.0710	1.0895	···	···	(1)	(12)		
0137+0116	opt.var.	0.2622	···	0.2631	0.2644	(1)		(1)	(1)
0159-1147	opt.var.,Sy1	0.6683	0.6696	···	···	(1)	(13)		
0214+1050	opt.var.	0.4068	···	0.407	···	(1)		(14)	

Table 1—Continued

QSO[1]	NED description	Ly-α (a)	MgII (b)	OIII (c)	Balmer (d)	References (a)	(b)	(c)	(d)
0232-0415	opt.var.	1.4391	1.4434	···	···	(1)	(1)		
0253-0138[3]	···	0.8756	···	···	···	(1)			
0254-3327B	opt.var.	1.916	···	···	···	(15)			
0302-2223	DLAs	1.4021	···	···	···	(1)			
0333+3208	opt.var.,LPQ	1.2642	1.264	···	···	(1)	(7)		
0334-3617[3]	···	1.1085	···	···	···	(1)			
0349-1438	···	0.6155	0.615	···	0.6206	(1)	(16)		(1)
0355-4820	···	1.0058	1.005	···	···	(1)	(2)		
0403-1316[3]	opt.var.,HPQ	0.5705	···	0.571	···	(1)		(14)	
0405-1219	opt.var.,HPQ	0.5717	0.5730	0.573	0.5731	(1)	(16)	(14)	(16)
0414-0601	opt.var.	0.7739	0.773	0.774	···	(1)	(2)	(5)	
0420-0127	blazar,HPQ	0.9122	0.9162	···	···	(1)	(13)		
0439-4319	···	0.5932	···	···	···	(1)			
0454-2203	DLAs,LPQ	0.5327	0.5350	0.534	···	(1)	(2)	(14)	
0454+0356	DLAs	1.3413	1.3490	···	···	(1)	(10)		
0518-4549	Sy1	0.0355	0.0341	···	0.0339	(1)	(1)		(17)
0537-4406[3]	BL Lac,HPQ	0.8976	0.8926	···	···	(1)	(18)		
0624+6907	···	0.3663	0.3687	0.3710	0.3698	(1)	(1)	(1)	(1)
0637-7513	Sy1	0.6522	0.6565	···	0.6570	(1)	(18)		(18)
0710+1151[3]	opt.var.	0.7712	···	···	···	(1)			
0742+3150	Sy1	0.4589	0.462	0.461	0.4620	(1)	(19)	(14)	(10)
0743-6719	opt.var.	1.5109	1.5089	···	1.511	(1)	(20)		(21)

Table 1—Continued

QSO[1]	NED description	Ly-α (a)	MgII (b)	OIII (c)	Balmer (d)	References (a)	(b)	(c)	(d)
0827+2421	blazar,HPQ	0.9363	0.94	···	0.942	(1)	(7)		(7)
0844+3456	Sy1	0.0637	0.0646	0.064	···	(1)	(1)	(5)	
0848+1623	opt.var.	···	1.9220	···	···		(7)		
0850+4400	···	0.5132	0.5142	···	0.5150		(1)		(1)
0859-1403[3]	blazar	1.3338	1.3381	···	1.341	(1)	(13)		(21)
0903+1658[3]	opt.var.	0.4108	0.4106	0.4114	···	(1)	(22)	(22)	
0907-0920[3]	···	0.630[4]	···	···	···				
0916+5118	···	0.5520	0.5525	···	0.5536		(1)		(1)
0923+3915[3]	opt.var.,Sy1,LPQ	0.6986	0.6990	···	···	(1)	(24)		
0935+4141	···	1.937[4]	···	···	···				
0945+4053	LPQ	1.2479	1.2506	···	···	(1)	(19)		
0947+3940	Sy1	0.2057	···	0.2059	···	(1)		(25)	
0953+4129	Sy1?	0.2331	···	0.247	0.2326	(1)		(25)	(25)
0954+5537[3]	blazar,HPQ	0.9005	0.9025	···	···	(1)	(1)		
0955+3238	opt.var.,Sy1.8	0.5281	···	0.531	0.5309			(14)	(10)
0958+5509	···	1.7569	1.7582	···	···	(10)	(7)		
0959+6827	···	0.7663	0.7724	···	···	(1)	(1)		
1001+0527	···	0.1589	0.1605	···	0.160	(1)	(1)		(25)
1001+2239	···	0.9766	···	···	···	(1)			
1001+2910	AGN	0.3285	···	···	0.3293	(1)			(1)
1007+4147	···	0.6110	0.6125	···	···	(1)	(13)		
1008+1319	···	1.3012	1.2968	···	···	(1)	(1)		

Table 1—Continued

QSO[1]	NED description	Ly-α (a)	MgII (b)	OIII (c)	Balmer (d)	References (a)	(b)	(c)	(d)
1010+3606	Sy1	0.0785	···	0.079	···	(1)		(5)	
1026-004A	···	1.4349	···	···	···	(1)			
1026-004B	···	1.5253	···	···	···	(1)			
1038+0625	opt.var.,LPQ	1.2667	1.272	···	···	(1)	(7)		
1049-0035	Sy1	0.3580	0.360	···	0.3605	(1)	(5)		(10)
1055+2007	opt.var.	1.1136	1.1165	···	···	(1)	(13)		
1100+7715	opt.var.,AGN	0.3120	···	0.324	0.339	(1)		(25)	(25)
1104+1644	opt.var.,Sy1	0.6294	···	0.630	0.6307	(1)		(5)	(6)
1114+4429	Sy1	0.1448	0.1442	0.143	···	(1)	(1)	(25)	
1115+4042	Sy1	0.1545	0.1552	···	0.156	(1)	(1)		(25)
1116+2135	E2,Sy1?	···	···	0.1768	0.1756			(25)	(25)
1118+1252	opt.var.	0.6823	···	···	···	(1)			
1127-1432[3]	blazar,LPQ	1.1824	1.2121	···	···	(1)	(18)		
1130+1108	···	0.5065	···	0.5110	0.5104	(1)		(1)	(1)
1136-1334	Sy1	0.5551	0.5571	···	0.5604	(1)	(18)		(18)
1137+6604	opt.var.,LPQ	0.6449	0.6448	0.646	···	(1)	(13)	(5)	
1138+0204	···	0.3789	···	0.3820	0.3831	(1)		(1)	(1)
1148+5454	opt.var.	0.9688	0.9777	···	···	(1)	(10)		
1150+4947	opt.var.	0.3334	0.333	0.333	0.333	(1)	(26)	(26)	(26)
1156+2123	···	0.3464	···	0.3475	0.3459	(1)		(1)	(1)
1156+2931	blazar,HPQ	0.7225	0.7281	···	···	(1)	(1)		
1206+4557	···	1.1596	1.164	···	···	(1)	(7)		

Table 1—Continued

QSO[1]	NED description	Ly-α (a)	MgII (b)	OIII (c)	Balmer (d)	References (a)	(b)	(c)	(d)
1211+1419	RQQ,Sy1	0.0802	0.0805	0.0807	0.0810	(1)	(1)	(25)	(25)
1214+1804	···	0.3719	···	···	0.3726	(1)			(1)
1215+6423	···	1.2981	···	···	···	(1)			
1216+0655	opt.var.	0.3312	0.3302	0.334	0.3374	(1)	(25)	(5)	(25)
1219+0447	AGN	0.0953	0.0931	···	···	(1)	(1)		
1219+7535[3]	SB(r)ab pec,Sy1	0.0701	0.0713	0.071	···	(1)	(1)	(5)	
1226+0219	blazar,Sy1,LPQ	0.156	···	0.157	0.158	(1)		(27)	(27)
1229-0207	DLAs,blazar,LPQ	1.0406	1.0439	···	···	(1)	(13)		
1230+0947[3]	···	0.4176	···	0.4162	0.4153	(1)		(1)	(1)
1241+1737	···	1.2807	1.282	···	···	(1)	(7)		
1247+2647	AGN	2.0394	···	···	···	(10)			
1248+3032	···	1.0607	···	···	···	(1)			
1248+3142	···	···	1.029	···	···		(28)		
1248+4007	···	1.0256	1.033	···	···	(1)	(7)		
1249+2929	···	0.8205	···	···	···	(1)			
1250+3122	···	0.7779	···	···	···	(1)			
1252+1157	opt.var.	0.8701	···	···	···	(1)			
1253-0531	BL Lac,HPQ	0.5367	0.5366	0.5356	0.536	(1)	(29)	(29)	(29)
1257+3439	opt.var.	1.3760	1.376	···	···	(1)	(7)		
1258+2835	···	1.3611	···	···	···	(1)			
1259+5918	···	0.4679	0.4717	···	0.4853	(1)	(25)		(25)
1302-1017	E4?,opt.var.	0.2770	0.2867	0.278	0.2868	(1)	(12)	(5)	(6)

Table 1—Continued

QSO[1]	NED description	Ly-α (a)	MgII (b)	OIII (c)	Balmer (d)	References (a)	(b)	(c)	(d)
1305+0658	···	0.6009	0.5999	···	···	(1)	(1)		
1309+3531	Sab,Sy1	0.1841	···	0.184	0.183	(1)		(25)	(25)
1317+2743	···	1.0082	1.016	···	···	(1)	(7)		
1317+5203[3]	blazar	1.0550	1.0555	···	···	(1)	(7)		
1318+2903	opt.var.	0.5469	···	···	···	(1)			
1320+2925	···	0.9601	0.972	···	···	(1)	(7)		
1322+6557	Sy1	0.1676	···	···	0.1684	(1)			(25)
1323+6530	···	1.6227	1.6233	···	···	(1)	(30)		
1327-2040	···	1.1682	1.170	···	···	(1)	(18)		
1328+3045	DLAs	0.8466	0.8508	···	···	(1)	(13)		
1329+4117	···	1.9351	···	···	···	(10)			
1333+1740	···	0.5464	0.5546	···	···	(1)	(25)		
1351+3153	···	1.3170	1.3382	···	···	(1)	(31)		
1351+6400	Sy1	0.0886	0.0884	0.087	0.089	(1)	(1)	(25)	(25)
1352+0106	···	1.1200	···	···	···	(1)			
1352+1819	Sy1	0.1508	0.1514	0.1572	0.1538	(1)	(1)	(25)	(25)
1354+1933	opt.var.	0.7190	0.718	0.719	···	(1)	(7)	(5)	
1356+5806[3]	···	1.3741	1.370	···	···	(1)	(7)		
1401+0952[3]	···	0.4363	···	···	···	(1)			
1404+2238	Sy	0.0966	0.0978	···	0.098	(1)	(1)		(25)
1407+2632	···	0.95	0.946	···	0.958	(1)	(32)		(32)
1415+4509	···	0.1145	0.1142	0.1143	0.1139	(1)	(1)	(25)	(25)

Table 1—Continued

QSO[1]	NED description	Ly-α (a)	MgII (b)	OIII (c)	Balmer (d)	References (a)	(b)	(c)	(d)
1416+0642	···	1.4339	···	···	1.442	(1)			(21)
1424-1150	···	0.8033	0.8037	···	···	(1)	(18)		
1425+2645	opt.var.	0.3634	···	···	0.3644	(1)			(10)
1427+4800	Sy1	0.2215	···	0.2203	0.2246	(1)		(25)	(25)
1435-0134	···	1.3099	···	···	···	(1)			
1440+3539	compact	0.0764	0.0772	0.0777	0.0772	(1)	(1)	(25)	(25)
1444+4047	E1?	0.2659	···	0.2672	0.267	(1)		(3)	(5)
1512+3701	Sy1?	0.3704	0.3734	0.371	0.3715	(1)	(2)	(5)	(6)
1517+2356	···	1.9037	···	···	···	(10)			
1517+2357	···	1.834[4]	···	···	···				
1521+1009	···	1.3210	1.332	···	···	(1)	(7)		
1538+4745	···	0.7704	0.7711	···	···	(1)	(7)		
1544+4855	···	0.3985	···	···	0.4010	(1)			(2)
1555+3313[3]	···	0.9402	0.9427	···	···	(1)	(31)		
1611+3420[3]	blazar,LPQ	1.3968	1.3997	···	···	(1)	(33)		
1618+1743	opt.var.	0.5549	0.5560	0.555	···	(1)	(14)	(13)	
1622+2352	opt.var.	0.9258	0.925	···	···	(1)	(7)		
1626+5529	Sy1	0.1315	0.1325	0.132	0.133	(1)	(1)	(25)	(25)
1630+3744	···	1.4712	1.478	1.474	1.478	(1)	(10)	(11)	(27)
1634+7037	···	1.3338	1.338	1.336	1.342	(1)	(10)	(11)	(27)
1637+5726[3]	LPQ	0.7499	0.750	···	0.751	(1)	(7)		(5)
1641+3954[3]	opt.var.,HPQ[5]	0.5946	0.5954	0.593	···	(1)	(14)	(2)	

Table 1—Continued

QSO[1]	NED description	Ly-α (a)	MgII (b)	OIII (c)	Balmer (d)	References (a)	(b)	(c)	(d)
1704+6048	opt.var.	0.3694	0.3704	0.372	···	(1)	(2)	(5)	
1715+5331	···	1.9371	1.932	···	···	(10)	(7)		
1718+4807	···	1.0809	1.0828	···	···	(1)	(7)		
1803+7827	BL Lac	0.6840	···	0.6797	···	(1)			(23)
1821+6419	Sy1	0.2957	···	0.297	···	(1)		(5)	
1845+7943	opt.var.,BLRG,Sy1	0.0567	0.0548	···	···	(1)	(1)		
2112+0556	···	0.4585	···	···	0.460	(1)			(5)
2128-1220	opt.var.,LPQ,Sy1	0.4988	0.5000	0.499	0.5028	(1)	(2)	(14)	(6)
2135-1446	E1,opt.var.,Sy1	0.2016	···	0.200	0.199	(1)		(14)	(34)
2141+1730	opt.var.,LPQ,Sy1	0.2124	···	0.211	···	(1)		(14)	
2145+0643	opt.var.,LPQ	0.9997	1.000	···	···	(1)	(7)		
2155-3027[3]	opt.var.,BL Lac	0.116[4]	···	···	···				
2201+3131[3]	LPQ	0.2953	0.2981	0.295	0.2979	(1)	(16)	(5)	(16)
2216-0350[3]	opt.var.,LPQ	0.8997	0.900	···	···	(1)	(7)		
2223-0512[3]	opt.var.,HPQ,BL Lac	1.4037	···	···	···	(1)			
2230+1128[3]	blazar,HPQ	1.0367	1.0379	···	···	(1)	(13)		
2243-1222	opt.var.,HPQ	0.6257	0.6297	···	···	(1)	(17)		
2251+1120	opt.var.	···	0.322	0.326	0.3255		(34)	(5)	(10)
2251+1552	blazar,HPQ	0.8557	···	···	···	(1)			
2251-1750	opt.var.,Sy1	0.0651	0.0637	0.064	···	(1)	(1)	(5)	
2300-6823	···	0.5149	0.511	0.516	0.512	(1)	(35)	(35)	(35)
2340-0339	···	0.8948	0.893	···	···	(1)	(7)		

Table 1—Continued

QSO[1]	NED description	Ly-α (a)	MgII (b)	OIII (c)	Balmer (d)	References (a)	(b)	(c)	(d)
2344+0914	opt.var.,Sy1	0.6710	0.6722	0.673	0.6731	(1)	(16)	(5)	(16)
2352-3414	opt.var.	0.7060	0.7063	···	···	(1)	(2)		

[1]See Paper III, Table 1 for alternate names

[2]We classify this as an associated absorber, see Paper III

[3]Observed only with pre-COSTAR FOS and A-1 aperture

[4]Redshift from Green et al. 1986 (0935+4141), Hewitt & Burbidge 1987 (1517+2357), Knezek & Bregman 1998 (0907-0920), Falomo et al. 1993 (2155-3027)

[5]Classified as blazar by Kinney et al. 1991

References. — (1)This paper; (2)Tytler et al. 1987; (3)Stockton & MacKenty 1987; (4)de Robertis 1985; (5)Corbin & Boroson 1996; (6)Zheng & Sulentic 1990; (7)Steidel & Sargent 1991; (8)Smith et al. 1977; (9)Cristiani & Koehler 1987; (10)Tytler & Fan 1992; (11)Nishihara et al. 1997; (12)Browne et al. 1975; (13)Aldcroft et al. 1994; (14)Corbin 1997; (15)Bolton et al. 1976; (16)Gaskell 1982; (17)Basu 1994; (18)Wilkes 1986; (19)Wills & Wills 1976; (20)di Serego-Alighieri et al. 1994; (21)Cheng et al. 1990; (22)Lynds et al. 1966; (23)Lawrence et al. 1996; (24)Burbidge & Kinman 1966; (25)Green et al. 1986; (26)Lynds & Wills 1968; (27)Morris & Ward 1988; (28)Zotov 1985; (29)Netzer et al. 1994; (30)Barthel et al. 1990; (31)Ulrich 1976; (32)M^{c}Dowell et al. 1995; (33)Schmidt 1977; (34)Kinman & Burbidge 1967; (35)Jauncey et al. 1978

Table 2. Summary of Observations

Name	V	Setup[a]	Date	Total exposure time (sec)
0112-0142	18.0	1	13Dec1996	1200
0137+0116	17.1	1	13Dec1996	1200
0232-0415	16.4	1	13Dec1996	1200
0349-1438	16.2	1	12Dec1996	900
0414-0601	15.9	1	19Dec1995	400
0454-2203	16.1	1	19Dec1995	400
0624+6907	14.2	1	19Dec1995	465
0827+2421	17.2	3	15Feb1997	1200
0850+4400	16.4	1	19Dec1995	300
0859-1403	16.6	2a	12Dec1996	3600
0916+5118	16.5	1	19Dec1995	350
0923+3915	17.9	2b	14Jan1996	1800
0954+5537	17.7	2c	20Apr1996	3600
0959+6827	16.4	2b	14Jan1996	1800
1001+2910	15.5	2a	12Dec1996	3600
1008+1319	16.2	2a	10Dec1996	1800
1130+1108	16.9	2d	14Jan1996	3600
1138+0204	17.6	2e	12Dec1996	2400
1156+2123	17.5	2e	12Dec1996	1800
1156+2931	17.0	2a	10Dec1996	1800
1214+1804	17.5	2f	21Apr1996	1800
1230+0947	16.1	2f	21Apr1996	3600
1305+0658	17.0	2c	20Apr1996	3600

[a]Telescope/Instrument set up: (1) FLWO 1.5 m, FAST, 300 l mm^{-1} 1st order, 3 $''$ slit, 3660-7540 Å; (2) SO B90, B&C, 600 l mm^{-1} 1st order, 1.5 $''$ slit, [a] 4500-6700 Å, [b] 3600-5825 Å, [c] 4140-6370 Å, [d] 6870-9140 Å, [e] 5610-7860 Å, [f] 5280-7550 Å; (3) MMT, Blue Channel, 800 l mm^{-1} 1st order, 2$''$ slit, 4365-6665 Å

Table 3. Spectrophotometric Properties

QSO	N_{HI} (a)	$f_{\nu_0}^{obs}$ (b)	α (c)	f_{ν_0} (d)	f_{ν}^{obs} (e)	RL (f)	References (b)	(c)	(d)	(e)
0003+1553	3.88	0.46	0.71±0.52	1.39±0.33	1.94 (1450)	2.24	(2)	(1b)	(1b)	(1b)
0003+1955	3.99	2.04	0.47±0.09	6.77±0.45	8.43 (1450)	-0.44	(3)	(1a)	(1a)	(1a)
0007+1041	5.62		-0.50±1.00	1.86±0.66	1.47 (1450)	0.00		(1a)	(1a)	(1a)
0015+1612	4.07		-1.14±0.43	0.19±0.06	0.11 (1450)	0.00		(1b)	(1b)	(1b)
0017+0209	3.05		1.98±0.56	0.12±0.08	0.31 (1450)	0.00		(1b)	(1b)	(1b)
0024+2225[1]	3.60		0.59±0.65	0.60±0.15	0.79 (1450)	2.40		(1c)	(1c)	(1c)
0026+1259	4.56		-0.10±0.24	2.33±0.33	2.22 (1450)	-0.04		(1b)	(1b)	(1b)
0042+1010	5.52		0.19±0.08	0.08±0.02	0.09 (1450)	2.99		(1c)	(1c)	(1c)
0043+0354[1]	3.18		2.35±0.04	0.13±0.01	0.97 (2093)	0.00		(1c)	(1c)	(1c)
0044+0303	2.88	1.16	0.34±0.11	0.67±0.07	0.79 (1450)	1.94	(2)	(1c)	(1c)	(1c)
0050+1225[1]	1.46		0.84±1.14	1.72±1.05	2.56 (1450)	0.06		(1a)	(1a)	(1a)
0100+0205	2.92		1.42±0.27	0.23±0.06	0.45 (1450)	0.00		(1b)	(1b)	(1b)
0102-2713	1.93		···	0.18	0.29 (1285)	0.00		(4)		(1b)
0107-1537	1.73		0.78±0.31	0.11±0.01	0.16 (1450)	0.00		(1c)	(1c)	(1c)
0112-0142[2]	4.32		···	0.17	0.29 (1326)	3.83		(4)		(1c)
0115+0242[2]	3.32		0.83±0.08	0.05±0.01	0.08 (1450)	4.08		(1c)	(1c)	(1c)
0117+2118[1]	4.75	0.39	0.15±40.6	1.77±7.84	1.88 (1307)	0.00	(2)	(1c)	(1c)	(1c)
0121-5903	3.05		0.15±0.10	2.71±0.27	2.91 (1450)	0.00		(1a)	(1a)	(1a)
0122-0021	3.57		0.65±0.07	0.63±0.07	0.86 (1450)	3.13		(1c)	(1c)	(1c)
0137+0116	3.00		1.44±0.31	0.03±0.02	0.07 (1450)	3.97		(1b)	(1b)	(1b)
0159-1147	1.77		-0.02±0.11	1.35±0.05	1.33 (1450)	3.01		(1c)	(1c)	(1c)
0214+1050	6.96		1.39±0.08	0.64±0.13	1.22 (1450)	2.57		(1b)	(1b)	(1b)
0232-0415	2.42	0.59	···	···	···	2.73	(2)			
0253-0138[2]	5.61		0.31±0.19	0.67±0.07	0.78 (1450)	0.00		(1c)	(1c)	(1c)
0254-3327B[4]	2.32		···	0.28	···	3.08		(4)		
0302-2223[1,4]	1.87	0.31	-2.89±0.08	2.57±0.44	0.88 (1318)	0.00	(2)	(1c)	(1c)	(1c)
0333+3208	13.5		0.80±5.79	0.56±1.65	0.81 (1450)	3.38		(1c)	(1c)	(1c)
0334-3617[2]	1.40		0.13±1.27	0.13±0.02	0.14 (1450)	···		(1c)	(1c)	(1c)
0349-1438	3.83		-0.32±0.29	2.45±0.23	2.11 (1450)	2.53		(1c)	(1c)	(1c)
0355-4820[1]	1.16	0.39	0.65±0.58	0.52±0.13	0.70 (1450)	2.91	(5)	(1c)	(1c)	(1c)

Table 3—Continued

QSO	N_{HI}	$f_{\nu_0}^{obs}$	α	f_{ν_0}	f_ν^{obs}	RL	References			
	(a)	(b)	(c)	(d)	(e)	(f)	(b)	(c)	(d)	(e)
0403-1316[2]	3.65		0.23±0.04	0.35±0.05	0.39 (1450)	4.35		(1c)	(1c)	(1c)
0405-1219	3.74	2.05	-0.11±0.04	4.38±0.18	4.14 (1450)	2.68	(2)	(1c)	(1c)	(1c)
0414-0601	5.14	0.34	-0.19±0.08	0.77±0.05	0.70 (1450)	2.66	(2)	(1c)	(1c)	(1c)
0420-0127[3]	7.10		1.84±0.05	0.08±0.01	0.20 (1450)	3.89		(1c)	(1c)	(1c)
0439-4319	2.30		0.40±0.08	0.27±0.01	0.33 (1450)	2.95		(1c)	(1c)	(1c)
0454+0356[5]	7.39	0.38	-0.26±2.26	1.40±0.57	1.26 (1336)	2.50	(2)	(1c)	(1c)	(1c)
0454-2203	2.99	0.38	0.05±4.19	1.25±0.17	1.28 (1450)	2.77		(1b)	(1b)	(1b)
0518-4549	4.12		0.18±1.45	0.12±0.05	0.13 (1450)	5.06		(1a)	(1a)	(1a)
0537-4406[2]	4.02	0.05	2.00±0.16	0.14±0.03	0.36 (1450)	4.05	(2)	(1c)	(1c)	(1c)
0624+6907	7.01		1.71±0.03	2.37±0.18	5.26 (1450)	0.00		(1b)	(1b)	(1b)
0637-7513	9.22	0.53	1.32±0.07	0.27±0.03	0.49 (1450)	4.10	(2)	(1c)	(1c)	(1c)
0710+1151[2]	11.0		0.16±0.08	1.13±0.10	1.22 (1450)	4.12		(1c)	(1c)	(1c)
0742+3150[1]	4.89	0.35	0.24±0.43	0.92±0.08	1.03 (1450)	2.96	(2)	(1b)	(1b)	(1b)
0743-6719	11.9	0.24	···	···	···	3.46	(2)			
0827+2421[3]	3.51		1.21±0.04	0.34±0.03	0.59 (1450)	3.17		(1c)	(1c)	(1c)
0844+3456[1]	3.31		0.75±0.03	2.31±0.09	4.94 (2495)	0.00		(1c)	(1c)	(1c)
0848+1623[4]	29.7		0.46	0.15	0.19 (1450)	0.00		(6)		(11)
0850+4400	2.53		1.02±0.20	0.35±0.05	0.56 (1450)	0.00		(1b)	(1b)	(1b)
0859-1403[2]	5.71	0.60	···	···	···	3.29	(2)			
0903+1658[2]	3.61		3.28±0.27	0.03±0.02	0.17 (1450)	2.79		(1b)	(1b)	(1b)
0907-0920[6]	4.57		-0.04±1.50	0.11±0.008	0.11 (1822)	0.00		(1c)	(1c)	(1c)
0916+5118	1.40		0.31±0.03	0.71±0.06	0.82 (1450)	0.00		(1c)	(1c)	(1c)
0923+3915[2]	1.53		0.17±0.05	0.70±0.03	0.77 (1450)	4.83		(1c)	(1c)	(1c)
0935+4141[4,5]	1.32		···	0.55	···	0.00		(4)		
0945+4053	1.44		-0.33±5.03	0.17±0.19	0.15 (1450)	4.07		(1c)	(1c)	(1c)
0947+3940	1.61		0.70±0.11	0.90±0.08	1.25 (1450)	0.00		(1b)	(1b)	(1b)
0953+4129	1.28		0.71±0.08	1.13±0.10	1.58 (1450)	0.10		(1b)	(1b)	(1b)
0954+5537[2]	0.94		0.96±0.05	0.12±0.01	0.18 (1450)	3.51		(1c)	(1c)	(1c)
0955+3238[1]	1.62	0.38	0.96±0.07	0.45±0.03	0.87 (1774)	2.99	(2)	(1c)	(1c)	(1c)
0958+5509[1]	0.84	0.31	···	···	···	0.00	(2)			

Table 3—Continued

QSO	N_{HI}	$f_{\nu_0}^{obs}$	α	f_{ν_0}	f_{ν}^{obs}	RL	References			
	(a)	(b)	(c)	(d)	(e)	(f)	(b)	(c)	(d)	(e)
0959+6827	3.93		1.12±2.21	0.54±0.71	1.10 (1720)	1.99		(1c)	(1c)	(1c)
1001+0527[1]	2.41		1.73±0.12	0.24±0.04	0.55 (1450)	0.26		(1b)	(1b)	(1b)
1001+2239	2.82		1.67±0.32	0.05±0.02	0.12 (1450)	3.17		(1c)	(1c)	(1c)
1001+2910	1.93		1.18±0.02	1.08±0.06	1.88 (1450)	0.00		(1b)	(1b)	(1b)
1007+4147	1.23	0.72	-0.20±0.08	1.12±0.07	1.02 (1450)	2.92	(2)	(1c)	(1c)	(1c)
1008+1319[1]	3.79	0.58	···	···	···	0.00	(2)			
1010+3606	1.24		0.90±1.60	0.66±0.60	1.00 (1450)	0.00		(1a)	(1a)	(1a)
1026-004A	4.85		···	0.11	0.19 (1328)	0.00		(4)		(1c)
1026-004B	4.85		···	0.15	0.24 (1285)	0.00		(4)		(1c)
1038+0625[1]	2.81		-0.65±1.96	1.30±0.06	1.00 (1361)	3.09		(1c)	(1c)	(1c)
1049-0035[1]	3.87	0.35	1.60±0.11	0.51±0.07	1.07 (1450)	0.00	(2)	(1b)	(1b)	(1b)
1055+2007	1.94		0.51±0.37	0.27±0.05	0.34 (1450)	3.64		(1c)	(1c)	(1c)
1100+7715[1]	3.04		0.67±0.04	0.97±0.06	1.33 (1450)	2.76		(1b)	(1b)	(1b)
1104+1644	1.55		-0.02±0.15	1.23±0.08	1.22 (1450)	2.66		(1c)	(1c)	(1c)
1114+4429[1]	1.80		1.80±0.04	0.15±0.02	0.35 (1450)	0.00		(1b)	(1b)	(1b)
1115+4042[1]	1.86		0.44±0.05	1.10±0.14	1.35 (1450)	0.00		(1b)	(1b)	(1b)
1116+2135	1.27		0.46±0.10	2.31±0.36	2.87 (1450)	0.01		(1b)	(1b)	(1b)
1118+1252[1]	2.28		0.42±0.08	0.11±0.02	0.14 (1450)	2.75		(1c)	(1c)	(1c)
1127-1432[2]	4.07		0.96±3.07	0.31±0.59	0.49 (1450)	4.78		(1c)	(1c)	(1c)
1130+1108[1]	3.47		1.40±0.15	0.32±0.05	0.62 (1450)	0.00		(1b)	(1b)	(1b)
1136-1334	3.51	0.60	-0.46±0.20	1.03±0.09	0.83 (1450)	3.36	(2)	(1b)	(1b)	(1b)
1137+6604[1]	1.00	1.05	0.24±0.04	1.04±0.09	1.17 (1450)	2.98	(2)	(1c)	(1c)	(1c)
1138+0204[1]	2.37		0.97±0.09	0.22±0.03	0.35 (1450)	0.00		(1b)	(1b)	(1b)
1148+5454	1.19	0.97	0.56±0.17	1.04±0.11	1.35 (1450)	-0.13	(2)	(1c)	(1c)	(1c)
1150+4947	2.01		0.66±0.05	0.19±0.03	0.26 (1450)	3.44		(1b)	(1b)	(1b)
1156+2123	2.56		0.95±0.10	0.31±0.04	0.49 (1450)	2.23		(1b)	(1b)	(1b)
1156+2931	1.58	0.57	1.27±0.08	0.73±0.06	1.33 (1450)	3.04	(2)	(1c)	(1c)	(1c)
1206+4557	1.27	0.45	-0.32±0.49	1.96±0.23	1.69 (1450)	0.00	(2)	(1c)	(1c)	(1c)
1211+1419	2.70		1.27±0.34	1.31±0.37	2.37 (1450)	-0.37		(1a)	(1a)	(1a)
1214+1804[1]	2.74		1.55±0.17	0.25±0.05	0.52 (1450)	0.00		(1b)	(1b)	(1b)

Table 3—Continued

QSO	N_{HI}	$f_{\nu_0}^{obs}$	α	f_{ν_0}	f_{ν}^{obs}	RL	References				
	(a)	(b)	(c)	(d)	(e)	(f)	(b)	(c)	(d)	(e)
1215+6423[1]	2.10		-0.14±2.50	0.19±0.06	0.18 (1340)	3.18		(1c)	(1c)	(1c)
1216+0655	1.57		0.84±0.06	0.97±0.06	1.44 (1450)	0.44		(1b)	(1b)	(1b)
1216+503a[7]	1.87		···	0.35	0.58 (1326)	0.00		(4)	(1c)	(1c)
1219+0447[1]	1.68		0.83±0.05	0.06±0.006	0.15 (2457)	0.00		(1c)	(1c)	(1c)
1219+7535[2]	3.13		0.00±0.36	2.21±0.34	2.21 (1450)	0.45		(1a)	(1a)	(1a)
1226+0219[3]	1.81	7.40	-1.51±2.68	47.6±1.94	26.9 (1330)	4.26	(7)	(1a)	(1a)	(1a)
1229-0207[5]	2.34	0.23	1.23±0.78	0.32±0.20	0.57 (1450)	3.25		(1c)	(1c)	(1c)
1230+0947[2]	1.81		1.33±0.36	0.51±0.16	0.96 (1450)	0.00		(1b)	(1b)	(1b)
1241+1737	1.81	0.25	···	···	···	2.16	(2)			
1247+2647[5]	1.03	0.76	···	···	···	-0.07	(2)			
1248+3032	1.23		0.19±0.28	0.08±0.01	0.09 (1450)	3.19		(1c)	(1c)	(1c)
1248+3142[8]	1.27		···	0.26	···	0.00		(4)		(8)
1248+4007	1.44	0.57	0.67±0.76	0.48±0.16	0.65 (1450)	0.00	(2)	(1c)	(1c)	(1c)
1249+2929[8]	1.14		···	0.22	···	0.00		(4)		(8)
1250+3122	1.24		···	0.33	0.54 (1279)	0.00		(4)	(1b)	(1b)
1252+1157	2.34		0.80±0.38	0.37±0.07	0.54 (1450)	3.12		(1c)	(1c)	(1c)
1253-0531[2]	2.12	1.43	1.58±0.02	0.14±0.01	0.30 (1450)	4.47	(2)	(1c)	(1c)	(1c)
1257+3439[1]	1.13		···	0.51	0.94 (1450)	1.14		(4)		(9)
1258+2835[1]	0.93		0.21±0.81	0.32±0.04	0.34 (1331)	0.00		(1c)	(1c)	(1c)
1259+5918	1.37	1.02	1.14±0.45	0.96±0.32	1.63 (1450)	0.00	(2)	(1b)	(1b)	(1b)
1302-1017	3.37	0.99	1.17±0.06	2.00±0.14	3.47 (1450)	2.34	(2)	(1b)	(1b)	(1b)
1305+0658	2.16		-0.07±0.04	0.24±0.03	0.23 (1450)	3.13		(1c)	(1c)	(1c)
1309+3531[1]	2.55		1.08±0.16	0.68±0.11	1.12 (1450)	1.58		(1b)	(1b)	(1b)
1317+2743	1.18	0.73	0.64±0.19	1.04±0.10	1.40 (1450)	0.00	(2)	(1c)	(1c)	(1c)
1317+5203[1,2]	1.90		0.54±0.82	0.51±0.15	0.66 (1450)	2.70		(1c)	(1c)	(1c)
1318+2903	1.14	0.26	-0.06±10.0	0.58±0.25	0.56 (1450)	0.00	(2)	(1b)	(1b)	(1b)
1320+2925	1.17		1.37±1.63	0.19±0.26	0.36 (1450)	0.00		(1c)	(1c)	(1c)
1322+6557	1.92		0.91±0.16	0.66±0.07	1.01 (1450)	0.00		(1b)	(1b)	(1b)
1323+6530[1,4,5]	1.99		···	0.11	···	3.02		(4)		
1327-2040[1]	7.53	0.19	0.83±0.41	0.55±0.12	0.82 (1450)	2.62	(2)	(1c)	(1c)	(1c)

Table 3—Continued

QSO	N_{HI}	$f^{obs}_{\nu_0}$	α	f_{ν_0}	f^{obs}_{ν}	RL	References			
	(a)	(b)	(c)	(d)	(e)	(f)	(b)	(c)	(d)	(e)
1328+3045[5]	1.16		0.39±0.13	0.20±0.01	0.24 (1450)	4.49		(1c)	(1c)	(1c)
1329+4117[5]	0.97	0.95	···	···	···	0.00	(2)			
1333+1740	1.75	0.51	0.92±4.71	0.65±1.81	1.01 (1450)	1.39	(2)	(1b)	(1b)	(1b)
1351+3153[1,5]	1.29		-0.91±2.78	0.16±0.28	0.11 (1319)	2.88		(1c)	(1c)	(1c)
1351+6400[1]	2.10		0.97±0.06	1.62±0.07	4.36 (2531)	1.10		(1c)	(1c)	(1c)
1352+0106	2.25	0.07	0.50±1.23	0.83±0.33	1.05 (1450)	0.00	(2)	(1c)	(1c)	(1c)
1352+1819	2.03		0.38±0.13	0.59±0.11	0.71 (1450)	0.00		(1b)	(1b)	(1b)
1354+1933	2.21	0.40	0.68±0.11	0.56±0.05	0.77 (1450)	3.53	(2)	(1c)	(1c)	(1c)
1356+5806[2]	1.40		0.09±6.29	0.56±0.04	0.59 (1344)	2.34		(1c)	(1c)	(1c)
1401+0952[2]	1.96		2.03±0.29	0.12±0.05	0.31 (1450)	0.72		(1b)	(1b)	(1b)
1404+2238[1]	1.99		1.03±0.04	0.31±0.04	0.86 (2413)	0.29		(1c)	(1c)	(1c)
1407+2632	1.47	0.83	0.28±0.05	1.20±0.07	1.38 (1450)	0.00	(2)	(1c)	(1c)	(1c)
1415+4509	1.13		0.65±0.08	0.85±0.05	1.32 (1790)	0.00		(1b)	(1b)	(1b)
1416+0642[1]	6.24		1.20±15.9	0.25±3.47	0.40 (1308)	3.67		(1c)	(1c)	(1c)
1424-1150	7.54		-0.04±0.18	0.85±0.07	0.83 (1450)	2.59		(1c)	(1c)	(1c)
1425+2645[1]	2.55	0.15	1.67±0.10	0.22±0.03	0.48 (1450)	2.43	(2)	(1b)	(1b)	(1b)
1427+4800	1.88		0.47±0.24	0.69±0.07	0.86 (1450)	0.00		(1b)	(1b)	(1b)
1435-0134	3.66	0.82	···	···	···	0.00	(5)			
1440+3539[1]	1.00		0.44±0.09	3.61±0.15	4.96 (1857)	-0.58		(1b)	(1b)	(1b)
1444+4047	1.27	0.89	0.86±0.04	1.06±0.06	1.59 (1450)	0.00	(2)	(1b)	(1b)	(1b)
1512+3701	1.39	0.57	0.94±0.12	0.61±0.06	0.95 (1450)	2.75	(2)	(1b)	(1b)	(1b)
1517+2356[4]	3.91		···	0.51	···	0.00		(4)		
1517+2357[4]	3.91		···	0.08	···	0.00		(4)		
1521+1009	2.88	1.65	···	···	···	0.00	(2)			
1538+4745[1]	1.64	0.34	0.57±0.06	1.03±0.05	1.34 (1450)	1.28	(2)	(1c)	(1c)	(1c)
1544+4855	1.60	0.10	2.04±1.72	0.36±0.81	0.95 (1450)	0.00	(2)	(1b)	(1b)	(1b)
1555+3313[2]	2.35		1.79±0.08	0.03±0.005	0.07 (1450)	3.03		(1c)	(1c)	(1c)
1611+3420[2]	1.65		···	0.18	0.30 (1322)	4.88		(4)	(1c)	(1c)
1618+1743	4.14		-0.30±0.05	1.30±0.06	1.13 (1450)	2.70		(1b)	(1b)	(1b)
1622+2352	4.46		1.75±0.16	0.09±0.01	0.21 (1450)	3.54		(1c)	(1c)	(1c)

Table 3—Continued

QSO	N_{HI} (a)	$f_{\nu_0}^{obs}$ (b)	α (c)	f_{ν_0} (d)	f_{ν}^{obs} (e)	RL (f)	References (b)	(c)	(d)	(e)
1626+5529[1]	1.83		0.29±0.16	1.13±0.22	1.30 (1450)	0.00		(1b)	(1b)	(1b)
1630+3744	1.07	0.84	···	···	···	0.00	(2)			
1634+7037	4.55	1.96	···	···	···	0.00	(2)			
1637+5726[2]	1.90		0.17±0.02	0.64±0.05	0.70 (1450)	3.98		(1c)	(1c)	(1c)
1641+3954[3]	1.02	0.61	1.04±0.08	0.41±0.06	0.67 (1450)	3.92	(2)	(1c)	(1c)	(1c)
1704+6048[1]	2.32	0.90	1.25±0.16	0.94±0.14	1.68 (1450)	2.86	(2)	(1b)	(1b)	(1b)
1715+5331	2.71		0.43	0.58	0.29 (1450)	0.53		(10)		(2)
1718+4807[1]	2.27		-0.43±0.84	5.01±1.16	4.09 (1450)	1.52		(1c)	(1c)	(1c)
1803+7827[3]	3.92		1.69±0.02	0.53±0.05	1.16 (1450)	3.35		(1c)	(1c)	(1c)
1821+6419[1]	3.98	1.86	0.86±0.07	3.90±0.13	8.37 (2204)	1.10	(2)	(1c)	(1c)	(1c)
1845+7943[1]	4.17		0.66±0.27	0.42±0.08	0.58 (1450)	3.88		(1a)	(1a)	(1a)
2112+0556	6.48	0.29	0.48±0.93	0.54±0.16	0.67 (1450)	0.00	(2)	(1b)	(1b)	(1b)
2128-1220	4.75	0.35	0.27±1.63	1.77±0.51	2.02 (1450)	2.99	(11)	(1b)	(1b)	(1b)
2135-1446[1]	4.71		0.94±0.42	0.57±0.15	0.88 (1450)	3.17		(1b)	(1b)	(1b)
2141+1730[1]	8.20		1.22±0.05	0.81±0.14	1.43 (1450)	2.84		(1b)	(1b)	(1b)
2145+0643	4.90		0.99±0.68	0.72±0.31	1.14 (1450)	3.58		(1c)	(1c)	(1c)
2201+3131[2]	9.02	0.60	0.96±0.08	3.15±0.33	4.93 (1450)	3.64	(2)	(1b)	(1b)	(1b)
2216-0350[2]	5.66	0.18	1.21±0.09	0.40±0.05	0.71 (1450)	3.43	(2)	(1c)	(1c)	(1c)
2223-0512[2]	5.47	0.16	···	···	···	4.35	(2)			
2230+1128[2]	5.42		0.76±0.96	0.45±0.21	0.64 (1450)	4.39		(1c)	(1c)	(1c)
2243-1222	4.94		-0.38±0.06	1.50±0.10	1.25 (1450)	3.32		(1c)	(1c)	(1c)
2251+1120[1]	5.08		1.2	1.46	0.49 (1450)	3.06		(12)		(2)
2251+1552	6.38	0.09	1.04±0.05	0.71±0.07	1.15 (1450)	3.94	(2)	(1c)	(1c)	(1c)
2251-1750[1]	2.77		1.06±0.08	1.47±0.09	4.32 (2507)	0.07		(1c)	(1c)	(1c)
2300-6823	3.69		-0.34±0.75	0.26±0.04	0.22 (1450)	3.18		(1b)	(1b)	(1b)
2340-0339	3.61		0.68±0.05	0.99±0.06	1.36 (1450)	2.24		(1c)	(1c)	(1c)
2344+0914	5.76	0.34	···	0.22	0.41 (1450)	3.52	(2)	(4)	(9)	(9)
2352-3414	1.08		0.07±0.03	0.74±0.05	0.77 (1450)	2.70		(1c)	(1c)	(1c)

Note. — Columns (a) 10^{20} cm^{-2} from Stark et al. 1992; Burstein & Heiles 1982; Lockman & Dickey 1995; (b) Direct measurement of flux at Lyman Limit in μJy; (c) Measured spectral index; (d) Extrapolated flux at Lyman Limit in μJy; (e) Measured flux at the rest wavelength listed in Å; (f) Radio Loudness, RL = log[S(5 GHz)]/log[S(1450 $\AA$)]

References. — (1) this paper, FOS data [a] H130, [b] H190, [c] H270; (2)Lanzetta et al. 1993; (3)Zheng et al. 1995; (4)Zheng et al. 1997; (5)Hamann et al. 1995; (6) Tytler & Fan 1992; (7)Appenzeller et al. 1998; (8)Sanduleak & Pesch 1984; (9)Osmer et al. 1994; (10) Zheng & Malkan 1993; (11)Kinney et al. 1991; (12) Green 1996

[1]Object spectrum shows associated absorption

[2]Observed only with pre-COSTAR FOS and A-1 aperture, not used for proximity effect

[3]Object is classified as a blazar or BL Lac

[4]Flux estimated from scaling composite QSO spectrum to match V

[5]Object spectrum shows damped Ly-α absorption

[6]No Ly-α forest observed, not used for proximity effect

[7]Binary quasar, not used for proximity effect

[8]Flux estimated from scaling composite QSO spectrum to match B

Table 4. Measurements of $J(\nu_0)$

Sample (a)	$\mathcal{N}_{lines}$ (b)	γ,norm. (c)	β	b (d)	method (e)	log[$J(\nu_0)$] (f)	χ^2 (g)	Q_{χ^2} (h)	Q_{KS} (i)
1	259	0.82, 13.6	1.46	···	BDO	$-22.04^{+0.43}_{-1.11}$	2.13	0.95	0.80
1	259	0.82, 6.73	1.46	35	ML	$-22.11^{+0.51}_{-0.40}$	1.21	0.29	0.80
1	259	0.82, 9.61	1.46	25	ML	$-22.12^{+0.52}_{-0.39}$	1.01	0.41	0.80
1	259	0.82, 9.31	1.45	25	ML	$-22.13^{+0.51}_{-0.41}$	0.78	0.58	0.80
1	259	0.82, 11.8	1.70	30	ML	$-21.74^{+0.45}_{-0.36}$	1.34	0.23	0.80
1	259	0.82, 38.0	2.04	25	ML	$-21.47^{+0.43}_{-0.32}$	1.10	0.35	0.80
2	289	0.15, 31.3	1.46	···	BDO	$-22.06^{+0.05}_{-0.62}$	2.62	0.91	0.30
2	289	0.15, 12.0	1.46	35	ML	$-22.03^{+0.44}_{-0.37}$	1.32	0.24	0.30
2	289	0.15, 13.9	1.46	25	ML	$-22.04^{+0.45}_{-0.36}$	1.34	0.23	0.30
2	289	0.15, 13.6	1.45	25	ML	$-22.06^{+0.45}_{-0.37}$	1.48	0.18	0.30
2	289	0.15, 17.6	1.70	30	ML	$-21.69^{+0.40}_{-0.32}$	1.47	0.18	0.30
2	289	0.15, 31.1	2.04	25	ML	$-21.42^{+0.37}_{-0.28}$	0.88	0.50	0.30
1a	162	1.50, 10.1	1.46	···	BDO	$-22.87^{+1.19}_{-0.82}$	1.51	0.98	0.64
1a	162	1.50, 4.92	1.46	35	ML	$-22.18^{+0.90}_{-0.61}$	0.17	0.98	0.64
1a	162	1.50, 3.67	1.46	35	ML	$-21.72^{+1.52}_{-0.74}$ [1]	1.02	0.40	0.62
1a	162	1.50, 3.71	1.46	35	ML	$-21.88^{+1.54}_{-0.73}$ [2]	0.98	0.43	0.62
1b	97	-0.87, 53.0	1.46	···	BDO	$-22.02^{+0.005}_{-1.33}$	2.44	0.87	0.98
1b	97	-0.87, 26.1	1.46	35	ML	$-21.98^{+0.76}_{-0.54}$	2.25	0.03	0.98
1b	97	-0.87, 21.5	1.46	35	ML	$-21.76^{+0.92}_{-0.58}$ [1]	1.31	0.24	0.95
1b	97	-0.87, 21.5	1.46	35	ML	$-21.95^{+0.93}_{-0.57}$ [2]	1.27	0.26	0.95
3	214	0.28, 9.97	1.46	35	ML	$-21.57^{+0.80}_{-0.52}$	0.47	0.82	0.70
4	208	1.04, 5.76	1.46	35	ML	$-22.15^{+0.66}_{-0.46}$	1.47	0.19	0.65
5	373	0.60, 7.93	1.46	35	ML	$-21.74^{+0.55}_{-0.39}$	0.97	0.44	0.96
6	301	0.89, 6.57	1.46	35	ML	$-22.17^{+0.44}_{-0.37}$	0.98	0.43	0.97
7	415	0.67, 7.72	1.46	35	ML	$-21.82^{+0.46}_{-0.37}$	0.93	0.46	0.98
7a	213	0.79, 7.28	1.46	35	ML	$-22.22^{+0.74}_{-0.51}$	0.29	0.94	0.64
7b	202	0.72, 7.29	1.46	35	ML	$-21.60^{+0.70}_{-0.47}$	1.15	0.33	0.98
8	422	0.69, 7.64	1.46	35	ML	$-21.85^{+0.46}_{-0.36}$	0.82	0.55	0.97
8a	220	0.84, 7.10	1.46	35	ML	$-22.23^{+0.73}_{-0.49}$	0.46	0.83	0.56
8b	202	0.72, 7.29	1.46	35	ML	$-21.60^{+0.70}_{-0.47}$	1.15	0.33	0.98

Table 4—Continued

Sample (a)	$\mathcal{N}_{lines}$ (b)	γ,norm. (c)	β	b (d)	method (e)	$\log[J(\nu_0)]$ (f)	χ^2 (g)	Q_{χ^2} (h)	Q_{KS} (i)
9	906	0.61, 9.26	1.46	35	ML	$-21.21^{+0.49}_{-0.32}$	0.55	0.76	0.91
9a	474	0.63, 9.23	1.46	35	ML	$-21.79^{+0.53}_{-0.40}$	0.76	0.59	0.87
9b	432	1.05, 6.40	1.46	35	ML	$-20.82^{+\infty}_{-0.51}$	0.33	0.91	0.71

Note. —
(a) Sample number- (1) all lines with $W > 0.32$ Å, (1a) $z < 1$, (1b) $z > 1$; (2) all lines with $W > 0.24$ Å, (2a) $z < 1$, (2b) $z > 1$; (3) RL > 1.0; (4) RL < 1.0; (5) sample (1) including associated absorbers; (6) sample (1) including damped Ly-α absorbers; (7) sample (1) including both associated absorbers and damped Ly-α absorbers; (7a) $z < 1$, (7b) $z > 1$; (8) sample (1) including associated absorbers, damped Ly-α absorbers, and blazars; (8a) $z < 1$, (8b) $z > 1$; (9) sample (8), all lines above variable threshold, (9a) $z < 1$, (9b) $z > 1$
(b) Number of Ly-α forest lines in sample
(c) Normalization, definition depends on method listed in (e), see §6, Equ. 9 and Equ. 10
(d) Doppler parameter in km s^{-1}
(e) BDO- Bajtlik, Duncan, & Ostriker (1988), ML- maximum likelihood, see Kulkarni & Fall (1993)
(f) Best fit value of $\log[J(\nu_0)]$ in units of ergs s^{-1} cm^{-2} Hz^{-1} sr^{-1}
(g) χ^2 of data versus the ionization model used
(h) χ^2 probability for the ionization model used
(i) K-S probability

[1]no dz removed for metal lines

[2]no dz removed for metal lines, $(\Omega_M, \Omega_\Lambda) = (0.3, 0.7)$

Table 5. Simulation Results

Input $\log[J(\nu_0)]$ (a)	z (b)	W_{thr} (c)	γ,A (d)	Recovered $\log[J(\nu_0)]$ (e)	χ^2 (f)
-23.0	all	0.32	1.41,7.81	$-22.74^{+0.15}_{-0.13}$	5.13
-23.0	all	variable	1.15,8.94	$-22.47^{+0.13}_{-0.12}$	5.73
-22.0	all	0.32	1.17,8.27	$-21.32^{+0.41}_{-0.29}$	13.6
-22.0	$z < 1$	0.32	0.95,8.74	$-20.81^{+1.91}_{-0.62}$	9.53
-22.0	$z > 1$	0.32	1.79,5.21	$-21.64^{+0.39}_{-0.28}$	6.70
-22.0	all	variable	1.48,6.71	$-21.63^{+0.20}_{-0.19}$	3.21
-22.0	$z < 1$	variable	0.75,10.0	$-21.34^{+0.60}_{-0.36}$	11.3
-22.0	$z > 1$	variable	1.52,6.09	$-21.63^{+0.25}_{-0.22}$	1.30
-21.0	all	0.32	1.44,7.25	$-20.81^{+0.65}_{-0.41}$	1.56
-21.0	all	variable	1.13,8.72	$-20.81^{+0.53}_{-0.38}$	0.73
$(0.017)\log(1+z) - 21.87$	all	0.32	0.99,9.46	$-21.54^{+0.38}_{-0.25}$	3.35
$(0.017)\log(1+z) - 21.87$	$z < 1$	0.32	0.51,11.1	$-21.80^{+0.80}_{-0.45}$	4.63
$(0.017)\log(1+z) - 21.87$	$z > 1$	0.32	1.90,4.74	$-21.54^{+0.40}_{-0.29}$	1.55
$(0.017)\log(1+z) - 21.87$	all	variable	1.38,7.32	$-21.56^{+0.22}_{-0.21}$	0.57
$(0.017)\log(1+z) - 21.87$	$z < 1$	variable	0.84,10.1	$-21.83^{+0.45}_{-0.34}$	3.28
$(0.017)\log(1+z) - 21.87$	$z > 1$	variable	2.48,2.67	$-21.37^{+0.31}_{-0.23}$	0.82

Note. — (a) Value of $\log[J(\nu_0)]$ used for modifying absorber column densities according to Equ. 4 and Equ. 5 ; (b) Redshift range of solution; (c) Equivalent width threshold in Å for line sample used in solution; (d) Maximum likelihood γ for line sample used, maximum likelihood method normalization, see §6, Equ. 10; (e) Value of $\log[J(\nu_0)]$ from simulated spectra using the ML technique; (f) χ^2 of data versus the BDO ionization model

Table 6. HI Ionization Rates

Sample (a)	γ,A (b)	β	b	log[$\Gamma_{\rm HI}$]	χ^2_ν (c)	$Q_{\chi^2_\nu}$ (d)	log[$J(\nu_0)$] (e)
1	0.69,7.65	1.46	35	$-12.17^{+0.50}_{-0.40}$	0.49	0.81	-21.56
1a	0.85,7.11	1.46	35	$-12.70^{+0.74}_{-0.51}$	0.38	0.88	-22.09
1b	0.72,7.29	1.46	35	$-11.88^{+0.74}_{-0.50}$	0.48	0.81	-21.28
2	0.61,9.27	1.46	35	$-11.27^{+0.74}_{-0.45}$	0.78	0.58	-20.67
2a	0.63,9.24	1.46	35	$-12.23^{+0.55}_{-0.42}$	1.17	0.31	-21.62
2b	1.05,6.40	1.46	35	$-9.089^{+\infty}_{-2.22}$	1.17	0.31	-18.48
1	0.69, 7.21[1]	1.46	35	-12.67,1.73[1]	1.01	0.40	...
2	0.61, 9.04[1]	1.46	35	-10.86,3.04[1]	0.47	0.82	...

Note. — (a) (1) all lines with $W > 0.32$ Å, (1a) $z < 1$, (1b) $z > 1$, (2)all lines above variable threshold, (2a) $z < 1$, (2b) $z > 1$; (b) Maximum likelihood method normalization (see §6, Equ. 10); (c) χ^2 of data versus the ionization model used; (d) χ^2 probability for the ionization model used; (e) $J(\nu_0)$ implied by Γ listed and $\alpha_s = 1.8$ (see §6.2, Equ. 12)

[1]maximum likelihood solution for log($A_{\rm pl}$),$B_{\rm pl}$ and normalization (see §6.2, Equ. 13)